Hull-Propeller Interaction and Its Effect on Propeller Cavitation

Regener, Pelle Bo; Andersen, Poul

Publication date:
2016

Document Version
Publisher's PDF, also known as Version of record

Hull-Propeller Interaction and Its Effect on Propeller Cavitation

PhD Thesis

$$(EIv'')'' = q - \rho A \ddot{v}$$

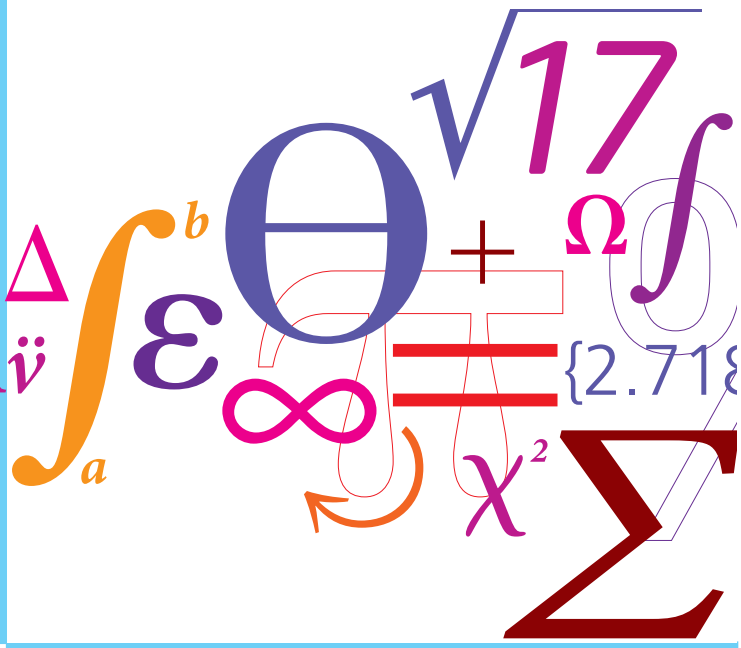

Pelle Bo Regener
DCAMM Special Report No. S223
November 2016

DTU Mechanical Engineering
Department of Mechanical Engineering

Hull-Propeller Interaction and Its Effect on Propeller Cavitation

Pelle Bo Regener

Technical University of Denmark
Department of Mechanical Engineering
Section for Fluid Mechanics, Coastal and Maritime Engineering

November 2016

Abstract

In order to predict the required propulsion power for a ship reliably and accurately, it is not sufficient to only evaluate the resistance of the hull and the propeller performance in open water alone. Interaction effects between hull and propeller can even be a decisive factor in ship powering prediction and design optimization. The hull-propeller interaction coefficients of effective wake fraction, thrust deduction factor, and relative rotative efficiency are traditionally determined by model tests.

Self-propulsion model tests consistently show an increase in effective wake fractions when using a Kappel propeller (propellers with a tip smoothly curved towards the suction side of the blade) instead of a propeller with conventional geometry. The effective wake field, i.e. the propeller inflow when it is running behind the ship, but excluding the propeller-induced velocities, can not be measured directly and only its mean value can be determined experimentally from self-propulsion tests.

In the present work the effective wake field is computed using a hybrid simulation method, known as RANS-BEM coupling, where the flow around the ship is computed by numerically solving the Reynolds-averaged Navier–Stokes equations, while the flow around the propeller is computed by a Boundary Element Method. The velocities induced by the propeller working behind the ship are known explicitly in such method, which allows to directly compute the complete effective flow field by subtracting the induced velocities from the total velocities. This offers an opportunity for additional insight into hull-propeller interaction and the propeller's actual operating condition behind the ship, as the actual (effective) inflow is computed.

Self-propulsion simulations at model and full scale were carried out for a bulk carrier, once with a conventional propeller, and once with a Kappel propeller. However, in contrast to the experimental results, neither a significant difference in effective wake fraction nor other notable differences in effective flow were observed in the simulations. It is therefore concluded that the differences observed in model tests are not due to the different radial load distributions of the two propellers. One hypothesis is that the differences are a consequence of the geometry of the vortices shed from the propeller blades. The shape and alignment of these trailing vortices were modeled in a relatively

simple way, which presumably does not reflect the differences between the propellers sufficiently.

Obtaining effective wake fields using the hybrid RANS-BEM approach at model and full scale also provides the opportunity to investigate the behind-ship cavitation performance of propellers with comparably low computational effort. The boundary element method for propeller analysis includes a partially nonlinear cavitation model, which is able to predict partial sheet cavitation and supercavitation. The cavitation behaviour of the conventional propeller and the Kappel propeller from the earlier simulations was investigated in the behind-ship condition using this model, focusing on the influence of the velocity distribution of the inflow field. Generally, the results agree well with experiments and the calculations are able to reproduce the differences between conventional and Kappel propellers seen in previous experiments. Nominal and effective wake fields at model and full scale were uniformly scaled to reach the same axial wake fraction, so that the only difference lies in the distribution of axial of velocities and in-plane velocity components. Calculations show that details of the velocity distribution have a major effect on propeller cavitation, signifying the importance of using the correct inflow, i.e. the effective wake field when evaluating propeller cavitation performance.

Resumé

For at kunne bestemme den nødvendige effekt til fremdrivning af et skib tilstrækkelig nøjagtigt er det ikke nok kun at betragte modstanden af skroget og kræfterne på propelleren i åbent vand. Vekselvirkningen mellem skroget og propelleren er af afgørende betydning for nøjagtigheden af bestemmelsen, og dermed er det også nødvendigt at tage hensyn til dette ved optimering af propelleren. Vekselvirkningen mellem skrog og propeller beskrives ved hjælp af medstrøms- og sugningskoefficienterne samt den relative rotative virkningsgrad. Disse bestemmes traditionelt ved modelforsøg.

Selvfremdrivningsforsøg med propellere af Kappel-typen (med bladtippen vendt mod sugesiden) har vist en forøgelse af den effektive medstrøm i forhold til forsøg med en konventionel propeller. Det effektive medstrømsfelt, dvs. tilstrømningen til propelleren, når den arbejder bag skibet, men uden de propellerinducerede hastigheder, kan ikke måles direkte, men kun bestemmes eksperimentelt som en middelværdi i forbindelse med selvfremdrivningsforsøget. I det foreliggende arbejde er det effektive medstrømsfelt beregnet ved en metode, RANS-BEM-kobling, hvor strømningen over skibet er beregnet ved numerisk løsning af Navier-Stokes ligningerne, mens strømningen over propelleren er beregnet med en randelementmetode. Herved kan de propellerinducerede hastigheder findes direkte, når propelleren arbejder bag skibet, og ved at subtrahere disse hastigheder fra de totale hastigheder kan den effektive medstrøm i form af et hastighedsfelt bestemmes. Herved opnår man forøget viden om, hvorledes propelleren arbejder bag skibet, idet man beregner den faktiske (effektive) tilstrømning til propelleren.

Selvfremdrivningsberegninger er blevet udført i både model- og fuldskala for et massegodsskib. Beregningerne er udført for skibet med en konventionel propeller og en Kappel propeller. I modsætning til forsøgsresultaterne viser beregningerne ingen større forskelle i den effektive tilstrømning til propellerne for henholdsvis den konventionelle og Kappel-propelleren. Det må derfor konkluderes, at de forskelle, der er observeret ved modelforsøgene, ikke skyldes de forskellige belastningsfordelinger for de to propellere. En hypotese er, at forskellene er en konsekvens af geometrien af hvirvlerne, som er afløst fra propellerbladene. Disse er modelleret på en relativt simpel måde, der formodentlig ikke afspejler forskellene mellem de to propellere i tilstrækkelig grad.

Med beregning af effektive medstrømsfelter ved hjælp af ovenstående RANS-BEM-kobling er det muligt at undersøge kavitationsforholdene for propelleren bag skib med relativt begrænset beregningsindsats. I randelementmetoden er der implementeret en delvis ikke-lineær kavitationsmodel, som kan beskrive såvel delvis som fuld (super) lagkavitation. Med denne model er kavitationsdannelsen for de angivne propellere bag skib undersøgt, dvs. indflydelsen af den effektive medstrømsfordeling. Der er generelt god overensstemmelse mellem resultater fra modelforsøg og fra beregninger, og beregningerne er i stand til at vise forskellene mellem Kappel- og den konventionelle propeller. For at undersøge indflydelsen af hastighedsfordelingen i tilstrømningen til propelleren blev der udført en serie beregninger, hvor hastighedsfeltet blev skaleret til den samme medstrømskoefficient. Denne svarer til den effektive medstrømskoefficient i fuldskala; men beregningerne blev udført for hastighedsfordelinger svarende til både model- og fuldskala. Beregningerne viser, at denne fordeling har stor indflydelse på kavitationsdannelsen, således at det er vigtigt at bruge den rigtige tilstrømning, dvs. det effektive medstrømsfelt, når man skal vurdere propellerens kavitationsforhold.

Acknowledgments

While this thesis concludes three years of work on ship propulsion and propeller hydrodynamics, it does not appear that this is the end of my work in this exciting and challenging field. Still, as this thesis marks the end of a both fun and intense phase of my career, I would like to take the opportunity to thank everyone who helped, guided, and supported me on my way so far. In this context, some persons certainly deserve individual acknowledgment.

First of all, I want to express my sincere and extraordinary gratitude to my supervisor, Poul Andersen. Not only for his constant support over the past three years, his always valuable advice, sharing his deep understanding and passion for propellers and ship hydrodynamics, but also for always doing so in an encouraging, positive, and lighthearted way. Maintaining this positive attitude even in difficult moments makes an enormous difference and it is difficult to express how much I appreciate that.

Also, thank you to all current and former colleagues in the Maritime Group at DTU Mekanik. Work is a lot more fun in such environment, being surrounded by smart and kind people. Out of many great colleagues, Yasaman Mirsadraee deserves special thanks and mention. Not only for being a terrific colleague, but also for her invaluable help over the last one and a half years. For her persistence when deriving all details of the cavitation model for the fifth time, trying to explore more possibilities and tracking down the last mistakes. Furthermore, her help in designing the propellers used for the demonstration cases in this thesis is also gratefully acknowledged.

Thanks are due to everyone at Flowtech for their great cooperation and collaboration and advances made on the SHIPFLOW code over the last years. At Flowtech, Björn Regnström was a great help (even when *my* bugs were causing the mess!) and always very responsive to our ideas on propeller modeling.

I also appreciated the cooperation within the MRT project (and, obviously, the funding!), with the external project partners MAN Diesel & Turbo and Mærsk Maritime Technology. Sharing hull and propeller geometries, model test results, and experience as openly as they did was a great help.

Thank you to all friends, fellow students, mentors, and colleagues – also from my years in Bremen and Hamburg!

Not only during the past three years, the support from my family has been extraordinary and reaching this point would have been impossible without them. I could not be happier to have you in my life!

Preface

This thesis is submitted in partial fulfillment of the requirements for the PhD degree. The studies have taken place at the Technical University of Denmark, Department of Mechanical Engineering, Section for Fluid Mechanics, Coastal, and Maritime Engineering, where the student was employed during the entire duration of the studies (October 2013 – November 2016). The project was supervised by Associate Professor Poul Andersen.

Funding was provided by Innovation Fund Denmark through the project titled "Major Retrofitting Technologies for Containerships" and the Department of Mechanical Engineering at the Technical University of Denmark.

All calculations were carried out on DTU's central high-performance cluster, using SHIPFLOW version 6.2.01 (released in September 2016) and programs developed and implemented as part of the present work.

Contents

1 Introduction

1.1 Background and Motivation

To overcome the resistance force a ship experiences when moving through water, a force in opposite direction is required. Historically, sails were the sole method to provide that thrust until the advent of the steam engine called for some kind of mechanical propulsion device around 1800. Around that time, the first forms of the modern screw propeller emerged to quickly become the dominant type of propulsor for seagoing ships (Kerwin and Hadler 2010). From the mid-nineteenth century to the present day, screw propellers have been and remain the by far most common type of propulsor. Except for some waterjet-driven high speed vessels, or very specialized ships like tugs, the screw propeller today powers nearly all commercial ships, further exceptions and radically different concepts being very rare.

Even though screw propellers have existed for more than two centuries, there is no easy or even general solution to the complete design problem, and improving the efficiency of marine propellers is still subject to continuous research and development, with proposed modifications small and large.

Today, ships account for carrying around 90% of the world trade* and about 3% of worldwide CO_2 emissions†. On cargo ships, most of the total engine power is required for propulsion. At this scale, even small increases in energy efficiency can have a substantial global impact, emphasizing the importance of further efforts to optimize the concept and application of the screw propeller.

Propulsive Efficiency

At the end of the day, it is in the interest of society to move a ship – and the goods it transports – along its trade route at a required speed using as little energy as possible.

Obviously, it is vital to any optimization problem and technique to have a precisely specified objective. As a number of different "efficiencies" are commonly used in the field of naval architecture, this section intends to give a

* United Nations Conference on Trade and Development (2016)
† International Maritime Organization (2015)

very brief description of the most important terms and point out their relevancy for this thesis.

Usually, efficiency is defined as the ratio of *useful* work or power to the *expended* work or power and denoted η. Both is true for most definitions of "efficiencies" in our context. The most useful conceivable power used on a ship is the power used to overcome the resistance it experiences when moving through calm water. This value is called *effective power*, P_E in short, and is easily found from the product of the total resistance force R_T and the ship velocity v_S.

$$P_E = R_T \cdot v_S \tag{1.1}$$

The *total expended* work or power is not as easy to define, as it strongly depends on the working principle of the main engine. As this is clearly outside of the scope (and quite possibly also the interest) of any ship hydrodynamicist, we limit ourselves to considering the *propulsive efficiency*, treating the main engine output power as the reference value. This is commonly referred to as the brake power P_B and measured at the crankshaft or the output shaft on a test bed. However, there will be further energy losses in between the main engine and the propeller. These losses are expressed as a *shafting efficiency* η_S, which is usually around 99%, but not of major interest to the hydrodynamicist or propeller designer, either.

Having now reached the propeller shaft, we also reached the scope of interest for our purpose. Using the power that is actually delivered and available to the propeller, $P_D = P_B \eta_S$, we find the *quasipropulsive efficiency* from

$$\eta_D = \frac{P_E}{P_D} \tag{1.2}$$

Given that usually the shafting losses are of lesser concern to the naval architect than the design and arrangement of the propeller, the *quasipropulsive efficiency* is often just referred to as the *propulsive efficiency*. This thesis will also use this somewhat inaccurate but common designation.

At this point it is important to stress that while η_D is indeed the typical optimization objective, it still needs to be broken down to several components to understand its value and to represent the different physical effects involved.

Firstly, the propeller's efficiency is assessed under ideal conditions. Measuring thrust and torque in uniform inflow and at a constant advance velocity and constant shaft speed is sufficient to compute the *open-water efficiency*. The ratio of advance velocity and rate of revolutions of the propeller shaft are expressed in the nondimensional advance ratio, defined as

$$J = \frac{v}{nD} \tag{1.3}$$

where v is the advance velocity, n is the shaft speed and D is the propeller diameter. Also writing thrust T and torque Q as nondimensional coefficients K_T and K_Q,

$$K_T = \frac{T}{\rho n^2 D^4} \quad \text{and} \quad K_Q = \frac{Q}{\rho n^2 D^5} \tag{1.4}$$

the open-water efficiency η_O can then easily be computed from these quantities:

$$\eta_O = \frac{K_T}{K_Q} \frac{J}{2\pi} \tag{1.5}$$

As the operating environment of the propeller behind the ship is rather different from an unobstructed, free stream inflow, the open-water efficiency is not equal to the propulsive efficiency, as the interaction of hull and propeller still needs to be taken into account.

The fact that the propeller thrust required to propel the ship at a given velocity is not equal to the resistance the ship experiences without a running propeller at the same velocity, is the one of the major interaction effects. The velocities induced by the propeller lead to lower pressures on the aft part of the hull, thereby increasing the resistance. This explains that the thrust is always higher than the resistance of the hull without any propeller or propeller effect present. This discrepancy of forces is expressed by the *thrust deduction*, defined using the thrust T from the self-propelled condition and the hull resistance R_T from the towed condition:

$$t = 1 - \frac{R_T}{T} \tag{1.6}$$

Common values for t for cargo ships range approximately between 0.1 and 0.2. Quite different values might be encountered for ships equipped with propulsors other than screw propellers*.

As the propeller is operating in the wake of the hull, the inflow field differs considerably from the open-water condition. Mostly viscous effects lead to a non-uniform flow field behind the hull and the average flow velocity in the propeller plane is noticeably lower than the ship's speed. To quantify this, the average axial inflow velocity in the propeller disk v_A is used to define the nondimensional *effective wake fraction:*

$$w = 1 - \frac{v_A}{v_S} \tag{1.7}$$

* Eslamdoost et al. (2014) show and discuss how even negative values are possible for waterjet-driven ships, marking an exception from above statement that the thrust is always higher than the resistance.

Apart from the effective wake fraction, which in practice is determined from relating the known open-water characteristics of the propeller and the thrust and shaft speed measurements in self-propelled condition to find the corresponding v_A, other "types" of wake fractions are common in ship hydrodynamics and propeller design. This is described and dealt with in detail in Chapter 3.

The effect of thrust deduction and wake are then commonly and conveniently combined in the so-called *hull efficiency*. Skipping the derivation* for brevity, the hull efficiency is defined as

$$\eta_H = \frac{1-t}{1-w} \tag{1.8}$$

The hull efficiency covers the effect of hull-propeller interaction on the thrust-related part of the efficiency. But with the propeller working in the non-uniform inflow field, there is also a difference in the torque absorbed while delivering the same thrust as in a comparable open-water scenario, operating at the same advance ratio. Of course, this also affects the propulsive efficiency and is expressed by the *relative rotative efficiency* η_R which is commonly obtained from the ratio of the open-water torque Q_O and the torque in behind condition Q.

$$\eta_R = \frac{Q_O}{Q} \tag{1.9}$$

Combining the three individual components† described above, the propulsive efficiency can now be written as

$$\eta_D = \eta_O \cdot \eta_H \cdot \eta_R \tag{1.10}$$

Having defined a specific efficiency to optimize for and having defined a way to break it down, we can now go back one step to look at the propeller design problem as a whole.

The Ship Propeller Design Problem

There are several factors differentiating the design of ship propellers from, for example, the design of aircraft propellers or wind turbine blades. Only considering the obvious design objective of high efficiency for now, the key differences are only due to the application – rather than the underlying physics or design theory.

* Textbooks like van Manen et al. (1988) or Bertram (2012) describe this in detail.

† Both *hull efficiency* and *relative rotative efficiency* are not actual efficiencies in the physical sense. They often also reach values above unity. Few therefore use other designations, for example referring to them as *coefficients* instead.

Firstly, ship design differs substantially from typical design tasks and processes in other disciplines of engineering (cf. Watson 2002) in that usually only one ship is built to one design. This implies that no full scale prototypes exist. Small series of two to twenty hulls being built to the same design are not uncommon for certain types of vessels, but there might still be other differences affecting the propeller design among these ships, such as a different operational profile to design for, or different engine configurations.

Therefore a different propeller is needed for almost every ship, which is in stark contrast to e.g. the aerospace industry. This is also reflected in the length of design cycles, which are few weeks for ship propellers and in the order of years for similar products in other industries.

The second major difference is that the propeller typically operates behind the ship, leading to a strongly non-uniform inflow and strong interaction effects between hull and propeller. The operational profile and the optimization point or optimization range will naturally strongly affect the propeller design, too.

Cavitation

Apart from the aforementioned distinctive circumstances due to the propeller operating behind the ship, there is also a major physical difference that sets marine propellers apart from similar devices, such as aircraft propellers: The occurrence of *cavitation*.

Cavitation is the phenomenon of vapor cavities, or bubbles, being formed and present in a liquid due to high local velocities and corresponding low pressures. But it is not the presence of vapor in the liquid as such that poses a problem for engineering applications. It is the formation and collapse of these cavities that can even be violent enough to actually compromise the structural integrity of a flow-exposed structure like a propeller blade.

A propeller blade essentially being a rotating hydrofoil, it generates lift – and therefore thrust – by creating a pressure difference across the two sides of the blade, leading to an inherent risk of the local pressure falling below vapor pressure on parts of the suction side.

Given the large inflow velocity gradients typically encountered in a ship wake field, a given blade section experiences large variations in angle of attack over one revolution, increasing the risk of cavitation and making the intermittent occurrence of cavitation more likely.

Additionally, when the blade reaches the 12 o'clock position, the two main drivers for cavitation both happen to act strongest: The hydrostatic pressure reaches its minimum level, while the axial inflow velocity tends to be low at the same time, leading to a large angle of attack and low dynamic pressure on the suction side of the blade.

This situation already hints at the objectives of highest possible efficiency and moderate or controlled cavitation behaviour being in opposition. Avoiding cavitation at all times by designing for one extreme situation is likely to come at a price in terms of efficiency and vice versa.

Without going into detail here, one should be aware of the existence of different forms of cavitation. Cavitation types experienced on ship propellers range from smooth vapor sheets that detach and reattach again on the blade, over detached clouds and individual spherical bubbles to vortex cavities at the tip or hub. A good overview over the different characteristics and underlying physics is provided by Franc and Michel (2004). Kinnas (2010b) outlines the basics for the ship propeller case.

The Role of Cavitation in Propeller Design

As indicated previously, developing an optimum propeller means satisfying conflicting objectives and constraints. Designing a ship propeller providing optimum performance typically means finding a good trade-off between high efficiency and acceptable cavitation behavior in a range of operating conditions. The requirement for high efficiency is fairly straightforward, both in terms of motivation and definition. The objective – or constraint – of cavitation, however, often is rather vague. Exact metrics and thresholds are difficult to define and the level of what is considered "acceptable" might even depend on the designer's or customer's individual experience and preference.

Specifying "hard" metrics to quantify all aspects of the adverse effects of cavitation is desirable, but generally challenging due to the different nature of these effects. Typically, the main effects of cavitation considered in the performance evaluation are:

Efficiency – Efficiency loss, even complete thrust breakdown is possible in the case of very large cavitation extent.

Erosion – Structural damage and erosion of the propeller blade or the rudder due to the violent collapse of cavities close to the blade surface.

Comfort – Vibration and noise in the ship, affecting the health and working environment of passengers and persons working on the ship.

Environmental Concerns – While underwater noise has always been an issue for naval applications, such as submarines, the environmental aspect has gained important in recent years. Recently, an ITTC specialist committee has identified and acknowledged propeller cavitation as the dominant source of underwater noise over a wide range of frequencies affecting fish and marine mammals (Ciappi et al. 2014).

While it might be impossible to find one overarching measure for quantifying the overall harmfulness of cavitation, metrics and methods for quantifying most of these individual items exist and are usually applicable to both experimental and computational approaches alike.

The point of thrust breakdown, for example, can be predicted by any given thrust measurement technique, assuming the cavity develops properly in the experiment or simulation.

Pressure pulses on the hull causing noise and vibration can be measured as well. Usually, the signal at blade passing frequency is dominant, but strong signals at higher harmonics and broadband noise are often seen for cases with detaching cavities and vortex cavitation. Those forms of cavitation are typically highly unsteady and often only appear intermittently. Especially computing the higher-order and broadband signals requires very detailed and sophisticated approaches, as it is necessary to detailedly capture the cavity dynamics at small scales in space and time.

An experienced propeller designer might even be able to judge the harmfulness of cavitation based on the cavity pattern on the blade, even though this is still a largely subjective and experience-based technique. Reliable prediction of cavitation erosion based on rational methods, however, is very challenging both in experiments and simulations. The recommendations of the ITTC* suggest to "assess the erosiveness in model scale by assessing the cavitation at model scale", with the "assessment" step only being defined very vaguely, too.

Using different methods for estimating cavitation erosion on a hydrofoil, all of them based on detailed and computationally expensive LES simulations, Eskilsson and Bensow (2015) found large scatter between the methods and concluded that none of the methods used was able to deliver reliable results. While it is a very challenging problem, it is also an active field of research and significant improvement may be expected in the coming years. Simulations might then also become the key to reliable cavitation (erosion) predictions in full scale, as scaling from model scale to full scale remains a challenging issue.

Typical propeller design workflows today usually first consider efficiency, then cavitation and its effects, and lastly structural and strength issues. As in many other design situations in engineering, an iterative "spiral" approach is also common in propeller design (Praefke 2011). Starting the first design loop with very basic tools, the level of sophistication and detail of the tools used then increases while iterating.

Further complicating the situation of today's propeller designers is the fact that the hull design and propeller design typically are carried out by different

* ITTC 7.5-02-03-03.7, Prediction of Cavitation Erosion Damage for Unconventional Rudders or Rudders behind Highly-Loaded Propellers, Revision 00, 2008

parties. As today information on the hull geometry often is not shared with the propeller designer, simplifications and assumptions need to be made. Aiming for efficient designs that also satisfy requirements regarding cavitation and vibrations, designers still try to incorporate hull information earlier in the process now. But as information on the actual hull form is commonly very limited, strongly simplified methods (such as the method by Holden et al. 1980) are still needed and new ones even actively developed. Bodger et al. (2016) describe a simple approach to vibration control including the outline of the hull geometry in a very basic way.

Aims and Objectives of This Work

Previously described design problem including the influence of hull-propeller interaction and propeller cavitation shows the need for computational approaches and models of different levels of complexity.

This thesis describes fast, simple, and robust computational tools for the performance prediction of ship propellers – both with regard to efficiency and cavitation – in the behind-hull condition for application in design and analysis.

Using a hybrid approach of a potential flow-based model for the propeller flow and propeller forces, and using a viscous method for the hull flow, focus is placed on hull-propeller interaction and its potential impact on propeller design decisions. The propulsive efficiency can be determined from simulations employing such approach, and values for wake fraction, thrust deduction, and relative rotative efficiency are available individually. A partially-nonlinear cavitation model in the propeller analysis code is able to predict the occurrence of unsteady sheet cavitation with comparably small computational effort.

Especially obtaining the experimentally not measurable, yet decisive, complete effective wake distribution in a hybrid computational approach might allow for more insight into hull-propeller interaction and better numerical cavitation predictions and analyses at the design stage.

The methods developed in this work are applied to obtain effective wake fields and analyze the cavitation performance of conventional and Kappel propellers at the self-propulsion point behind the ship. From tests at model and full scale, Kappel propellers are known to have hull-propeller interaction characteristics different from conventional propellers (see the following section). This fact is still not fully understood today, but can be reproduced consistently in model tests. Also, cavitation behaviour and control has always been a challenge for these unconventional propellers. Implementing the methods outlined above and applying them in a coupled manner might help creating a better understanding of hull-propeller interaction and behind-ship cavitation performance of such propellers.

1.2 Kappel Propellers

Marine propellers with blade tips that are smoothly bent towards the suction side are known as "Kappel propellers", named after their original inventor, Mr. Jens J. Kappel. The concept and working principle is similar to that of winglets used on aircraft wings, which increase the lift-to-drag ratio. Interestingly, today's latest generation aircraft actually feature winglet designs that resemble typical Kappel propeller blade tips to an astonishing extent*.

After also exploring various other conceivable concepts of tip-modified propellers, Andersen and Andersen (1987) developed the theoretical basis and a method for designing such propellers. The main conclusion from that study was that an optimum tip-modified propeller should have a suction side-facing winglet that is smoothly integrated into the blade. This is still the defining geometry feature of Kappel propellers.

Both theoretical and practical work on this concept continued over the years. In a key publication on the topic, Andersen (1996) compared the performance of a Kappel propeller and a conventional propeller for a container ship, indicating a power reduction of about 4% using the Kappel propeller. Full scale service experience confirmed efficiency gains in that order (Andersen et al. 2005a).

Summarizing the results of a major research project which included extensive model testing of several systematically varied Kappel propellers and comparator propellers, Andersen et al. (2005b) come to several important conclusions that remain relevant to date:

In the cases considered, the Kappel propellers provided an increase in propulsive efficiency of about 4%. This total gain was attributed to both higher open water efficiencies and higher hull efficiencies. The increase in hull efficiency was achieved through larger effective wake fractions and unchanged thrust deduction factors.

Experiments in a large cavitation tunnel including the ship hull showed "somewhat different" (Andersen et al., ibid.) cavitation behaviour, with larger sheet cavity volumes and less stable sheets. Andersen et al. speculated that this was caused by hull-propeller interaction, as radial inflow velocity components lead to large changes in angle of attack for sections in the bent tip part of the blade. Given the increase in effective wake fraction observed in the self-propulsion tests for the same ship-propeller configurations, it even seems sensible to infer that differences exist in the effective wake distribution.

The differences in cavitation behavior and the challenges in cavitation control are described in more detail by Andersen et al. (2000), showing both experimental results and results from calculations based on two-dimensional theory.

* AIRBUS markets these new winglet shapes as "sharklets" to reflect this considerable design change over previous generations of winglets in the name as well.

1.3 Tools for Propeller Design and Analysis

This section gives a very brief overview of tools available and used for the hydrodynamic aspects of propeller design today. A more process-oriented illustration of contemporary propeller design in practice is outlined by Praefke (2011). The basic principles and procedures – usually based on experimental or empirical approaches but also applicable to numerical methods – are described in various textbooks. Bertram (2012) provides thorough explanations of these.

1.3.1 Empirical Estimation, Regression-based Methods

In order to get a first idea of the design, and to find a starting point for subsequent steps and design stages, empirical methods are still a popular and sensible choice. A number of design diagrams were established by using regression models on data gathered from series of open-water model tests, varying key blade geometry parameters systematically.

The *Wageningen B-Series* is probably the best known and most used propeller series. Originally published by Troost between 1938 and 1951, Oosterveld and van Oossanen (1975) provided the open-water characteristics in polynomial form, making them readily available for convenient use as a computer-based design tool.

Based on this, the open water characteristics of B-Series propellers can be obtained with negligible computational effort. Today, these data can and are still used to get first efficiency estimates or, for example, to estimate the effect of changing the number of blades or the blade area ratio on the efficiency.

1.3.2 Design Tools

Here, a method that finds the optimum propeller geometry for a given condition is referred to as a "design tool". The propeller with the optimum geometry will create the required thrust using minimum power. For a fixed shaft speed that means the lowest possible torque. According to the basic theory by Betz (1919), this can be simplified to finding the optimum radial load distribution for given thrust, propeller diameter, and propeller speed. Furthermore, the radial distributions of chord length, thickness, rake, and skew are common input to design programs. Output values are then radial distributions of pitch and camber, representing the radial distribution of loading.

Extending the earlier individual efforts by Betz, Goldstein, and Prandtl from around 1920, the work by Lerbs (1952) forms the basis for marine propeller optimization using lifting line theory and is still used today. This method is able to find the optimum radial distribution of circulation in radially varying

inflow. Combining the radial circulation distribution with the known two-dimensional section characteristics of e.g. airfoil series, the optimum geometry and the corresponding efficiency can be found. As long as the flow over the propeller blade sections can be considered largely two-dimensional, lifting line theory still serves as a valuable tool today. However, the results always need to be corrected for three-dimensional effects, and caution is required for propeller geometries that are known to cause pronounced three-dimensional flows, such as high-skew propellers.

While the lifting line approach concentrates the circulation to line vortices in spanwise direction, lifting surface methods, such as the vortex lattice method (VLM), also include the chordwise extent of the blade and the chordwise variation of circulation, as the singularities are placed on a reference surface instead of a line. Still, the two blade faces (suction and pressure side) are collapsed into one surface and the lattice of vortices is usually placed on the mean camber surface, so the method is linear with respect to blade thickness. A complete vortex lattice-based optimization method for ship propellers was first described by Greeley and Kerwin (1982), tools employing the method for more advanced applications emerged later, e.g. Coney (1989, including optimization for ducted propellers and multi-component propulsors) and Olsen (2001, with a focus on Kappel propellers).

Cavitation is usually neither modeled nor considered in the mentioned optimization methods. The designer can, however, modify the chord distribution accordingly and re-run the optimization when the pressure distribution on a certain section indicates a too high risk of cavitation.

1.3.3 Analysis Tools

In the analysis problem, the full blade geometry is already known and specified. Instead of dealing with finding the optimum geometry, now the flow around a given propeller at a given operating condition is of interest. Whereas above-mentioned optimization methods for design only consider a radially varying (circumferentially constant or averaged) inflow, analysis tools are usually employed to solve the unsteady problem including nonuniform inflow. Typical quantities of interest at this step are, among others, unsteady forces, temporal pressure fluctuations, and cavitation extent and cavitation dynamics.

Generally, the lifting line and lifting surface methods (such as the vortex lattice method, VLM) can also be formulated for the analysis problem. The landmark paper by Kerwin and Lee (1978) describes numerical lifting surface methods developed at MIT for the steady and unsteady analysis problems. Many of the methods and tools mentioned therein survive until the present day.

For example, the VLM code "MPUF-3A", that stems back to the initial development of unsteady propeller analysis programs at MIT in the 1980s (see Kinnas et al. 2003), is actually still popular and in active use. That particular code is even able to model unsteady sheet cavitation, but its cavitation model naturally inherits the basic limitations of the method and underlying assumptions.

The next step in complexity and completeness is the boundary element method (BEM, also "panel method"), which models the full blade geometry, including thickness. Chapter 2 of this thesis describes the general background of that method and the corresponding approach to cavitation modeling.

All of the previously mentioned methods are based on potential flow theory, representing a substantial simplification of the Navier–Stokes equations, neglecting viscosity, compressibility, and assuming irrotational fluid motion. These simplifications are reasonable to make at the design stage given the high-Reynolds number flow around the relatively thin propeller blades. Still, in the pursuit of better analyses and predictions, computationally much more expensive field methods making fewer assumptions and simplifications and capturing more of the actual physics are becoming more popular as well.

A "direct numerical solution" (DNS) of the Navier–Stokes equations is not feasible for complex engineering applications in the foreseeable future, therefore certain simplifications are still needed. These methods all fall in the "CFD" category (computational fluid dynamics), and today usually solve the incompressible Reynolds-averaged Navier–Stokes equations (RANS, both steady and unsteady), commonly using the finite-volume method. Increasing complexity further, and resolving larger eddies accurately while modeling subgrid-scale eddies, the current state of the art in high-fidelity simulation of propeller flows is "large eddy simulation" (LES, unsteady). To reduce the high computational cost of LES, a blended RANS-LES approach is also possible, this method is then referred to as "detached eddy simulation" (DES).

Whereas RANS-based CFD approaches are fast and robust enough to be routinely used in propeller analysis today, the computational effort associated with LES and DES simulations currently still limits their applicability to research work.

Cavitation can be modeled in all aforementioned CFD methods by a multiphase flow approach and special mass transfer models for the phase changes.

Field methods solving other than above equations exist, but are very rarely employed for ship propeller analysis. One of the rare examples is the recent paper by Budich et al. (2015) who solved the compressible Euler equations for detailed cavitation and cavitation erosion analysis.

1.3.4 Design using Analysis Tools

Leaving classical theory behind, one may also choose to base the design process on an analysis tool. In this case, no "design tool" that directly provides the optimum geometry for a given case is involved any longer. Rather, one tries to find the optimum by establishing knowledge from analyzing many geometries. This approach is particularly attractive for nonlinear optimization problems including multiple objectives and constraints.

For a practical application, usually parametric surface generation geared towards optimization (described for marine propellers by, e.g. Harries and Kather 1997) is coupled with an analysis tool, resulting in what is also referred to as "simulation-driven design". That means that after choosing a suitable tool from the previously described array of analysis methods, the performance of many automatically generated different propeller geometries is evaluated to select the best variant or to further drive a formal optimization based on optimization algorithms.

While this design approach is independent of the exact analysis method, choosing a computationally inexpensive analysis tool is particularly attractive to allow for a wider coverage of the design space in a given time. Still, one needs to ensure that the geometries created in this highly automated process – and the corresponding flow problem – are within the range of validity and applicability of the analysis method. The choice of the analysis tool must obviously allow for the reliable evaluation of the required objective functions. Otherwise, optimization algorithms might find and "exploit" limitations of the analysis tool, leading to sub-optimal results.

Integrated multi-stage optimization that uses analysis tools of increasing complexity in several stages is therefore an attractive option. Berger et al. (2014) solely use a panel code in the first stage, and a panel code coupled with a RANS solver (similar to the approach described in Chapter 3) in the second stage. One might choose to expand this further to validate the optimization results from a previous stage using a more advanced analysis method.

In another recent application of the simulation-driven approach, Gaggero et al. (2016) use a parametric, B-Spline-based geometry model and both a panel code and RANS-based CFD for the hydrodynamic analyses.

Assuming the method used for performance evaluation is capable of predicting all objective functions effects sufficiently well, the simulation-driven approach allows to optimize for multiple objectives in several operating conditions and account for multiple constraints at the same time. This is a major advantage over the classical design methods described in the previous section.

As this can require many thousand evaluations, even a strongly simplified and fast analysis program might become too "slow" at some point. For that

reason, the work by Vesting (2015, PhD thesis as paper collection) makes use of surrogate models for the performance analysis in combination with advanced optimization algorithms. While showing some promising trends, it remains crucial to remember that the success of analysis-based design will always also depend on the accuracy and reliability of the analysis tool employed.

Generally, it can be expected that this analysis-based approach to design will soon gain even more significance and complement the use of classical design methods, as computational resources become more and more affordable and as potentially suitable analysis tools with different levels of complexity exist already.

2 The Boundary Element Method for Ship Propeller Analysis

Taking the previously introduced vortex-lattice approach another step forward and introducing the blade thickness, one arrives at the physically most comprehensive potential flow model for propeller analysis in common use today. Boundary element methods (BEM), often also referred to as panel methods, have a lot in common with vortex-lattice methods for the analysis problem. But while vortex-lattice methods collapse the two blade faces into one and place the singularities on a reference surface that usually is the camber surface, panel methods are inherently nonlinear in this regard, as the singularities are placed on panels on the actual blade surface.

Only minor simplifications of the blade geometry are necessary for practical reasons in a robust implementation, such as zero trailing edge thickness and possibly an incomplete representation of the blade tip*. This means that the blade representation is complete from the blade root to sections very close to the tip, with all key design parameters, such as arbitrary radial distributions of chord length, pitch, skew, rake, camber, and thickness included. Also, no simplifications or assumptions regarding sectional profile shapes are required.

The panel method for three-dimensional steady lifting and non-lifting flows originated in the aircraft industry in the 1960s before being adopted to marine propellers in the 1980s. A decent summary of the general background and different applications is given both in the review by Hess (1990) and the textbook by Katz and Plotkin (2001).

Most of the development of panel methods for analysis of ship propellers has been documented in a number of PhD theses over the past two to three decades. Initially representing the state of the art in propeller hydrodynamics and implementing the most complete approach of potential flow methods, the method recently gained increased interest again. This is because of its – for today's standards – comparatively low computational effort while still offering

* For practical reasons, the blade is often cut at the tip (about 1% of the propeller radius) to avoid meshing issues and numerical problems at the singular tip point. Over the years there have been several efforts to improve the solution at the tip using specialized meshing techniques in the tip region, see e.g. Pyo (1995) or Baltazar et al. (2005), but they do not appear to be in widespread use today.

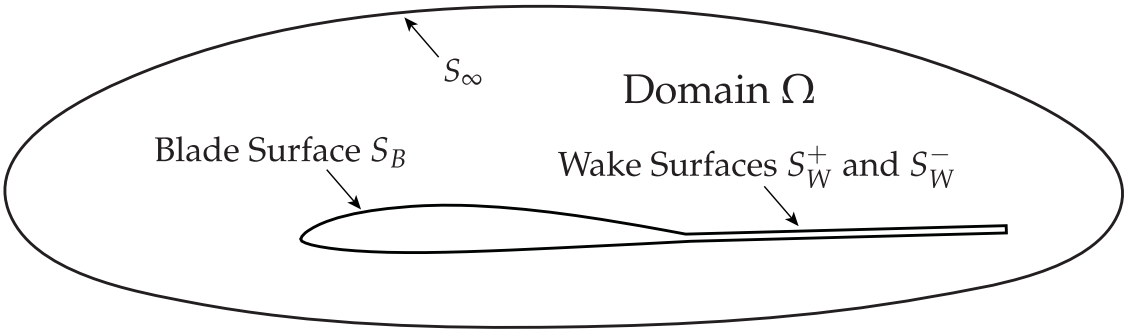

Figure 2.1: Domain Boundaries and Surface Definitions

a decent representation of the blade and the flow around it.

The thesis of Hsin (1990) documents the initial three-dimensional and unsteady panel code for ship propellers in non-uniform inflow developed at MIT. Not much later, Fine (1992) described a sheet cavitation model built on the panel method, a major step forward for propeller analysis. His approach was also used by Vaz (2005), who thoroughly studied this model in steady and unsteady cavitating flows using a panel method in two dimensions. Vaz's thesis also includes a chapter on steady, three-dimensional cavitating propellers and discusses several numerical and practical aspects of the implementation.

Apart from efforts of modeling sheet cavitation, some research has been carried out on modeling tip vortex cavitation using extensions of the boundary element method, see e.g. Szantyr (1994) and Lee and Kinnas (2001). The recent and comprehensive paper by Berger et al. (2016) also draws from these previous efforts and shows the state of the art with respect to potential flow-based modeling of tip vortex cavitation in the behind ship condition.

In his thesis describing another implementation of the unsteady panel method for ship propeller analysis, Hundemer (2013) outlines a simple model for determining the inception of tip vortex cavitation and describes a coupling of the panel code for hydrodynamic analysis with a finite element method-based tool for structural analysis.

In the scope of the present work, the sheet cavitation model described by Fine (1992) has been implemented for use in the behind-ship condition.

2.1 Mathematical Formulation

This section gives a very brief summary of the mathematical formulation and solution strategy of the boundary element method for propeller analysis as used for this thesis. Given that the concept of potential flow has been known and used for centuries, and the boundary element method has been known and used for decades, fundamental derivations and proofs of the governing equations are skipped here, and the interested reader is referred to textbooks, such as Newman (1977). The integral and discretized equations for the boundary element method are only given for the more general cavitating case as the formulation for the fully wetted, non-cavitating case is a subset of this, just dropping the appropriate terms.

2.1.1 Governing Equations and General Solution

For the present problem we generally assume inviscid, incompressible, and irrotational flow. This gives rise to the concept that the flow field can be expressed as the gradient of a scalar velocity potential Φ. The continuity equation then simplifies to the Laplace equation

$$\nabla^2 \Phi = 0 \tag{2.1}$$

As this equation is linear, multiple elementary solutions to it can be superposed and will still satisfy the equation. One can therefore generally solve the flow around an arbitrarily-shaped geometry by placing suitable singularities – usually both sources and dipoles (that are known elementary solutions to the Laplace equation) – on the body boundary.

This is based on a classic application of Green's theorem, stating that the potential inside a domain bound by a closed surface* can be expressed as a surface integral over the boundary. In the present case the domain Ω is bound by the closed surface $S = S_\infty + S_B + S_W$, as shown in Fig. 2.1. The two shown wake surfaces S_W^+ and S_W^- are in practice collapsed into one infinitely thin surface S_W.

Derivations of this can be found in general textbooks (e.g. Lamb 1932, Newman 1977, or Katz and Plotkin 2001, ranging from a more mathematical approach to an increasingly application-oriented view) or in more specific theses discussing the same method as implemented here, e.g. by Hundemer (2013, in German).

The linearity of the Laplace equation (2.1) is not only taken advantage of for constructing the geometry from elementary solutions, but also makes it

* Or multiple closed surfaces assumed to be connected by infinitesimal tubes, see Newman (1977).

simple to apply any geometry-independent inflow condition, whose potential satisfies (2.1). In the following, a notation is used that splits up the total potential Φ into a known onset part ϕ_{Onset} (dependent on the wake field with the local velocity $\boldsymbol{u}_{\text{Wake}}$ and the propeller rotation, the sum of those resulting in a local velocity vector $\boldsymbol{u}_{\text{Onset}} = \nabla\phi_{\text{Onset}}$) and a propeller geometry-dependent perturbation potential ϕ that is to be determined.

$$\Phi = \phi_{\text{Onset}} + \phi \tag{2.2}$$

In the non-cavitating case, a Neumann-type kinematic boundary condition (see p. 23) is to be imposed on the entire propeller blade. In the cavitating case, the dynamic boundary condition (see p. 26) applies on the cavity-covered region of the blade. Using these boundary conditions, the unknown potential ϕ from (2.2) can be found from solving the integral equations described in the following section.

Additionally, the Kutta condition needs to be enforced for the present lifting flow problem, requiring finite velocities at the trailing edge (see p. 31).

2.1.2 Integral Equations

Based on aforementioned general solution strategy of using Green's identities and exploiting the linearity of the governing equations, sources and dipoles are placed on the blade surface S_B. Only dipoles are placed on the infinitely thin wake surface S_W, unless the cavity extends beyond the blade into the wake. In that case additional sources are placed on the surface S_{CW} (see Fig. 2.2), representing the cavity thickness.

Note that S_{CW} only exists in case of supercavitation and the corresponding terms in the equations are dropped otherwise. The existence of a surface $S_{CB} \subset S_B$ in the case of partial cavitation, however, does not change the picture in the integral equations, as both dipoles and sources are present on the blade in any case.

Depending on where the potential is to be computed, the equations differ, as the field point needs to be excluded from the integration if it lies on the boundary. For the general case, this is well described by Newman (1977). A detailed description and derivation for the evaluation on the zero-thickness wake surface, which is required for (2.5), is provided by Fine (1992, Appendix A).

When setting up the equations to solve the problem, we are mainly interested in the two scenarios of the field point either lying on the blade or the wake surface, as these are the locations of the unknown singularity strengths.

Below formulations use Green's function $G(p, q)$, for brevity abbreviated to G in the following. Here p is the location of the field point where the potential

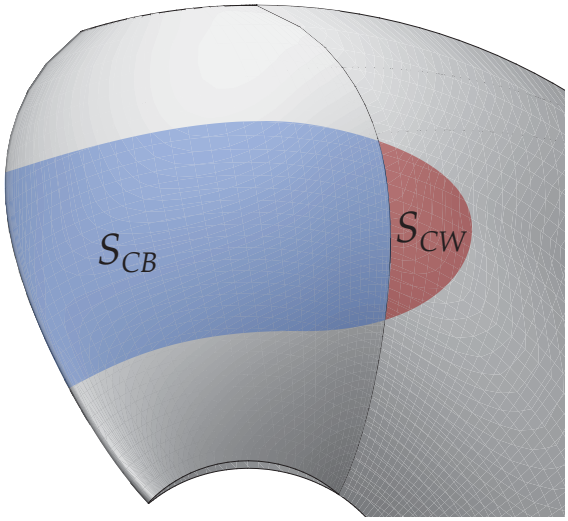

Figure 2.2: The cavitating parts of the blade and wake surfaces are subsets of the blade and wake surfaces, respectively: $S_{CB} \subset S_B$ and $S_{CW} \subset S_W$

is to be determined and q the location of the singularity. Then R is the distance in space between the points p and q.

$$G = G(\boldsymbol{p}, \boldsymbol{q}) = \frac{1}{|\boldsymbol{p} - \boldsymbol{q}|} = \frac{1}{R} \tag{2.3}$$

In the present problem, G can be interpreted as a continuous source distribution, and $\partial G/\partial n$ as a continuous dipole distribution.

Obviously, the signs of the individual terms in the equations depend on the definition of panel normal directions and the orientation of the dipoles. In the present implementation, the panel normal is pointing out of the fluid, into the body, as is visualized in Fig. 2.3. The dipoles are aligned with the panel normals and oriented such that the source part is located on the negative side (in normal direction) of the surface and the sink part is located on the positive face, which is somewhat counterintuitive. For the orientation on the wake, the suction side definition applies. These definitions are chosen to be in line with previous propeller codes at DTU.

Using all definitions from above, including Figs. 2.1, 2.2, and 2.3, the surface integral formulations based on Green's identities and the governing Laplace equation appear as follows for below two cases.

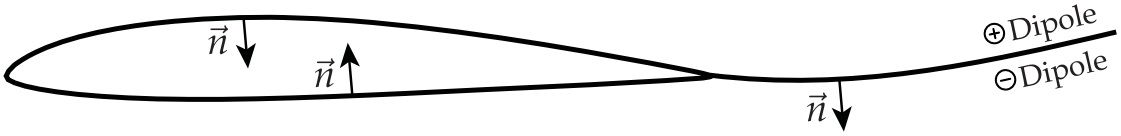

Figure 2.3: Definition of panel normals and dipole orientation

The potential ϕ_p on a point on the blade (the field point lies on the blade surface) can be found from

$$2\pi\phi_p = \int_{S_B} \left[\phi_q \frac{\partial G}{\partial n} - G\frac{\partial \phi_q}{\partial n}\right] dS - \int_{S_{CW}} \left[G\Delta\frac{\partial \phi_q}{\partial n}\right] dS + \int_{S_W} \left[\Delta\phi_q \frac{\partial G}{\partial n}\right] dS \quad (2.4)$$

And if the field point lies on the wake surface, the equation reads

$$\begin{aligned} 4\pi\phi_p^+ &= 2\pi\Delta\phi_q + \\ &+ \int_{S_B} \left[\phi_q \frac{\partial G}{\partial n} - G\frac{\partial \phi_q}{\partial n}\right] dS - \int_{S_{CW}} \left[G\Delta\frac{\partial \phi_q}{\partial n}\right] dS + \int_{S_W} \left[\Delta\phi_q \frac{\partial G}{\partial n}\right] dS \end{aligned} \quad (2.5)$$

In these equations, in line with the previously described interpretation of G, any terms $\partial\phi_q/\partial n$ represent source strengths, any ϕ_q represent dipole strengths, and any $\Delta\phi_q = \phi_q^+ - \phi_q^-$ are potential differences across the wake sheet.

Above equations (2.4) and (2.5) make use of the following abbreviations in the integrals over the wake surface, due to the fact that the single, collapsed wake surface still technically consists of two sheets.

$$\Delta\phi_q = \phi_q^+ - \phi_q^- \quad (2.6)$$

$$\Delta\frac{\partial \phi_q}{\partial n} = \frac{\partial \phi_q^+}{\partial n} - \frac{\partial \phi_q^-}{\partial n} \quad (2.7)$$

2.1.3 Discretized Equations

In order to solve the integral equations (2.4) and (2.5) for a specific problem, we aim at discretizing them to receive a set of algebraic equations, that can then be solved after applying the appropriate boundary conditions.

Both blade and wake geometry and the corresponding equations (2.4) and (2.5) are discretized on a structured mesh of quadrilateral panels (see Fig. 2.4, p. 25 for an example), again using all definitions and conventions from above.

Furthermore, it is assumed that all singularity strengths are constant over one panel. We then define the dipole strengths ϕ_j and the source strengths σ_j on

all panels. These being constant per panel, they are moved out of the integral terms $\int_{\text{Panel}}(\ldots)$. These integrals are then called influence coefficients – as they correspond to the influence of one panel with a constant, unit-strength source or dipole onto the center of another panel – and can be approximated numerically. Several schemes exist for this task and derivations and descriptions for classical examples can be found in the paper by Newman (1986), the thesis by Hsin (1990), or the textbooks by Bertram (2012) or Katz and Plotkin (2001).

In order to highlight the influence coefficients and the singularity strength coefficients in the equations, the integrals over the blade surface in Eq. (2.4) and (2.5) containing the source *and* dipole distributions are split up into two in the following.

If the field point is located on the blade surface, the influence of all singularities on the control point of blade panel i is computed. The discrete equation corresponding to (2.4) now reads

$$
\begin{aligned}
2\pi\phi_i = &\sum_{J_B}\left(-\phi_j \underbrace{\left(-\int_{\text{Panel}}\left[\frac{\partial G}{\partial n}\right] dS\right)}_{\boldsymbol{A}_{ij}}\right) + \sum_{J_B}\left(\sigma_j \underbrace{\left(-\int_{\text{Panel}}[G]\, dS\right)}_{\boldsymbol{B}_{ij}}\right) + \\
&+ \sum_{J^*_{CW}}\left(\sigma_{j^*} \underbrace{\left(-\int_{\text{Panel}}[G]\, dS\right)}_{\boldsymbol{C}_{ij^*}}\right) \quad - \sum_{J^*_W}\left(\Delta\phi_{j^*} \underbrace{\left(-\int_{\text{Panel}}\left[\frac{\partial G}{\partial n}\right] dS\right)}_{\boldsymbol{G}_{ij^*}}\right)
\end{aligned}
\tag{2.8}
$$

If the field point is located on the wake surface, i.e. the influence on wake panel i is computed, the discrete equation corresponding to (2.5) appears as

$$
\begin{aligned}
4\pi\phi_i^+ = &\; 2\pi\Delta\phi_{j^*} + \\
&+ \sum_{J_B}\left(-\phi_j \underbrace{\left(-\int_{\text{Panel}}\left[\frac{\partial G}{\partial n}\right] dS\right)}_{\boldsymbol{D}_{ij}}\right) + \sum_{J_B}\left(\sigma_j \underbrace{\left(-\int_{\text{Panel}}[G]\, dS\right)}_{\boldsymbol{E}_{ij}}\right) + \\
&+ \sum_{J^*_{CW}}\left(\sigma_{j^*} \underbrace{\left(-\int_{\text{Panel}}[G]\, dS\right)}_{\boldsymbol{F}_{ij^*}}\right) \quad - \sum_{J^*_W}\left(\Delta\phi_{j^*} \underbrace{\left(-\int_{\text{Panel}}\left[\frac{\partial G}{\partial n}\right] dS\right)}_{\boldsymbol{H}_{ij^*}}\right)
\end{aligned}
\tag{2.9}
$$

Note that the influence coefficients depend on both i (the panel the influence is computed on) and j (the influencing panel), as they contain Green's function $G = G(p, q)$ and that the negative sign is included in the influence coefficient

Name	Influence from	Influence on
$\boldsymbol{A}_{ij}$	Dipole on Blade Panel j	Blade Panel i
$\boldsymbol{B}_{ij}$	Source on Blade Panel j	Blade Panel i
$\boldsymbol{C}_{ij}$	Source on Wake Panel j	Blade Panel i
$\boldsymbol{D}_{ij}$	Dipole on Blade Panel j	Wake Panel i
$\boldsymbol{E}_{ij}$	Source on Blade Panel j	Wake Panel i
$\boldsymbol{F}_{ij}$	Source on Wake Panel j	Wake Panel i
$\boldsymbol{G}_{ij}$	Dipole on Wake Panel j	Blade Panel i
$\boldsymbol{H}_{ij}$	Dipole on Wake Panel j	Wake Panel i

Table 2.1: Summary and Naming Scheme of Influence Coefficient Matrices

matrices. Also note that the terms including contributions from a wake panel use the index j^* instead of j to emphasize the difference in blade and wake indices. While this is not necessary or of major importance at this conceptual stage, it is obviously vital to the implementation.

Introducing the numerically computed influence coefficients as matrices as indicated using the braces above (where matrix element ij is the influence from a unit-strength panel j on panel i, see Tab. 2.1) equation (2.8) may be written as compactly as

$$2\pi\phi_i = \sum_{J_B}\left(-\phi_j \boldsymbol{A}_{ij}\right) + \sum_{J_B}\left(\sigma_j \boldsymbol{B}_{ij}\right) + \sum_{J^*_{CW}}\left(\sigma_{j^*} \boldsymbol{C}_{ij^*}\right) - \sum_{J^*_W}\left(\Delta\phi_{j^*} \boldsymbol{G}_{ij^*}\right) \tag{2.10}$$

and (2.9) becomes

$$4\pi\phi_i^+ = \sum_{J_B}\left(-\phi_j \boldsymbol{D}_{ij}\right) + \sum_{J_B}\left(\sigma_j \boldsymbol{E}_{ij}\right) + \sum_{J^*_{CW}}\left(\sigma_{j^*} \boldsymbol{F}_{ij^*}\right) - \sum_{J^*_W}\left(\Delta\phi_{j^*} \boldsymbol{H}_{ij^*}\right) + 2\pi\Delta\phi_{j^*} \tag{2.11}$$

For convenience, the term $2\pi\phi_i$ from the left hand side of (2.10) is usually moved to the right hand side by adding this factor to the diagonal of $\boldsymbol{A}$ (elements $\boldsymbol{A}_{ii}$). The same principle is applied to the term $2\pi\Delta\phi_{j^*}$ in (2.11), which disappears as 2π gets included on the diagonal of $\boldsymbol{H}$.

For a z-bladed propeller with N chordwise panels (usually $N/2$ per face) and M spanwise panels per blade, there are now $J_B = zNM$ equations (2.10) to be solved. Equations of the second form, (2.11), are only required if there are unknown singularity strengths on the wake sheet, i.e. in the case of supercavitation. In that case, J^*_{CW} (the number of panels covered by S_{CW}) additional equations (2.11) emerge.

The singularity strengths on the non-cavitating wake surface S_W are assumed known. In practice, they are initialized with the blade circulation from the steady solution at the corresponding radius, and later contain the "time history" of the blade circulation, that is convected downstream in the unsteady method (see p. 31).

Kinematic Boundary Condition

The system of equations to be solved consists of one Eq. (2.10) for each blade panel and one Eq. (2.11) for each cavitating wake panel. For the non-cavitating case, the source strengths are known from the kinematic boundary condition, requiring that no fluid passes through the blade. In other words, the derivative of the perturbation potential in normal direction is equal and opposite to the normal component of the onset flow at each panel:

$$\begin{aligned} \nabla\Phi \cdot \boldsymbol{n} &= \boldsymbol{U}_{\text{Total}} \cdot \boldsymbol{n} = 0 \\ \boldsymbol{U}_{\text{Onset}} \cdot \boldsymbol{n} + \frac{\partial \phi}{\partial n} &= 0 \\ \frac{\partial \phi}{\partial n} &= -\boldsymbol{U}_{\text{Onset}} \cdot \boldsymbol{n} \end{aligned} \tag{2.12}$$

Applying this boundary condition to all blade panels in the non-cavitating condition, there are as many unknowns as equations. The source strengths are known from the local onset flow and the panel orientation and the dipole strengths are solved for.

In the cavitating case, dipole strengths remain the unknown and solved-for quantity on the wetted part of the blade, while the source strength becomes the unknown on the cavitating surface. In other words, a different boundary condition is needed on the cavitating part of the blade. This is discussed in the following section.

2.2 Cavitation Modeling Approach

The equations from the previous section obviously hold, no matter whether a non-cavitating (fully wetted) propeller, or a partially cavitating, or super-cavitating propeller is to be analyzed, as they were derived for the general case, with source and dipole distributions on the blades and the blade wake. Therefore, the main intention of this section is to provide some background on the boundary condition required on the cavitating surfaces, and to introduce the general approach to finding the cavity extent and thickness for a given cavitation number.

As mentioned earlier, the boundary element method is generally nonlinear with regard to blade thickness, as the kinematic boundary condition is fulfilled on the blade surface. This also makes it straightforward to obtain the source strengths from the kinematic boundary condition, (2.12). When modeling sheet cavitation on the propeller blade, however, we intend to do this in a *partially* nonlinear approach. This means that the boundary condition is still satisfied on the blade surface and not on the cavity surface, as the location of which is unknown *a priori*. By making this simplification, one avoids the expensive and possibly error-prone processes of remeshing (to adapt the mesh to the three-dimensional cavity shape) and recomputing influence coefficients, which is necessary after any geometry change.

Even in the cavitating case, most propellers are only partially cavitating, meaning there will be both wetted and cavitating panels on the blade. For the wetted parts, the aforementioned equations and the kinematic boundary condition still apply unchanged.

The method described here was initially described comprehensively by Fine (1992) and has since been implemented in several* BEM codes for propeller analysis. This section describes the approach and the key concepts behind the method to outline the working principle, its advantages, disadvantages, and implications. Details and derivations of, for example, the dynamic boundary condition on the wake, can be found in Fine (ibid.).

General Concept

As a cavity is characterized by having vapor pressure at the phase interface, a dynamic boundary condition is applied on the cavitating part of the blade, prescribing the total pressure to be equal to vapor pressure. As mentioned, this

* Initially in PROPCAV at MIT, development now continues at the University of Texas at Austin. Similar implementations:
- PROCAL (MARIN, see Vaz and Bosschers 2006),
- PANMARE (TU Hamburg-Harburg, see Bauer and Abdel-Maksoud 2012)

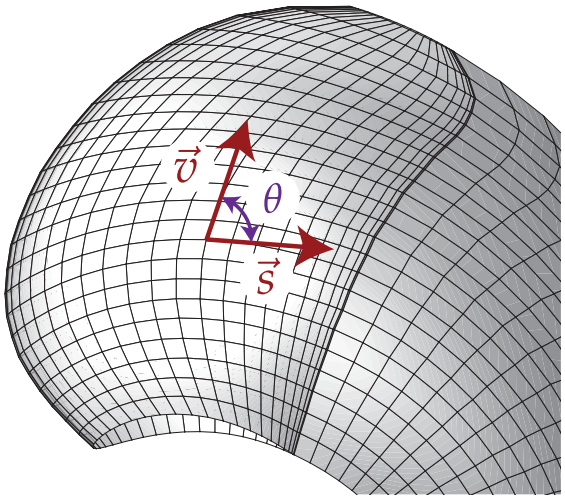

Figure 2.4: Directions of s and v in the curvilinear system on the blade

boundary condition is linearized in the sense that it is satisfied on the blade surface instead of the actual cavity surface. Fine (ibid.) discusses this difference in detail and shows that iterative remeshing, moving the blade mesh from the blade surface to the cavity surface to establish a fully nonlinear solution, is unnecessary as this yields a negligible increase in accuracy at very high computational cost.

It should be noted that the cavity shape is not found directly. The method requires a guess for the cavity extent (i.e. the vapor-covered region of the blade surface) and then solves the problem for a given cavitation number. After solving for the singularity strengths, the cavity thickness is then computed in a post-processing step.

Assuming the guess for the cavity extent is correct, the cavity thickness will be zero at the boundaries of the cavity, meaning that it detaches smoothly from the blade and reattaches smoothly again. If this is not the case, the cavity extent needs to be changed iteratively until the "correct" shape is found.

The approach described here relies on the blade being discretized on a structured mesh using quadrilaterals with the mesh lines aligned with the main flow direction. This, however, is a fair assumption to make as this is clearly the most common kind of meshing approach for boundary element methods for propeller analysis. On every spanwise strip* of the blade, a cavity *openness* is then defined as the thickness at the last cavitating panel. The converged solution describing the correct cavity shape requires the openness on all strips to be zero or below a defined threshold.

* A *strip* is defined as a set of panels having the same spanwise mesh index in the structured mesh, see Fig. 2.4 or Fig. 2.7.

Dynamic Boundary Condition

For obvious reasons the dynamic boundary condition on the cavitating part of the propeller blade – which prescribes the blade pressure below the cavity to be equal to vapor pressure – is based on Bernoulli's equation. Using a propeller-fixed coordinate system, a reference point far upstream on the propeller axis, and a point on the cavitating blade, it reads

$$p_0 + \frac{\rho}{2} |\boldsymbol{u}_{\text{Wake}}|^2 = \rho \frac{\partial \phi}{\partial t} + p_v + \frac{\rho}{2} \left(|\boldsymbol{v}_c| - \omega r \right)^2 + \rho g z \tag{2.13}$$

and is applied to find the "cavity velocity" $|\boldsymbol{v}_c|$ corresponding to the known vapor pressure p_v, ambient pressure at shaft depth p_0, onset flow ($\boldsymbol{u}_{\text{Onset}} = \boldsymbol{u}_{\text{Wake}} + \omega r$), and hydrostatic pressure ($\rho g z$, where z is the difference in submergence) at the point in question.

The "cavity velocity" found from Eq. (2.13) is then used to set up a Dirichlet boundary condition on the potential. Specifically, this is done by specifying the potential on the cavitating blade panels to be the chordwise-integrated cavity velocity plus the potential at the detachment point (see Fig. 2.5), which is assumed to be known.

A detailed derivation using velocities in the curvilinear coordinate system* established by the mesh on the blade (as shown in Fig. 2.4) can be found in Fine (ibid.) or the concise yet fairly complete review by Kinnas (2010a).

Skipping this derivation, but replacing the pressures p_0 and p_v by introducing the nondimensional cavitation number based on the propeller speed†

$$\sigma_n = \frac{p_0 - p_v}{\frac{\rho}{2} (nD)^2} \tag{2.14}$$

the derivative of the perturbation potential in chordwise direction (which is later integrated on each strip) can be written

$$\begin{aligned} \frac{\partial \phi}{\partial s} = & - U_s \\ & + \cos(\theta) \left(\frac{\partial \phi}{\partial v} + U_v \right) \\ & + \sin(\theta) \sqrt{(nD)^2 \sigma_n + |\boldsymbol{u}_{\text{Onset}}|^2 - \left(\frac{\partial \phi}{\partial v} + U_v \right)^2 - 2 \frac{\partial \phi}{\partial t} - 2 g z} \end{aligned} \tag{2.15}$$

where

* Ideally, the panel angle θ is close to 90° for large parts of the mesh, though.

† Of course, one can also define cavitation numbers based on other reference velocities, therefore this particular one is denoted σ_n.

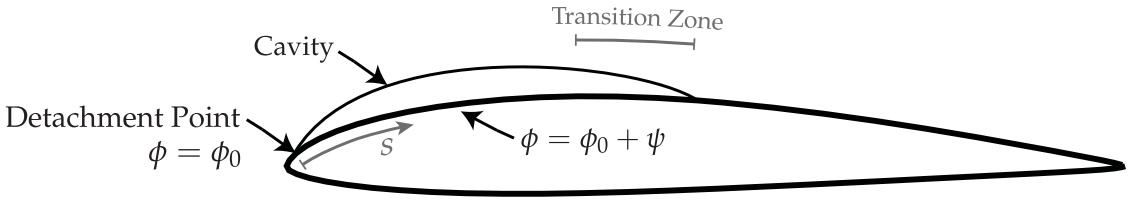

Figure 2.5: Potential on the cavitating part of the blade

U_s	Onset flow component in s-direction ($\boldsymbol{U}_{\text{Onset}} \cdot \vec{s}$)
U_v	Onset flow component in v-direction ($\boldsymbol{U}_{\text{Onset}} \cdot \vec{v}$)
θ	Angle between the s and v directions (see Fig. 2.4)
n	Propeller speed
D	Propeller diameter
σ_n	Cavitation number at shaft depth, reference velocity nD
g	Acceleration due to gravity
z	Vertical distance from shaft (positive up)

It must be noted that two quantities in (2.15) are assumed to be known but actually unknown at the time the boundary condition is set up: Both the perturbation component of the cross-flow term $\partial\phi/\partial v$ and the unsteady term $\partial\phi/\partial t$ are part of the solution and require an estimate value at this point.

Assuming that the potential at the detachment point of the cavity (see Fig. 2.5) is known, the potential on the cavitating part of the blade is then finally found by integrating Eq. (2.15) in chordwise direction from the detachment point ($s = 0$) to the point of interest ($s = s_p$, usually at the control point locations of the cavitating panels):

$$\phi = \phi_0 + \psi = \phi_0 + \int_0^{s_p} \frac{\partial \phi}{\partial s} \mathrm{d}s \tag{2.16}$$

This assumes that ϕ_0 is a known quantity, which it in fact is not. However, it can be expressed as an extrapolation of the known or solved-for potentials upstream. The extrapolation is necessary anyways, as $s = 0$ (the location of ϕ_0) is per definition located at a panel edge and quantities are computed at the panel control points. Fine (ibid.) proposes using third-order polynomial extrapolation for this, which has proven to work surprisingly well, despite the issues usually related to higher-order extrapolation.

At the aft end of the cavity, Kinnas and Fine (1990) (and also Fine 1992) propose the use of a "transition zone" (as indicated in Fig. 2.5) where the pressure inside the cavity recovers to the level on the wetted part of the blade. This is implemented by essentially relaxing the cavitation number in (2.15)

by a factor that depends on the relative chordwise position. While this entire assumption or the details of such pressure recovery law are debatable and provide material for separate lengthy discussions, the present implementation simply uses the transition law and the proposed constants by Kinnas and Fine (ibid.), resulting in a transition zone covering the last 15% of the cavity length on a given strip (Fig. 2.5 gives an indication but is not drawn to scale).

Cavity Thickness

As a Dirichlet boundary condition is applied to the cavitating panels by prescribing the potential according to (2.16), the unknown quantity or singularity strength that is solved for is now the source strength. That means that the vector of unknowns consists of a mix of unknown source and dipole strengths.

After solving the system of equations, the cavity height (or thickness) on each panel is determined in a "post-processing" step, as the position of the cavity surface depends on the then-known source strengths. The cavity thickness h is found from applying the kinematic boundary condition. The derivation in the curvilinear coordinate system is skipped again for brevity and the reader is once again referred to Fine (1992).

Using the same symbols and definitions as before, the resulting partial differential equation expressing the cavity thickness reads

$$\frac{\partial h}{\partial s}\left[V_s - \cos(\theta)\, V_v\right] + \frac{\partial h}{\partial v}\left[V_v - \cos(\theta)\, V_s\right] = \sin^2(\theta)\left(V_n - \frac{\partial h}{\partial t}\right) \tag{2.17}$$

containing the total velocities $V_s = U_s + \frac{\partial \phi}{\partial s}$, $V_v = U_v + \frac{\partial \phi}{\partial v}$, and $V_n = U_n + \frac{\partial \phi}{\partial n}$, the latter containing $\frac{\partial \phi}{\partial n}$, which, by definition, is the source strength.

In order to solve (2.17) numerically, Fine (ibid., p. 79) suggests to substitute the partial derivatives by backwards finite differences. In chordwise direction these are defined at the panel edges not the panel centers, leading to recursive substitution yielding a simple yet long expression. As this recursive approach also depends on previously computed quantities in chordwise and spanwise direction, this way of computing the cavity height is an inherently sequential process starting at the leading edge of the innermost strip, proceeding downstream and then outwards in spanwise direction.

Opposed to Fine (ibid.), the present implementation does not use any higher-order finite differences schemes when discretizing and solving (2.17). This decision was made to increase numerical stability and reduce numerical artifacts for cases including strongly inhomogeneous wake fields. The corresponding loss of accuracy was observed to be negligible for all practical cases.

2.3 Implementation

The method outlined in the previous sections has been implemented in a code named "ESPPRO" as part of the present work. The initial version of the program was developed and implemented at DTU between 2001–2003 and has now been extended to include the sheet cavitation model described in Section 2.2. This effort included rewriting all major computational routines and redesigning most data structures. For maximum portability, the code is now fully compliant with the Fortran 2008 standard, and is almost entirely self-contained, the widespread BLAS and LAPACK libraries* for linear algebra operations being the only examples of external dependencies.

2.3.1 Trailing Wake Geometry

The trailing vortices, also called blade wake or trailing wake, so far only appeared in earlier equations and sketches. The location and geometry of these wake sheets has been assumed known so far and has no influence on the equations to be solved. Still, the exact geometry and alignment of the blade wake with the flow has substantial influence on the results: Forces, induced velocities, and other quantities of interest strongly depend on the wake alignment.

Conceptually, it is easy to define how the blade wake should be formed and aligned. By assumption and definition, the wake sheet is a force-free surface, thereby required to be fully aligned with the flow.

Fulfilling this demand requires computing induced velocities in every of the wake sheets' mesh nodes, which are then to be displaced according to the total flow velocity vector. The induced velocities themselves, however, depend on the wake sheet geometry, thereby triggering a computationally expensive, iterative alignment procedure, which is even likely to suffer from numerical stability issues.

Therefore, many contemporary BEM implementations still make large simplifications, such as placing the trailing vortices on simple helicoidal surfaces. This is also valid for the present implementation at the time of writing. Also, a "frozen" wake geometry is assumed, i.e. it is not time dependent and does not change while the program is running.

Apart from the expected roll-up of the tip vortex and slipstream contraction, the wake pitch is one of the main characteristics. When using a simplified blade wake model without iterative alignment, the roll-up is commonly ignored

* See Lawson et al. (1979) for BLAS and Anderson et al. (1999) for LAPACK. Apart from the corresponding reference implementations, API-compatible, optimized libraries exist and are used for the present work.

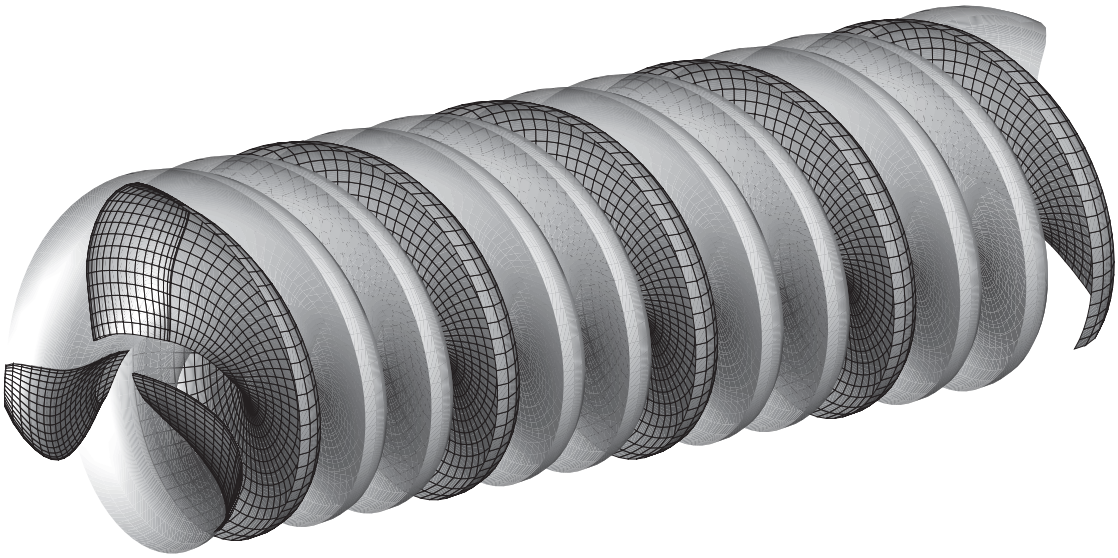

Figure 2.6: Typical Blade Wake Geometry for a Kappel Propeller
(Using Streckwall's model, mesh only shown on one wake sheet)

completely, while focus is placed on determining the wake pitch. Close to the blade's trailing edge, the pitch of the wake sheet is typically assumed to be equal to the pitch of the bisector of the blade section at the trailing edge. This initial wake pitch is usually kept in a "transition zone" extending about one propeller radius downstream the trailing edge, before changing the pitch to the ultimate wake pitch further downstream. This concept dates back to the blade wake modeling for steady-state vortex lattice models from the 1970's and 80's, for example described by Kerwin and Lee (1978) and Greeley and Kerwin (1982, Implemented in the code "PSF-2").

The current ESPPRO implementation defaults to the very simple and robust wake geometry model described by Streckwall (1998). This model does not account for slipstream contraction or other complex phenomena, and the ultimate wake pitch is only a function of advance ratio and blade pitch at a nondimensional radius of 0.9. Alternatively, the geometrically slightly more involved model of Hoshino (1989) is available, too, which additionally considers contraction and a stronger radial variation in ultimate wake pitch.

The alignment of the blade wake is still a subject of recent research, as it is a major cause of the limitations and limited applicability of the panel method. Highlighting some recent examples, Tian and Kinnas (2012) compared open water results from fully aligned wake and the previously mentioned classical model by Greeley and Kerwin (ibid.). Particularly for low advance ratios (and high loadings), the differences are substantial and the improvement

in predicted forces is considerable and promising. Focusing on hydrofoils instead of marine propellers, Wang et al. (2016) discuss numerical details of implementing a fully iterative wake alignment scheme for the steady case.

While a robust, accurate, and fast wake alignment scheme for propellers in strongly nonuniform inflow and at different loadings is highly desirable, no method fulfilling these requirements exists today.

2.3.2 Kutta Condition and Timestepping

The unsteady propeller problem using the Boundary Element Method is commonly solved in the way described by Hsin (1990), where the dipole strength $\Delta\phi$ of the wake panels is convected downstream as the blade rotates. The wake panels are commonly created so that their angular spacing corresponds to the blade angle increment ("timestep") $\Delta\theta$, making the process very simple. As mentioned in the previous section, the blade wake *geometry* is considered invariant in time, so it is only the onset flow and the wake dipole strength that vary over time, then posing the mathematical problem described before.

The potential jump on the wake sheet right behind the trailing edge corresponds to the potential difference of the aftmost panel on the blade's pressure side and suction side, which is part of the solution.

$$\Delta\phi_{\mathrm{TE}} = \phi^{+}_{\mathrm{TE}} - \phi^{-}_{\mathrm{TE}} \tag{2.18}$$

This difference is an approximation of the circulation at this radius and is released to the wake to be convected downstream as the blade turns, as indicated in Fig. 2.7. The figure also illustrates that the potential jump is actually known at the wake panel edges, not of the panel centers. The (constant) dipole strength of the wake panel is assumed to be the average of the values at the two edges.

The Kutta condition is enforced by substituting (2.18) directly into the system of equations, as described in detail by Hsin (ibid.). The first panel behind the blade is split up into multiple subpanels in streamwise direction, which are assigned varying dipole strengths to mimick an element with linearly changing dipole strength to decrease the influence of the timestep size on the solution. This technique also goes back to Hsin (ibid.).

Time-derivatives of the potential – as required for the computation of blade pressures using the unsteady Bernoulli equation – are determined using second-order backwards finite differences.

2.3.3 Setting up and Solving the System of Equations

Previously described approach results in a linear system of equations with a dense matrix on the left hand side (LHS) that depends on the geometry

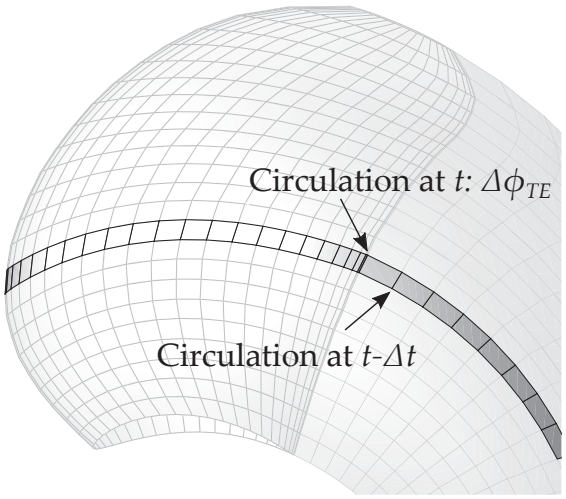

Figure 2.7: Convecting the circulation down the wake sheet

and the extent of cavitation. For the non-cavitating case and a "frozen" wake, the system matrix does therefore not change between timesteps, as Eq. (2.10) simplifies to

$$\phi_j \boldsymbol{A}_{ij} = \sigma_j \boldsymbol{B}_{ij} - \Delta\phi_{j^*} \boldsymbol{G}_{ij^*} \tag{2.19}$$

where all influence coefficient matrices are known and precomputed and the source strengths on right hand side are found from the kinematic boundary condition. For performance reasons, the matrix $\boldsymbol{A}$ can and should be factorized and stored as such in this case.

For the cavitating case, the LHS matrix changes after every change in cavity shape guess, as any panel j might change state from wetted to cavitating within the inner or outer* iterations, not only changing the structure of the matrix, but also leading to different unknown variables.

Baltazar and Falcão de Campos (2010) describe a technique to avoid updating the entire matrix in every inner iteration, and claim a 40-fold increase in speed for a steady, partially cavitating case. This technique, however, is not implemented in the present method.

Instead, the system of equations is set up from scratch in every single inner and outer iteration by assembling the LHS from precomputed influence coefficient matrices. It is then solved using a direct solver based on LU factorization (LAPACK's `GESV`). Vaz (2005) touches upon the possibility of using iterative solvers to improve performance, but mentions that this task is non-trivial due to the special matrix structures in the cavitating case. As the dynamic boundary

* Inner iterations: Iterations within one timestep to find the correct cavity shape
Outer iterations: Change in blade angle, new timestep

condition is based on an extrapolation of the detachment point potential, large off-diagonal terms are introduced to the final LHS matrix. In combination with the high condition numbers that are typical for propeller panel codes anyways (also see Hsin 1990), successful implementations using iterative solvers will probably require preconditioners adapted to this very specific problem.

Other implementation-specific means that have been realized in the present work to minimize calculation time are described in Section 2.3.5.

2.3.4 Cavitation Model Implementation Details

Assumptions for the Dynamic Boundary Condition

As mentioned on p. 26, two terms in the dynamic boundary condition (Eq. 2.15) have to be assumed known, even though they are actually part of the solution. Also, both these terms are part of the expression below the square root and have a negative sign. This is potentially dangerous, as (too) large values, estimates, or extrapolations for these terms might turn the entire expression negative.

First, there is the cross-flow term $\partial\phi/\partial v$. Even though this term is squared and then carries a negative sign, it is unlikely that it reaches a magnitude sufficiently large to blow up the square root term, as the total onset velocity vector magnitude (with positive sign) is also part of the expression.

Fine (1992) compared cavity shapes with and without this term included. The influence was found to be negligible for a simple hydrofoil case and noticeable but small for an actual propeller. Still, the term can easily be taken into account by using the value from the previous inner iteration, where it is computed with little additional effort (e.g. by spanwise central differences) in a postprocessing step.

Second, there is the unsteady term $\partial\phi/\partial t$. Special care needs to be taken here, as this term is included with a negative sign below the square root expression of Eq. (2.15), and there is no similar term with opposite sign. Fine (ibid.) suggests to extrapolate the value from previous timesteps, which led to instabilities and crashes in all practical cases (including a real blade geometry and a realistic ship wake field) investigated as part of the present work. Vaz (2005) suggests a less aggressive approach, that corresponds to using the local panel time derivatives from the previous revolution (at the same blade angle), where they are computed by backwards finite differences. Even though his work on unsteady cavitation was limited to two-dimensional cases, he still reported divergence for most cases using that approach for treatment of the unsteady terms. While still using the values from a previous cycle, the introduction of large underrelaxation factors is the solution suggested by Vaz (ibid.), coming at the cost of requiring many revolutions to be simulated.

As this is unpractical for an unsteady, three-dimensional analysis of a ship propeller in a wake field, a very simple approach was chosen to serve as the default in the present implementation. The cavitation model is only activated after at least one full revolution in the non-cavitating condition, where the unsteady terms are computed and stored for all panels and blade angles. After activating the cavitation model, the previously saved time-derivatives are applied on the wetted part of the blade, while $\partial\phi/\partial t$ is assumed zero inside the cavity. This is a substantial simplification and calls for further improvements in the future. While the directly-computed time derivatives inside the cavity are usually rather well-behaved, large changes can typically be observed in the reattachment zone, where one panel might change state from *cavitating* to *wetted* multiple times over a few timesteps. The very simple and very conservative approximation proved to be the only one of the methods investigated that ensured general stability and convergence of the inner iterations.

Split Panels

In the cavitation model described so far, a cavity always covers one or more entire panels. That means that a cavity – by definition – starts at a panel edge and closes (reattaches) at a panel edge. Unless the chordwise mesh resolution is very high, it is therefore unlikely, that the opennesses on all strips reach values small enough to consider the cavity "closed". For typical timestep sizes (blade angle increments of 1–5°) the wake panels have a "chordwise" extent that is easily ten times larger than the average chordwise length of a blade panel. To achieve acceptable opennesses, this essentially requires very small timesteps for supercavitating cases.

To relax the requirement on mesh resolution and to overcome the particular issues for supercavitation, Fine (ibid.) and Fine and Kinnas (1993) describe a "split panel technique" that splits the last cavitating panel of a strip into two. Using this technique, cavity lengths corresponding to a non-integer number of panels can be modeled, and the cavity can reattach at any chordwise position. On every split panel, the singularity strengths are no longer solved for, but rather extrapolated from the cavitating and the wetted part of the blade (or wake), thereby changing the number of equations in the system to be solved.

Extrapolations

Extrapolations play an important role in different parts of the cavitation modeling approach described. As mentioned, any extrapolations of unsteady terms are avoided in the present implementation. Also, the extrapolation order for the split panel quantities has been reduced (to either 0^{th} or 1^{th} order) compared

to the original method by Fine (ibid.), as the higher order extrapolations again proved to be unsuitable for all practical applications. The current implementation does, however, use the higher-order extrapolation for the potential at the cavity detachment point (see p. 27). This has proven to work well so far, but a "safer", yet accurate scheme, that avoids the obvious flaws of higher-order polynomial extrapolation, might improve the quality of the prediction. That is likely to be of particular interest for cases that exhibit mid-chord cavitation, which are possible to simulate, as the detachment point is arbitrary in the current implementation. Mid-chord cavitation prediction using a BEM is also described by Mueller and Kinnas (1999) and Young and Kinnas (2001) (using the PROPCAV implementation), but the extrapolations are not discussed therein.

2.3.5 Code Performance and Parallelization

When rewriting the computational routines of the code, particular focus was placed on computational efficiency, memory handling, general performance, and parallelization. While the aforementioned linear algebra libraries deliver excellent performance for common operations involving dense matrices as commonly encountered in panel methods, further measures can and need to be taken to achieve decent performance on modern computer architectures.

Based on observations from the computer development of the 1960s, Moore (1965) estimated that the number of transistors on processors would double every two years. This estimate is now commonly known as Moore's law, and it continues to hold so far. Along with the number of circuits, the clock speed of processors increased steadily until the mid-2000s, before several reasons – one of them power usage and related temperature and cooling issues – led to a halt of this trend (McCool et al. 2012). Since then, additional performance gains have been achieved through adding more parallelism on different levels to the hardware. Best known and most significantly, adding more computing cores to processors.

This large change – away from higher clock speeds and towards more parallelism – within only one decade has had serious implications on software development. Previously, almost any program would run considerably faster on newer computers. This is no longer true. Only programs that are designed to exploit parallelism on multiple levels will be able to benefit from the continuing increase in computing power. On the other hand, a program that *scales* is likely to benefit from future hardware in a similar fashion as sequential programs used to benefit from increasing clock speeds in the past.

While (parallel) code performance is a complex topic that depends on many

factors and details, there are some key metrics that help understand and quantify the theoretical parallel performance of a program. An obvious requirement for scalability is that parts of the problem at hand *can* be solved in parallel, as any serial work obviously limits the parallel scalability.

Originally described abstractly by Amdahl (1967), the following relationship between number of processors P, serial execution time $T(1)$, and the relative speedup S is now commonly known as Amdahl's law and can be used to estimate the "parallel fraction" f:

$$S(P) = \frac{T(1)}{T(P)} = \frac{1}{f/P + 1 - f} \tag{2.20}$$

Using the parallel fraction, one can also easily find the maximum theoretical speedup from Amdahl's law:

$$S(\infty) \leq \frac{1}{1-f} \tag{2.21}$$

This demonstrates that parallel fractions far beyond 90% are required to achieve decent speedups for common numbers of processors found even in consumer-grade computers. While modern compilers contain a number of automatic or implicit parallelization features, manual, explicit instructions will remain to be required to achieve optimum performance and scalability (McCool et al., ibid.).

For ESPPRO, explicit parallelization using OpenMP* is used for threading and vectorization. Given that computing the influence of one element on another point is a large part of the panel method, there is a lot of independent work that can be distributed among multiple threads to be executed in parallel. ESPPRO's parallel performance is shown in Fig. 2.8. According to Amdahl's law (2.20), the parallel fraction is close to 98% for a typical non-cavitating case (solid black line) and only 80% for a supercavitating case (dotted line).

To obtain the data, the entire program (initialization and steady calculation followed by an unsteady calculation covering two full revolutions) has been run with a varying number of threads on a Intel Xeon E5-2680 v2 processor, which has 10 physical cores and 20 virtual (logical) cores as it is capable of hyperthreading. The latter also explains the parallel performance degradation (and deviation from the theoretical estimate using the corresponding parallel fraction) beyond 10 threads, seen in Fig. 2.8.

In summary, the measures outlined briefly here increased the performance of the ESPPRO code significantly compared to earlier versions. Rewriting the

* Enabling multiprocessor parallelization on shared memory systems, as well as explicit SIMD (Single Instruction Multiple Data) instructions. See OpenMP ARB (2015)

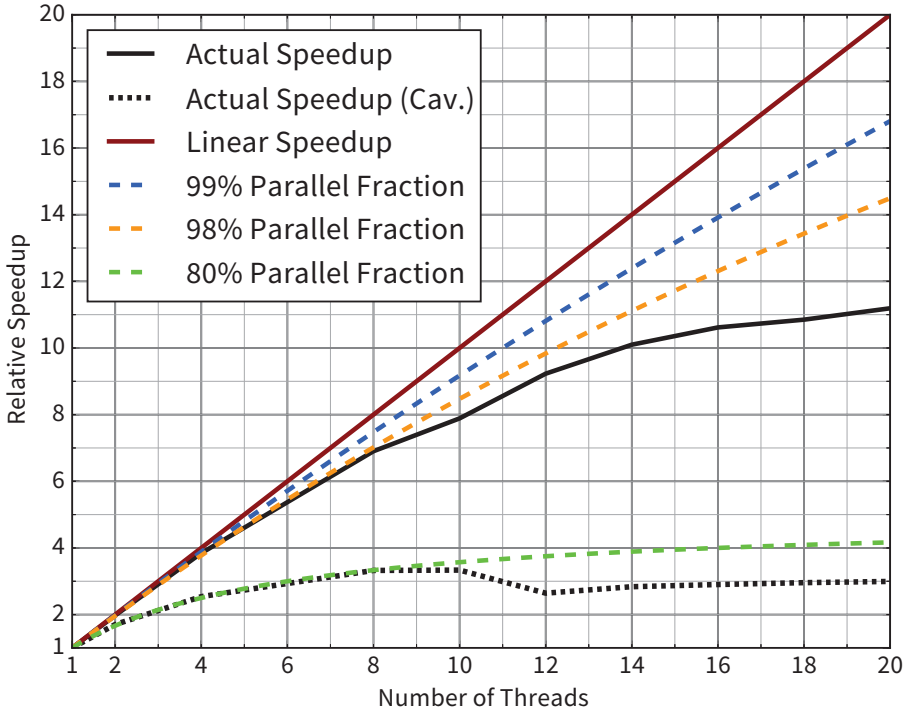

Figure 2.8: Parallel Speedup

computational routines using more precomputed and stored values, as well as more efficient memory handling, the serial performance increased by a factor of 5–50, depending on mesh resolution. Taking the parallel gains into account as well, the code typically executes about hundred times faster on a typical workstation today. Non-cavitating full scale cases can now be analyzed in real time.

The parallel fraction is considerably lower for the cavitating case, as the implementation of the cavitation model is less optimized so far and contains several inherently sequential operations, such as the computation of the cavity thickness (see p. 28).

While Amdahl's law and the parallel speedup for a representative case gives a good indication of the practical impact and advantage of the parallelization, it is not a definitive metric for the parallel performance. Amdahl's law describes the so-called "strong scaling", meaning the speedup by adding more processing units (PU) to solving a problem of fixed size.

When discussing parallel performance and scaling for a growing problem size, Amdahl's law is not necessarily central any longer. Assuming the amount of work *per PU* can be considered fixed, the problem size grows with the number of PUs added. Usually referred to as "weak scaling", Gustafson's law (Gustafson 1988) can give guidance on theoretical limits in this scenario.

For the application of panel codes to the ship propeller analysis problem, the problem size can, however, be considered fixed, as the method is known to converge rather quickly with increasing mesh resolution (Hsin 1990). Furthermore, numerical problems are likely to arise for too fine meshes, particularly at the thin sections close to the tip.

Other Practical Performance Aspects

For common problem sizes in propeller analysis, today's computers can easily store multiple influence coefficient matrices (see Tab. 2.1) in memory. Generally, the present implementation precomputes as many values as possible upon initialization, including all influence coefficients that can be expected to be used.

For values that are less likely to be used, a "lazy fetching" approach is employed. That means that a value is computed once needed and then stored for possible later use. This can save many unnecessary evaluations and many redundant re-evaluations of previously computed values. Especially when computing the quantities necessary for the integration of the dynamic boundary condition in the cavitating case, this technique saves considerable time. Obviously, it is vital to expire and reset those values once they become invalid, e.g. in a new timestep. A similar approach is taken for influence coefficients involving cavitating wake panels. As they are only needed in case a cavity extends beyond the blade, it usually does not pay off to precompute all of them.

When storing the influence coefficients contiguously and well-aligned in memory, considerable gains in computational efficiency are achieved when explicit SIMD instructions ("single instruction multiple data") can be used, i.e. vector instructions exploiting data level parallelism.

3 RANS-BEM Coupling

3.1 Background and General Concept

3.1.1 CFD in Calm Water Ship Hydrodynamics

In today's parlance of ship hydrodynamics, "computational fluid dynamics" (CFD) for computing the flow around the hull mostly refers to field methods solving the Reynolds-averaged Navier–Stokes equations, most commonly using a finite volume approach*. While more advanced methods like large-eddy simulation (LES) are also gaining some attention in the realm of academia, steady or unsteady RANS is today's workhorse for computing the viscous flow around ship hulls. The results and analyses from the "workshops on CFD in ship hydrodynamics" give an excellent overview over the state of the art.

The 2010 workshop held in Gothenburg (final analysis by Larsson et al. 2014) showed good overall results obtained by various RANS-based methods in prediction of resistance and propulsion quantities, as well as wake flow fields for a variety of cases, also demonstrating and documenting the increasing maturity of commercially available and affordable software packages. While the results from the workshop held in Tokyo in 2015 are still being analyzed in depth, preliminary conclusions confirm the notion that CFD can provide reliable results and is accurate enough to be ready to support hull design work when applied properly.

As numerical calm water ship hydrodynamics is reaching this degree of maturity, it leads to advanced simulation-based ship design becoming more and more useful, accessible, and widespread. There is also an increasing interest in optimizing for required propulsion power instead of bare hull resistance. Given that the optimization for required propulsion power may result in a different "optimum hull design" than a hull optimized for resistance† , efficient and accurate means of propeller modeling are becoming a key concern.

---

* See e.g. Ferziger and Perić (2002) for details of the finite volume method and the application to the RANS equations. See Larsson et al. (2014) for an overview of common contemporary tools, implementations and their numerical methods.

† This phenomenon has been reported multiple times in the past. Recently, Klinkenberg and Veldhuis (2016) described how a major design decision could go one way or the other, depending on resistance or power as the objective.

From a conceptual point of view, it appears easiest to treat the propeller the same way as the rest of the ship, fully resolving its geometry and applying an unsteady, e.g. RANS-based, CFD tool. An obvious advantage of this approach is that the propeller effect is modeled without the drawbacks of potential flow-based propeller analysis tools as described in the previous chapters, resulting in a consistent treatment of all flow-exposed components of the ship. Also, the propeller inflow field is inherently "correct" as no further assumptions or modeling are required. However, there is also a multitude of disadvantages with this conceptually simple, but practically rather involved approach:

When the ship is sailing in calm water, the flow around the hull can usually be treated as a steady-state problem. With the rotating propeller present, however, the entire simulation immediately requires an unsteady approach, even though time-averaged quantities might be enough in a hull and propeller design situation.

Furthermore, the propeller introduces components and local flow phenomena of scales that are very different from the flow around the bare hull. Therefore the propeller requires the time step for the entire simulation to be chosen much smaller than would be necessary for the rest of the ship. As a consequence, the computational effort does not only increase due to the increased number of cells, but also due to the time-accurate solution procedure that is not necessarily required by the engineering problem at hand.

Another potential drawback concerns the geometry preprocessing. Still-unknown geometry details at an early propeller design stage can often be smeared out for potential flow-based tools. Opposed to that, high-fidelity CFD requires a detailed, "watertight" propeller geometry to create a volume grid of sufficient quality around the propeller to be able run in a stable manner. The meshing step for the propeller itself is rather complex and requires additional computational effort and user experience. Also, some numerical approach for implementing the relative motion of different grids to each other (hull, propeller blades) needs to be chosen. For an unsteady, time-accurate solution, sliding mesh techniques and overset grids are two common methods.

Although some of these problems can be partly alleviated by automated processes and better-than-ever meshing tools, the increase in grid points and CPU time by adding the fully discretized propeller to the CFD calculation will always be substantial.

For above reasons, it is attractive to model the propeller effect without actually including the discretized propeller in the RANS problem. This is usually done by adding body forces to the cells covering the (imaginary) propeller volume in the RANS grid. Representing the propeller and modeling the propeller effect, those body forces simply appear as source terms in the

momentum equations. Writing the incompressible Navier–Stokes equations compactly by using Einstein's summation rule (as e.g. derived in Larsson and Raven 2010), the body force components F_i appear on the right hand side:

$$\frac{\partial u_i}{\partial t} + u_j \frac{\partial u_i}{\partial x_j} = -\frac{1}{\rho}\frac{\partial p}{\partial x_i} + \nu \frac{\partial^2 u_i}{\partial x_j \partial x_j} + F_i \tag{3.1}$$

This approach then poses the question of how to compute the body forces. Obviously, one can think of methods of any level of complexity. Commonly used models range from a inflow-independent linear actuator disk, to using a panel method as described in the previous chapter. No matter what exact model from this range of complexity is used, the propeller model providing the either steady, unsteady, or time-averaged body forces will only require very limited or even entirely negligible computational effort relative to the CFD calculation for the viscous flow around the hull. The latter combination of a RANS solver for the hull flow and a panel method for the propeller analysis is then commonly referred to as "RANS-BEM Coupling".

As the above-mentioned disadvantages of the approach using a discretized propeller are removed, the RANS-BEM approach is usually 1–2 orders of magnitude faster than an all-CFD simulation, while retaining all major ship-scale flow features and characteristics necessary and relevant for a self-propulsion simulation.

The general concept and the steps involved in a RANS-BEM coupling approach for propeller modeling are described in Section 3.1.3, p. 46f.

The propeller preprocessing in a RANS-BEM coupling method is considerably easier than for the all-CFD case. Instead of a highly stretched volume grid around the entire blade and hub, a much simpler to create panel mesh on the blade surface serves as input for the BEM, which can even change between iterations. For example, it is almost trivial to run a self-propulsion simulation with a controllable pitch propeller at constant revolutions. Also, replacing a stock propeller by a custom propeller design is straightforward and does not require any remeshing on the RANS side. After all, changing or moving the propeller only means assigning new body forces to different cells in the RANS grid.

Generally, the hybrid RANS-BEM approach is very well-suited for analyses on a global level, as, for example, encountered in hull form optimization. However, in most cases, is not the right tool to study detailed, small-scale flow features, in particular those located very close to the blades or downstream in the wake of the propeller. One should always keep in mind that the coupled approach using a potential flow-based propeller model providing the propeller forces makes a number of assumptions and simplifications of the physics

involved, and the overall quality and accuracy of the results obtained by a coupled approach depends on the quality of the propeller model itself.

Yet, it is also important to note that the RANS-BEM coupling can still provide the user – and the propeller designer in particular – with *more* information than the all-CFD approach, as will be described in the following section.

With the mentioned advantages at hand, the RANS-BEM coupling approach was recently called an "emerging trend" by the 27th ITTC's Specialist Committee on CFD in Marine Hydrodynamics (Hino et al. 2014, Presentation Slides*).

3.1.2 Effective Wake

Chapter 1 already introduced the concept and definition of the *hull efficiency*, that includes the *effective wake fraction*. This value is, as described, typically deduced from relating the results of open water and self-propulsion tests at model scale.

As it is rather common to use the term *wake* as a short form for different effects and quantities, like both *wake fraction* and *wake field*, depending on the context, this section defines some more terms and tries to highlight and clarify the key concepts behind them before going into more detail.

In the scope of this thesis, *wake fields* are always velocity distributions in the propeller plane or in a surface approximating the propeller plane. The *wake fraction* corresponding to a *wake field* is a measure of the volumetric mean axial velocity of the wake field relative to the ship speed and limited to the radial range of the propeller. For a field in polar coordinates with the spatially varying axial velocity $v_x = v_x(r, \theta)$, ship speed v_S, propeller hub radius r_H, and the propeller tip radius $R = D/2$, the wake fraction w is therefore defined as:

$$w = \frac{\int_{r_H}^{R} r \int_0^{2\pi} \left(1 - \frac{v_x}{v_S}\right) \mathrm{d}\theta \, \mathrm{d}r}{\pi \left(R^2 - r_H^2\right)} \tag{3.2}$$

Note that all figures visualizing wake fields in this thesis show *velocity* distributions, nondimensionalized by the ship speed, while $1 - v_x/v_S$ is the basis for the wake fraction.

As mentioned in Chapter 1, the term "wake field" is still not unambiguous, as different flow fields are of interest, for example with and without the propeller present. Even though below concepts are well-defined, one can find many publications† using ambiguous terminology. Therefore, the key concepts are

* Proceedings of the 27th ITTC, Volume III, p. 561

† For example, in the short section on propellers, the otherwise excellent textbook on marine

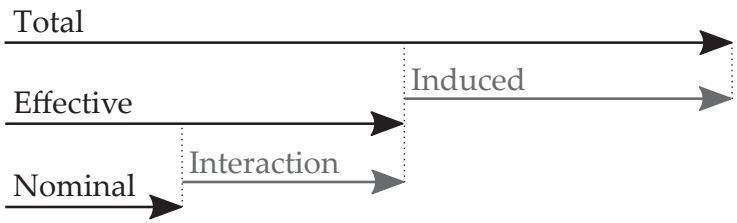

Figure 3.1: Conceptual representation of total, nominal, and effective velocities (As illustrated by Carlton 2012)

defined and described briefly again. Also note that below definitions apply to *wake* as in both *wake field* and the corresponding *wake fraction* according to (3.2):

The **nominal wake** corresponds to the velocity field in towed condition without any propeller or propeller effect present. By its nature the nominal wake field is independent of the propeller and often the only wake field that is recorded in experiments and provided to the propeller designer. It is routinely measured in model scale, but not measurable with reasonable effort in full scale (as one would have to tow the ship without a propeller at an appropriate loading condition while measuring the flow field). The measurability of this and other types of wake fields is summarized in Tab. 3.1.

The full scale experiments are generally difficult to execute, therefore the table shows the corresponding symbols in parentheses, only indicating whether measurements are possible with somewhat reasonable effort. Also note that the table would look differently for wake *fractions* derived from methods that do not require or compute the entire field.

The **total wake** is encountered when observing the actual, total flow with a working propeller. It includes the propeller-induced velocities. The presence of the rotating blades makes it more difficult to measure over the entire propeller disk, but there is no conceptual reason that makes it impossible. Today, nominal wake fields are still commonly measured using Pitot tubes, whereas non-intrusive optical methods like Laser Doppler Anemometry (LDA) or Particle Image Velocimetry (PIV) are usually preferred or required approaches for total wake measurements. Recently, Kleinwächter et al. (2016) reported full-scale total wake measurements using PIV, demonstrating the feasibility of carrying out such measurements. However, velocities were only measured in a fraction of the propeller disk, relatively close to the hull.

Lastly, the **effective wake** corresponds to a purely imaginary or conceptual type of velocity field. It is the velocity field as "felt" by the propeller, containing

hydrodynamics by Newman (1977) does not make the necessary differentiations between types of wake fields. Also, even some recent ITTC guidelines contain unclear or contradictory use of these terms.

the velocities related to hull-propeller interaction, but excluding the purely propeller-induced velocities. The mean axial velocity of this field – the effective wake *fraction* – is easily found from open water and self-propulsion tests, the distribution of velocities in the propeller plane, however, is usually not known.

Theoretically, there are two ways of obtaining the effective wake field, as can be seen from Fig. 3.1: Either the interaction velocities are added to the nominal field, or the propeller-induced velocities are subtracted from the total wake field. No matter which approach is used, this fictitious field is impossible to determine directly from experiments at any scale as neither the interaction velocities nor the purely propeller-induced velocities can be measured.

While being difficult to compute or measure, the effective wake field is of great importance to the propeller designer, as it represents the actual inflow field to the propeller. Also, it is the inflow field that needs to be used for any analyses regarding behind-ship performance or behind-ship cavitation behaviour when not including the hull in the same simulation.

When using a CFD approach with the complete hull and a discretized propeller, the propeller inherently experiences the right inflow, as all interactions of hull and propeller are part of the simulation. But as the induced velocities are not known explicitly, the effective wake field can not be *extracted* from such method. This leads to another key advantage of using a propeller model as done in a RANS-BEM coupling approach: Any onset flow can be specified in the propeller panel code and at the same time, the induced velocities from each blade and wake panel are available in an isolated way, allowing for calculation of the effective wake field.

In the present work, effective wake fields are always found from the difference of the total wake field and the propeller-induced velocity field, using the total wake field from the RANS part of the simulation and the induced velocities from the BEM. The coupling of the two programs is described in the following sections.

The existence of the effective wake field and the related issues have been known for a long time, but due to the complexity of problem (both on the hull side, the propeller side, and the interaction itself), it has only been "solved" properly for realistic hull and propeller geometries very recently.

Theoretical approaches also using iterative coupling of models for hull and propeller flow have been developed decades before (cf. Huang and Groves 1980, Dyne 1980), but usually either their hull or propeller representation was not sufficient for practical purposes. Yet, these methods offered interesting hints, as, for example, Huang and Groves (ibid.) could demonstrate that the common assumption that the effective wake distribution is similar to a uniformly scaled version of the nominal field is not appropriate.

Method	Scale	Nominal	Total	Effective
Experiment	Model	✓	✓	–
	Full	(–)	(✓)	–
All-RANS	Model	✓	✓	–
	Full	✓	✓	–
RANS-BEM Coupling	Model	✓	✓	✓
	Full	✓	✓	✓

Table 3.1: Measurability of different types of wake fields

The effective wake problem gained increasing interest in the 1980s when more numerical tools and computer programs made their way into propeller design and nominal wake fields were forming the key input. Dyne (1980) describes the related problems when designing "wake-adapted" propellers, and the nominal vs. effective wake issue is also acknowledged by Kerwin (1986) in his review paper.

Most of the relatively few theoretical and experimental efforts towards obtaining the effective wake distribution have aimed at simplified hull geometries like axisymmetric bodies while using an actual propeller. Opposed to that, Hoekstra (1977) employed a very interesting approach involving a realistic ship model and a simplified propeller, instead. Using a geometrically simple axisymmetric diffuser to represent the propeller in the towing tank-scale experiment, he measured the total velocity field upstream of the "propeller" and computed the velocity field induced by the diffuser based on actuator disk theory. The difference of the two then obviously leads to the effective wake field. Still, no later applications of similar experimental methods are known to the author and none of them are in regular use today.

3.1.3 General Concept

The general concept of RANS-BEM coupling described in this section is applicable to all contemporary methods mentioned and reviewed in the following section and to the version implemented as part of this work, described in the section thereafter. Minor differences between different implementations might exist on a lower level, but below steps form the basis for the approach.

1. Run the unsteady propeller model (BEM) in an initial guess of the effective wake field. The nominal wake field might be a good starting point.
   a) Compute the purely propeller-induced velocities in the coupling plane from the singularities in the BEM and store them for later use.
   b) Convert the blade panel forces to volume forces in the RANS grid.
2. Apply the propeller forces to the RANS problem and run the solver until the effect of the forces on the flow converges.
3. Extract the total velocities in the coupling plane from the RANS code.
4. Subtract the induced velocities known from the previous BEM run from the total velocities to obtain the effective wake field.
5. Re-run the BEM in the effective wake field and update the induced velocities (Step 1a) and propeller forces (Step 1b) and proceed with Step 2.

As is apparent from these basic steps, this coupling method is of iterative character and the steps need to be repeated until convergence, i.e. the effective wake field does not change significantly between two coupling iterations. The exact number of iterations required will strongly depend on the kind of the analysis problem (fixed propeller speed or self-propulsion), the RANS solver, and details of the implementation (e.g. propeller force underrelaxation, the coupling frequency in terms of RANS iterations, ...) of the coupling. Typically, however, convergence is achieved after few (about 3–10) iterations.

The key issue for the RANS-BEM coupling approach is related to the location of the coupling plane. Ideally, one would like to compute the effective wake in the exact location of the control points in the propeller panel code, or at least in the propeller plane. This is not possible, as the BEM works by placing singularities on the blade surface, resulting in infinite induced velocities in the immediate vicinity of the panels.

RANS-BEM coupling can be applied in both steady and unsteady RANS approaches. For steady approaches, the unsteady propeller forces and induced velocities from the BEM are to be time-averaged. As mentioned before, the steady-state procedure is usually sufficient for calm water self-propulsion, but the unsteady approach also allows for more advanced applications (also see p. 50).

3.2 Literature Review

Representing the effect of a propeller by body forces inside a viscous flow simulation is a rather obvious solution to simplifying this complex problem and its first application already dates back about 40 years (see Schetz and Favin 1977 and subsequent papers by the same authors). In this early application and simple approach, however, the propeller forces were independent of the actual inflow – therefore not changing or being updated as the flow evolves – and usually at least circumferentially constant.

One decade later, a key step forward was presented in the important work by Stern et al. (1988), who first described a two-way, iterative coupling of a viscous flow solver for the flow around a ship hull and an inviscid propeller code, including all key concepts of the process described in the previous section. Given the very limited computing power for this kind of task and the fact that RANS solvers were not yet able to reliably compute the complex flow around ship sterns, axisymmetric bodies or very simple three-dimensional shapes represented the ship hull, therefore rather providing a proof-of-concept than a tool for ship and propeller design at that time. In this original work, the propeller model providing forces and induced velocities was based on a vortex-lattice code, at that point representing the most advanced method for ship propeller analysis.

Only a few years later, Zhang et al. (1991) presented an iteratively coupled body force propeller model operating behind a slender variant of the Series 60 hull at model scale. That work can be considered the first application of a hybrid method to a case involving both an actual ship and propeller. The hull flow was computed by a single-block RANS solver and propeller forces and induced velocities were computed from lifting line theory. Even though this particular method was based on and implemented in the early versions of SHIPFLOW, it should be noted that the RANS solver involved was *not* XCHAP, but an earlier, now discontinued, solver. Still, a very similar method still serves as the default propeller model in SHIPFLOW today.

Still being constrained by computer resources, the work by Kerwin et al. (1994) used a combination of an axisymmetric part for the hull flow and a non-axisymmetric part for the propeller flow. Based on this, they describe an interesting design and optimization procedure for wake-adapted ducted propellers, thereby proving the power and usefulness of such coupled methods.

As both CFD and the body force-based propeller representation slowly gained maturity, it was increasingly used for three-dimensional cases involving more strongly non-uniform inflow, such as open-water cases with an inclined shaft setup (Choi and Kinnas 2001). This particular study used an Euler solver

coupled to a vortex-lattice method, with the latter also including a sheet cavitation model. Apart from the inclined shaft case, the paper also provides results for an axisymmetric case and compares the total velocity field and cavity patterns with experiments, showing that the coupled approach can deliver good accuracy at reasonable computational effort.

With the advent of mature RANS codes and simulations becoming feasible for real ship geometries at model and full scale, the strategy of coupling a potential flow-based propeller code gained a lot in popularity for the key task of enabling numerical self-propulsion tests. By the time of the Gothenburg 2010 workshop on ship hydrodynamics*, several implementations of viscous/inviscid coupling approaches existed, some still relying on lifting line or vortex-lattice propeller representations, others using panel codes (BEM) for this task.

Starke et al. (2010) describe the method that is now routinely used† within design studies and hull optimization at MARIN. More detail on their method and implementation is given by Starke and Bosschers (2012), who not only analyze scale effects in powering prediction using the method, but also discuss important details regarding the selection of the coupling plane and the computation of induced velocities in the panel code:

Starke and Bosschers (ibid.) highlight the discrepancies in the representation of the propeller blades in RANS and BEM, as only the blade-associated forces acting on the fluid are modeled on the RANS side. Lacking the blades as such, the displacement effect of the blades is consequently not accounted for. On the other side, the blade thickness is represented by sources in the BEM, fulfilling the kinematic boundary condition on the blade surface. Starke and Bosschers (ibid.) therefore propose to only use the dipole contributions from the blade panels when computing the induced velocities. This issue was then revisited and investigated in depth by Hally (2015), who compared the aforementioned approach with a method that computes the induced velocities from all singularities present in the BEM and then accounts for the displacement effect by introducing source terms in the continuity equation in the RANS solver. The magnitude of these mass source terms is proportional to the strength of the blade sources in the BEM. Hally concluded that both methods – either excluding the source contributions or adding mass sources – essentially work equally well and reports differences in effective wake fraction and thrust and torque coefficients for the KCS self-propulsion case of $\pm 0.2\%$ when comparing the results of the two approaches.

While earlier applications using simplified hulls or open water configura-

* See the final workshop assessment by Larsson et al. (2014).
† See for example Klinkenberg and Veldhuis (2016).

tions (e.g. Choi and Kinnas 2001) explicitly mentioned that the coupling plane location is not of high importance, Starke and Bosschers (ibid.) found the opposite to be true when the propeller is operating behind the ship. They emphasized the importance of the location of the coupling plane and demonstrated the effect strikingly by showing the change in effective wake fraction, thrust deduction, and propeller speed at the self-propulsion point when varying the distance between propeller and coupling plane. As appears intuitive and sensible, the effective wake fraction increases – and thereby the propeller speed in self-propulsion decreases – as the coupling plane is moved further upstream, further away from the propeller, and closer to the hull. As a consequence, they propose to extrapolate the effective wake field from two planes upstream of the propeller plane and, using this method, yield better agreement with experimental results.

Following up on the work from their colleagues, Rijpkema et al. (2013) elaborate further on the importance of the coupling plane choice and extend the method to use a curved upstream surface that follows the contour of the propeller blade's leading edge. This way, the coupling plane can be placed as close to the propeller blades as possible while avoiding intersections with the blade panels.

The MSc thesis by Rotte (2015) revisits these important contributions from researchers at MARIN and provides some additional interesting findings and examples using the same programs and approach.

Meanwhile, Tian et al. (2014) derived a way to compute the induced velocities in the control points of a vortex-lattice method (VLM), removing the need for any extrapolation, as the effective wake can be calculated in exactly the points where it is required for the computation. That approach is used in an interesting way by Tian and Kinnas (2015), who used a RANS-VLM coupling to get the effective wake in the propeller plane and then employed the more advanced BEM for the actual analysis and cavitation simulation.

In a different approach to increase the accuracy of the effective wake prediction, Sánchez-Caja et al. (2015) suggest to introduce correction factors that correct for the discrepancies introduced by the different assumptions made by RANS and the potential flow-based propeller model. In an open water case the effective velocities in the entire flow domain should always be identical to the initial uniform parallel inflow, as – by definition – the propeller-induced velocities are the only disturbance. Technically, this should hold for any coupling plane approach and location. Due to the different assumptions and simplifications in RANS and potential flow, the velocities induced by the force field on the RANS side, and the induced velocities as computed directly in the BEM, are usually not identical. One might be able to achieve very good agreement

and negligible discrepancies close to the design point, but it is likely that these discrepancies vary over the operational range. The correction factors proposed by Sánchez-Caja et al. (ibid.) are derived from those open water effective wake discrepancies to be later applied to correct the effective ship wake field.

Beyond these measures to obtain the best possible accuracy for numerical self-propulsion results, several papers (e.g. Berger 2011 and Tian et al. 2014) focus on details of the mapping of panel forces to RANS cell forces. This is particularly challenging in the case of unstructured volume grids that might even be distributed across several processes, as parallel solvers are employed. On a slightly more general level is the question of whether every force vector per BEM panel is transferred to the RANS grid (probably the most common approach, explicitly mentioned in Wöckner et al. 2011) or whether all blade panel forces (from both suction and pressure side) are first projected on the camber surface before being mapped to the CFD grid, as described by Starke and Bosschers (2012).

RANS-BEM coupling implementations exist for both steady and unsteady approaches to the hull flow problem. Using a Vortex-Lattice propeller code and an Euler solver, Choi and Kinnas (2003) computed both steady and unsteady effective wake fields, concluding that the difference between the time-average of the unsteady fields and the steady field is very small.

As of 2014, the officially recommended procedures and guidelines of the ITTC also mention* the general concept of using a propeller model exchanging velocities and forces instead of using a discretized propeller in CFD, but do not go into further detail.

Applications

The number one application for RANS-BEM coupling methods is clearly the problem of power prediction by means of a numerical self-propulsion test. Still, thanks to the flexibility and versatility of the method, a number of more advanced applications have been reported.

Greve et al. (2012) applied the method for simulating self-propulsion of a pod-driven ship in waves. This was later (Greve and Abdel-Maksoud 2015) extended to include partially emerged, ventilated propellers and their interaction with the free surface.

Martin et al. (2015a) describe advanced unsteady manoeuvring simulations of a navy submarine. Simulations were carried out with both a discretized propeller and a VLM-based body force model for comparison. The key results

* ITTC Recommended Procedures and Guidelines: *Practical Guidelines for Ship Self-Propulsion CFD, Revision 00, 2014.*

of the two approaches are very similar but the propeller model reduced the number of cells by more than 20% (which is a typical number if the hull is included) which results in considerably shorter CPU time. The same authors focused on comparing the propeller open-water results in oblique inflow using a full RANS propeller and the RANS-VLM propeller in Martin et al. (2015b). Even though the agreement is fair, Martin et al. indicate that a bug in their implementation might have caused worse agreement than expected.

3.3 Implementation

As part of the present work, the RANS-BEM coupling concept has been implemented on the basis of the DTU-developed propeller analysis code "ESPPRO" (see Chapter 2) and the commercial CFD package SHIPFLOW (Flowtech 2016). Specifically, the finite volume-based, steady-state RANS solver "XCHAP" from the SHIPFLOW package is used, which has been extensively validated for ship stern flows and ship wake prediction*. XCHAP requires structured grids and uses the overlapping grid technique to conveniently represent complex geometries as, for example, appendages such as rudders in structured grids.

In XCHAP, body force propellers get their own (usually cylindrical) grid, thereby entirely separating the hull and gridding part from the propeller. This also simplifies the force transfer from panel forces to RANS cells. The present implementation uses unmodified versions of both XCHAP and ESPPRO and uses an additional program to ensure communication and data transfer between the two. The interface also takes care of all required conversions of input and output files, and additional steps like time-averaging and smoothing. When computing induced velocities in the panel code, only the dipole contributions are taken into account (as suggested by Starke and Bosschers 2012 and as described above).

3.3.1 Body Force Transfer in Overlapping Grids

XCHAP offers so-called "active" and "passive" modes for propeller grids. If the propeller grid is "passive" it is merely used for convenience and all forces are always interpolated from the propeller grid to the background grid (all propeller grid cells are interpolation cells by definition). An "active" propeller grid is treated like any other grid, meaning that it actually contains discretization cells if it is resolving the point in question better than any other grid in the region. Generally, both approaches are viable options, one should note,

* See, for example, the previously mentioned *Workshops on CFD in Ship Hydrodynamics*.

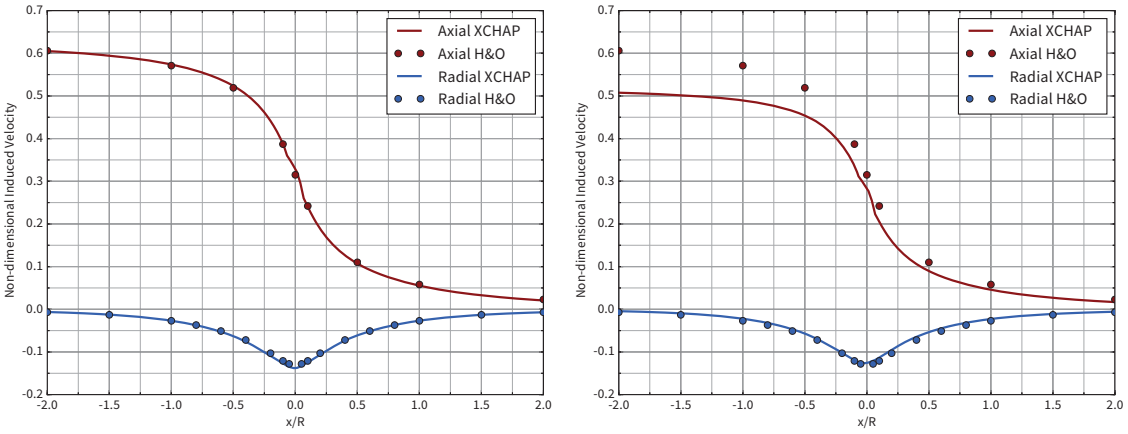

(a) $C_{TH} = 0.2$ **(b)** $C_{TH} = 1.0$

Figure 3.2: Induced Velocities on r/R=0.7: Actuator Disk RANS and Analytical Results from Hough and Ordway (1964)

however, that the interpolation of body forces from the "passive" propeller grid to other grids is out of reach for the user and not always conservative – meaning that thrust or torque might be lost in the additional interpolation step, depending on the exact grid composition and overlap. "Active" grids, on the other hand, give more control to the user and will usually not suffer from any possible further interpolation issues, but do require special attention and a well-designed overlap, as the grid will actually influence the flow resolution.

In any case, utmost care is required when creating the grids in the aftbody and propeller region. This requirement is still very reasonable, given that it is the only major pitfall and replaces much more involved algorithms required to find the correct cells for mapping forces to distributed, unstructured grids.

To evaluate the impact of different choices for propeller grids, and to check the general applicability of the particular RANS method, a simple test case can be set up. By implementing a method that generates a force field representing an actuator disk, the induced velocities can be validated against the classic results by Hough and Ordway (1964). The corresponding force field is applied to a cylindrical propeller grid that is embedded in a cubic box, resulting in a setup comparable to an open water test.

When the condition of carefully created grids is fulfilled, excellent agreement of induced velocities is achieved for cases with a low thrust loading (see Fig. 3.2a). When the propeller loading is increased, larger deviations behind the propeller can be seen (Fig. 3.2b). This, however, is perfectly in line with the expectations, as it only shows the limitations of linear actuator disk theory. Nonlinear actuator disk theory yields lower induced axial velocities at the

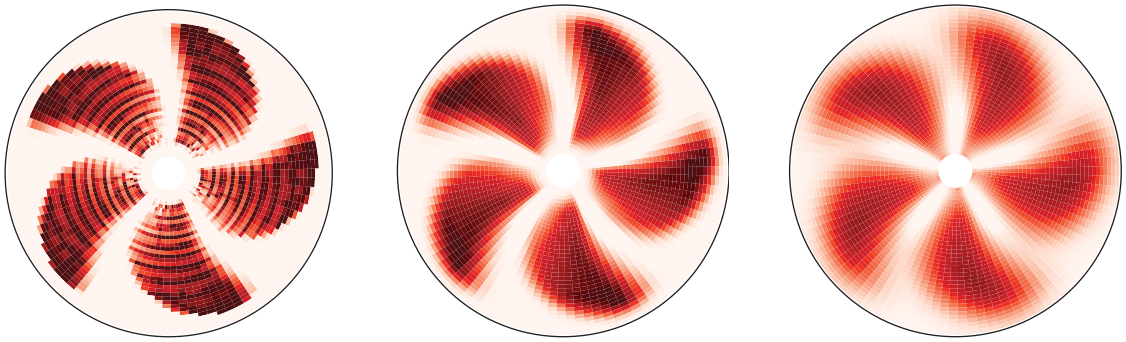

(a) No Smoothing **(b)** One Sweep **(c)** Five Sweeps

Figure 3.3: Blade Forces and Smoothing after Interpolation to the RANS Grid (Integrated along the Axial Grid Dimension)

given radius in the slipstream (cf. Breslin and Andersen 1994, p. 190), similar to the RANS results in Fig. 3.2b. Note that the induced velocities in Fig. 3.2 (and all similar figures) are normalized by the ship speed and divided by C_{TH}.

Fig. 3.3 shows an example of the axial force field corresponding to one BEM timestep mapped to a cylindrical RANS grid. For visualization purposes, the third grid dimension is collapsed into one slice and the sum along the axial dimension of the grid is shown. The panel forces from each blade angle ("timestep") of the unsteady BEM solution are being transferred to the cylindrical grid by trilinear interpolation. For a steady-state RANS solver like XCHAP, the force field is then time-averaged.

As in overlapping grids the resolution of the RANS propeller grid should not be too different from typical cell sizes in the background grid (usually the grid around the hull), it is often inevitable to have RANS grids and BEM meshes with very different radial resolutions. Simple trilinear interpolation of the panel forces to the cylindrical RANS grid will then lead to artifacts as can be seen in Fig. 3.3a. In such cases, smoothing is helpful and sometimes strictly necessary, as very pronounced force peaks resulting from such interpolation artifacts can render the solution unstable.

To still retain the characteristics of the force distribution, smoothing is applied separately and sequentially in the three grid dimensions. In the present implementation, one "sweep" consists of two smoothing iterations applied in radial direction, followed by one iteration in circumferential and axial direction each. This default has proven to work well for common ratios of mesh resolutions, but can be increased for more extreme cases. Excessive smoothing, however, will lead to new artifacts as forces diffuse, leaving the actual radial range of the propeller (as can be seen in Fig. 3.3c).

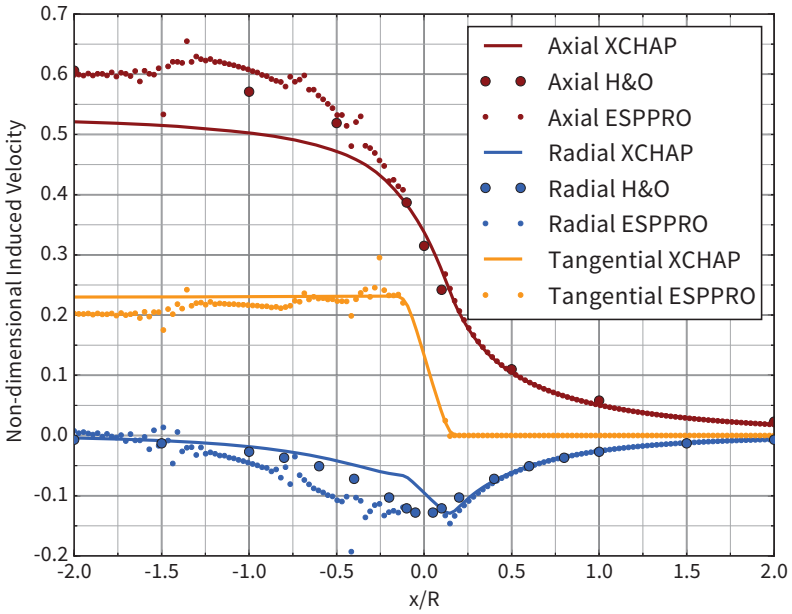

Figure 3.4: Induced Velocities on r/R=0.7: Conventional Propeller RANS-BEM Coupling, BEM, Actuator Disk

3.3.2 Basic Validation in Open Water

A simple, yet essential step in implementing the RANS-BEM coupling method is to check whether the induced velocities computed by the BEM match the velocities induced by the body forces in the RANS solver. This can be done by running the coupling for an open water case, as that is the only case where the effective velocity distribution is known exactly – there is no hull-propeller interaction and the effective wake is equal to the nominal wake, to use those terms. In an infinite domain with parallel inflow of unity magnitude and a working "BEM-coupled" propeller, the total velocity extracted at any position in the RANS minus the BEM-computed induced velocity should yield unity parallel inflow again.

For the RANS-BEM coupling to work properly and accurately in practice, it is however sufficient if the induced velocities "cancel out" in the coupling plane where the effective wake is computed and that is used to exchange velocities.

Running the coupled programs for such open water case with a conventional propeller results in a induced velocity distribution shown in Fig. 3.4. The figure again shows induced velocities along a line parallel to the propeller shaft on 70% of the propeller radius, just as Fig. 3.2. The linear actuator disk values are also again plotted for reference. The agreement of the RANS and BEM velocities upstream of the propeller seems very good, downstream large discrepancies arise. Upstream, even the linear actuator disk results match rather nicely. There

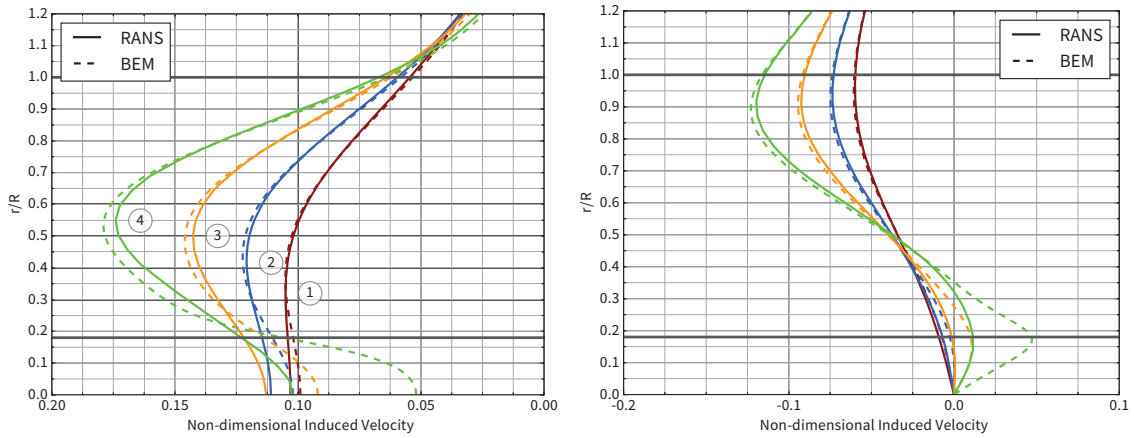

(a) Axial **(b)** Radial

Figure 3.5: Upstream Induced Velocity Profiles in RANS and BEM (KCS Propeller *KP505*, $J = 0.7483$)

are several explanations for the discrepancies downstream. First, the "outliers" of the BEM velocity profile are a result of those individual points being located too close to the singularities of either blade or wake panels. Second, one needs to remember that the induced velocities are computed without the source contributions. Adding those contributions as well, the BEM provides a radial velocity profile that is symmetric around the propeller plane and yields very good agreement with the actuator disk results.

As mentioned above, it is only the agreement in an upstream coupling plane that is crucial for typical applications of the RANS-BEM coupling approach. In order to investigate this more closely, axial and radial induced velocity profiles (see Fig. 3.5) are generated in four potential planar coupling planes upstream, located at $x/R = 0.3$ (marked ④ in the figure), 0.4/③, 0.5/②, and 0.6/①. The propeller, advance ratio and plane locations are identical to the example used by Hally (2015). The agreement found here can be considered equally good as demonstrated in that paper*. The increasing discrepancies towards the blade root can probably be attributed to the lack of the hub in the computation (causing unrealistic peaks in the BEM velocities, the radial component in particular), the increasing blade thickness, and the fact that the distance from the evaluation plane to the blade's leading edge decreases for decreasing radial positions. The agreement at the outer radii is very good and indicates that the interface between the programs works properly and that the implementation is ready for use in the behind-ship condition.

* One should note, however, that Fig. 3.5 shows induced velocities divided by C_{TH}, whereas Hally (2015) plots absolute total velocities.

3.3.3 Coupling Plane Considerations

As described in the literature (see review in Section 3.2, p. 47), the selection of the coupling plane type and location has a profound impact on the computation of effective wake fractions and therefore self-propulsion results. It is obvious from Fig. 3.4 and Fig. 3.5 (and also basic theory), that the magnitude of the induced velocities decreases quickly as one moves further upstream, away from the propeller. But also the relative and absolute discrepancies between the induced velocities in RANS and BEM decrease at larger distances (see Fig. 3.5), as the inherent modeling differences between the two methods become less significant in the far field.

Placing the coupling plane close to the propeller can therefore be considered an "aggressive" choice. On one hand, one will avoid an excessive overprediction of the effective wake fraction. On the other hand, it needs to be ensured that the profiles of the induced velocities in the coupling plane match, which will be more difficult to achieve close to the blade.

The present implementation includes options for all major coupling plane approaches described in the literature.

The simplest form is a single, planar coupling surface upstream of the propeller. This approach is trivial to implement and very robust as long as the plane is sufficiently far away from the foremost point of the blade.

Even though a curved coupling surface that follows the contour of the blade's leading edge is not much more complex to implement than its planar counterpart, this extension can lead to substantial improvements. By following the leading edge at a constant distance, the discrepancy between RANS and BEM velocities might be considered more consistent, as the shortest distance from a point on the coupling surface to the blade is always the same. While discrepancies may still exist and appear as artificial contributions to the effective wake fraction, the velocity distribution in the effective wake field might at least be less distorted. Especially for propellers with considerable rake and little hull clearance*, choosing a curved coupling plane over a planar one can make a big difference.

Based on multiple planar or curved upstream coupling surfaces, linear extrapolations to the propeller plane have been reported to yield good results. This has also been implemented in the present method. As a variation and extension of the extrapolation to the propeller plane, the axial effective velocity gradient can be passed to the propeller code in addition to the effective wake field in an upstream plane. Computing this gradient from multiple upstream coupling planes, one can then vary the onset velocity on the blade panels

* Such as the *Japan Bulk Carrier*, see Hino et al. (2016) and the proceedings of the Tokyo 2015 workshop (not published yet).

depending on their individual axial position.

Still, as extrapolations always carry an inherent risk of compromising robustness, the default behavior of the present implementation is to use a single, curved upstream coupling plane. The present implementation in this default configuration has already been successfully applied in a different study to verify results from a vortex lattice-based propeller and pre-swirl stator optimization by RANS-BEM coupling-driven self-propulsion simulations (Saettone, Regener, and Andersen 2016).

Experiments regarding other novel coupling plane approaches – for example including additionally computed effective velocities at small distances downstream of the blade to then interpolate to the propeller plane – were not pursued further. Robustness and reliability were not satisfactory, while the potential gain in accuracy was also found to be small.

3.3.4 Computational Performance and Related Practical Issues

Section 2.3.5 already described performance aspects of the BEM implementation alone. As the lower computational effort compared to all-CFD approaches is a major advantage and argument for using RANS-BEM coupling, computational performance and scalability also need to be considered when running the two parts of the simulation in a coupled manner.

As we have already entered the age of parallel computing, almost everything runs in parallel. Today's CFD solvers usually scale very well and are parallelized using MPI* allowing for massive parallelization using dozens or hundreds of processors spanning over multiple computing nodes. Potential flow-based propeller codes, on the other hand, are probably either not able to run in parallel at all, or parallelized for shared memory architectures (such as ESPPRO, using OpenMP, see p. 35).

This raises the question of how to run the coupled simulation practically, as the RANS part is able (and likely) to run on many processes across arbitrarily allocated resources within a computing cluster without a shared memory address space. Many RANS processes might have to wait idle for the propeller model to finish updating the forces. As in the described scenario the propeller code only utilizes one computing node at best, it can not harness the total computing power of all nodes involved in the RANS simulation.

The implementation of the University of Iowa (IIHR, Group of Prof. Stern, Chase et al. 2013, Martin et al. 2015a) therefore continuously runs the propeller

* Message Passing Interface, allows for parallel execution also across physical machines. MPI is standardized, yet multiple implementations of the standard exist. The initial draft for the standard, including motivation and introduction is described by MPI Forum (1993), but newer versions of the standard exist.

code in a separate process and simply takes the then-latest propeller forces when needed. This is a viable option if the propeller model is not parallelized at all and/or requires significant walltime to run.

The present implementation does not require setting apart resources for a continuous propeller process, but rather ensures that the BEM only runs briefly and at maximum speed while all processes of the RANS solver wait for the new propeller forces. Then one coupling iteration including effective wake calculation, running the unsteady analysis in ESPPRO, and feeding back new RANS body forces takes much less than one minute. Given that usually less than ten of such coupling iterations are needed, the overall walltime overhead of this process is small.

Running the BEM at maximum speed requires utilizing all available CPU cores on one node when updating the propeller forces. This still raises some issues, as most modern MPI implementations "bind" the processes to certain physical cores, sockets, or even memory by default, as substantial performance gains can be achieved if a processor core and a nearby contiguous piece of memory are exclusively available to one specific thread. Programs parallelized by OpenMP can also benefit from similar affinity settings.

Problems therefore arise as soon as different programs (such as the RANS solver and the propeller code) are running on the same node, as the two programs "fight" for resources, trying to bind to processors exclusively, and as a result the propeller code might easily get slowed down by a factor of 10–100, compared to the usual execution time on the same hardware.

The specifics depend on the operating system and the MPI implementation, but one needs to either temporarily unbind the MPI processes, or to make sure the MPI processes are not spinning ("busy-waiting"), blocking their allocated resources without doing useful work.

In the present implementation the RANS processes are explicitly set to "sleep" while the propeller forces are updated and the BEM is running. On Linux systems, it is then sufficient to additionally reset the processor affinity of the newly spawned BEM process using the `taskset` command, as the BEM would otherwise be limited by the inherited resource allocation of the one(!) MPI process that launches the propeller model.

Many of these details are highly implementation-specific and might even depend on the specific hardware or operating system used to run the simulation. Still, one needs to be aware of these issues on a conceptual level first, as large differences in scalability of the RANS and the BEM part of the hybrid simulation may pose surprisingly severe limits on the overall computational efficiency and required walltime.

4 Application to Conventional and Kappel Propellers

This chapter describes two related, yet separate applications of the methods developed as part of the present work and described in Chapters 2 and 3.

The first part, Section 4.1 (p. 61ff.), documents the application of the RANS-BEM coupling approach to simulate self-propulsion tests with both a Kappel propeller and a comparable conventional propeller. These simulations were carried out to determine and assess the hull-propeller interaction and to investigate possible differences in global flow characteristics that could explain the effective wake behaviour of Kappel propellers observed in experiments, as mentioned in Section 1.2.

The second part, Section 4.2 (p. 82ff.), then draws from the results from the self-propulsion simulations to evaluate the behind-hull cavitation performance, focusing on the influence of the inflow field used. This is also motivated by the slightly more intricate cavitation characteristics of Kappel propellers, very briefly outlined in Section 1.2, which are suspected to be related to the interaction with the hull wake field.

Results are given for a modern handysize bulk carrier with high block coefficient ($c_B = 0.81$ and a rather full aftbody, with a tendency towards flow separation at model scale). Two propellers have been designed for this ship as part of the present work. Both designs are based on the same thrust requirement and the model scale nominal wake distribution. This represents the typical upfront knowledge of the propeller designer (see Sections 1.1 and 3.1.2). For the propeller design, the axial component of the nominal wake field was uniformly scaled to match the expected effective wake fractions, taking the different expectations for a conventional and a Kappel design into account.

The blade geometries used here are unrefined designs based on simple design tools (based on the method by Andersen and Andersen 1987) and do not even try to represent the state of the art in propeller design and optimization. Neither for the conventional nor for the Kappel design. Rather, two simple geometries were established with the intent to show the main geometry features and distinctions between conventional and Kappel propellers to identify possible general trends and differences in a simulation.

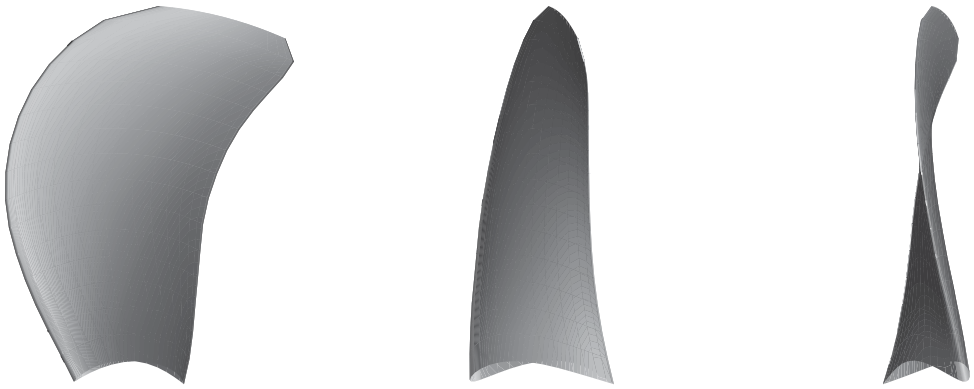

(a) Looking Aft **(b)** Side View **(c)** Looking at LE

Figure 4.1: Conventional Blade Geometry

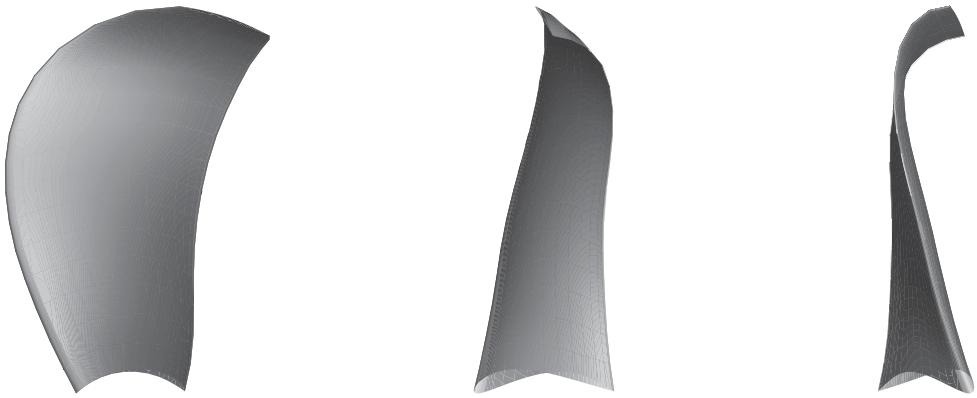

(a) Looking Aft **(b)** Side View **(c)** Looking at LE

Figure 4.2: Kappel Blade Geometry

The blade geometries of the conventional and the Kappel-type propeller are shown in Fig. 4.1 and Fig. 4.2, respectively. The main characteristics are listed in Tab. 4.1. All radial input distributions to the design tool were kept as similar as possible for the two propellers, the differences in resulting pitch distributions are mainly a result of the different assumptions for the effective wake fraction, as mentioned above, aiming at identical propeller speeds in self-propulsion. The chord distributions were modified to result in identical expanded blade area ratios. At same area ratio, the sectional chord lengths are shorter for the Kappel propeller due to the longer effective span.

		Kappel	Conv.
Number of Blades	z	3	3
Diameter	D	Identical	
Thrust Loading at Design Point	C_{TH}	1.40	
Hub Radius	r_h/R	0.150	0.150
Blade Area Ratio	A_E/A_0	0.388	0.388
Design Advance Ratio	J	0.590	0.613
Pitch Ratio (at $r/R = 0.7$)	$P/D_{0.7}$	0.926	0.949
Effective Skew Angle	$\theta\,[^\circ]$	19.2	18.6
Profile Type		NACA66 (mod.)	

Table 4.1: Propeller Particulars

4.1 Self-Propulsion and Effective Wake

The brief introduction to Kappel propellers (Section 1.2, p. 9) mentioned that previous experimental studies consistently revealed increased effective wake fractions for ships equipped with a Kappel propeller. This increase is usually found to be between 5–10%, compared to the same ship with a conventional propeller, and has been observed and confirmed in numerous experiments since the introduction of the Kappel propeller concept, including various ship types, aftbody forms, and propeller loadings. Unfortunately, the experimental approach only provides the effective wake fraction (using the thrust identity approach) and does not allow for any further insight into the wake distribution, as the effective wake is a purely conceptual flow field (see Section 3.1.2).

The simulation results presented in the following are based on the RANS-BEM implementation introduced in Chapter 3, which is used for numerical self-propulsion simulations at model and full scale, thereby inherently and explicitly computing effective wake fields and fractions.

In those simulations a single coupling plane is used that follows the propeller's leading edge contour at an axial distance of 1.5% of the propeller diameter. For visualization of wake fields, the velocities extracted on these moderately curved surfaces are projected onto a planar surface. All results and velocity fields shown are steady-state in calm water and at the converged self-propulsion point.

Experimental results for validation are not available for the propeller geometries used here. Model tests with a stock propeller and a different Kappel propeller, however, agree well with the simulation results for hull-propeller

interaction coefficients shown in the following.

If the effective wake fraction is considerably higher for a Kappel propeller, there must be some global effect leading to such difference in effective flow. This is particularly true, if the guess expressed by Andersen et al. (2005b) holds, that the radial velocity components of the effective wake field also differ from effective wake fields for conventional propellers, amplifying the different behind-hull cavitation behavior.

In a try to shed some more light on this and to get some more insight into the total and effective flow upstream of the propeller, the effective velocities are not only evaluated in the wake plane used for the RANS-BEM coupling, but also in a number of points in the centerplane of the ship. This allows for visualizing the effective flow in a slice perpendicular to the propeller plane, which adds another dimension of information to the wake field, and might help illustrate and understand effective flow differences on a more global level.

Computational Setup

The general computational setup for model and full scale computations is identical, apart from obviously necessary differences, such as grid stretching and the presence of a towing force in model scale self-propulsion.

Beyond the default behaviour of SHIPFLOW-XCHAP, the "global approach" is used (i.e. the entire ship is part of the RANS domain). The fine and body-fitted grid around the hull is further refined in the aftbody region to ensure good flow resolution and good feedback between the hull and propeller grids. The inlet plane is located 80% of the ship length upstream of the forward perpendicular, the outlet is placed one ship length downstream the aft perpendicular. The computational grids are stretched towards the ship hull according to the Reynolds number, aiming at a y^+ value of 0.7. The propeller grid is of "active" type (see Section 3.3.1), and turbulence closure is based on the Explicit Algebraic Stress Model (EASM)*.

Dynamic trim and sinkage are taken from a model scale self-propulsion experiment with the same hull, and the free surface is not included in the simulation (double body approach), as the Froude number of the simulated condition is low (0.14). The rudder or other appendages are not included in the simulation.

The total number of cells in the RANS domain is about 13 million for the model scale case and about 18 million for the full scale case. All RANS simulations are run until convergence, which is defined as a change in the total longitudinal force smaller than 0.25%, plus a standard deviation of the pressure

* Also see the XCHAP theory manual: Flowtech (2007)

contribution to that force below 0.025%. Both criteria are considered over the previous 10 iterations*. The propeller forces are updated every 10 iterations, and the propeller shaft speed is changed for each new coupling iteration to balance the forces in self-propulsion mode. The entire process converges after about 10 such coupling iterations. Due to the computational efficiency related to the use of structured grids in RANS and parallelization of the BEM code, the entire self-propulsion simulation only takes in the order of 100 CPU hours (usually 3–5 hours of walltime using 40 CPUs on a cluster).

On the BEM side, the propeller blades are discretized into 16 panels in spanwise direction and 32 panels in chordwise direction (16 panels each per pressure and suction side). In chordwise direction, cosine stretching is applied towards the leading and trailing edges. This rather coarse mesh is due to the legacy design method that was used for the design of these propellers, which also provides the meshes directly.

The timestep in the unsteady BEM calculations corresponds to a 5° blade angle increment. Forces and velocities for the RANS coupling are only written out after two full blade revolutions of BEM simulation time to build up the blade wake strength.

* Also see the SHIPFLOW documentation: Flowtech (2016)

Quantity		Hoshino		Streckwall	
		Kappel	**Conv.**	**Kappel**	**Conv.**
Effective Wake Fraction	w	0.289	0.273	0.320	0.304
Thrust Deduction	t	0.146	0.146	0.146	0.146
Relative Rotative Efficiency	η_R	1.020	1.022	1.020	1.021

Table 4.2: Hull-Propeller Interaction Coefficients, Model Scale

4.1.1 Model Scale Simulation Results and Analysis

Running resistance and self-propulsion simulations at model scale using RANS-BEM coupling in the setup described before, the hull-propeller interaction coefficients shown in Tab. 4.2 are found. Generally, the results appear to be in line with the expectations from model tests:

The effective wake fraction is about 5% higher for the Kappel propeller, while the thrust deduction remains unchanged. This corresponds very closely to typical experimental results. The differences in relative rotative efficiency are too small to allow any inferences to be made. Previous studies (e.g. Andersen et al. 2005b) reported less favorable values for η_R for Kappel propellers.

Given the very primitive way of estimating viscous forces acting on the propeller in the BEM (using the computed surface velocities and a constant friction coefficient) and the resulting lack of confidence in details of the torque prediction, the relative rotative efficiency is not studied in further detail here.

The prediction of the thrust deduction, especially with regard to comparison of conventional and Kappel propellers, does not appear critical either, as the simulation results are in line with experiments and do not show any noticeable differences among the propellers. In the following, focus is therefore placed on the effective wake.

Table 4.2 already indicates that the self-propulsion simulations for both propellers were carried out twice, using different blade wake models in the propeller code (also see p. 29). The obvious differences in effective wake fraction between the simulations with different wake models already give a hint of the importance and impact of the geometry of the blade wake in the BEM. The differences in blade wake geometry that ultimately cause the different results are very obvious:

A longitudinal cut on the centerline for the simple blade wake (helicoidal surfaces without slipstream contraction, using the wake pitch assumptions by Streckwall 1998) is shown in Fig. 4.3. Hoshino's wake model (Hoshino 1989) generates the geometry from Fig. 4.4 for the same propeller and advance ratio.

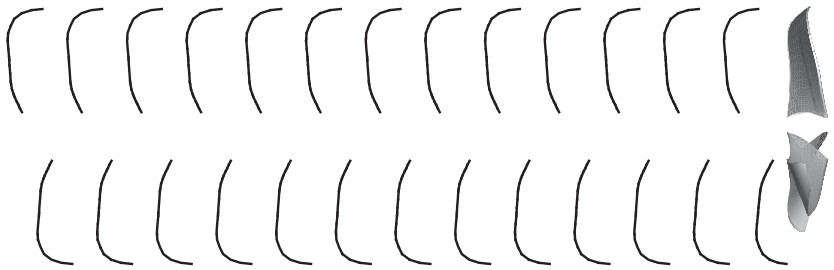

Figure 4.3: Longitudinal Section of Simple Blade Wake

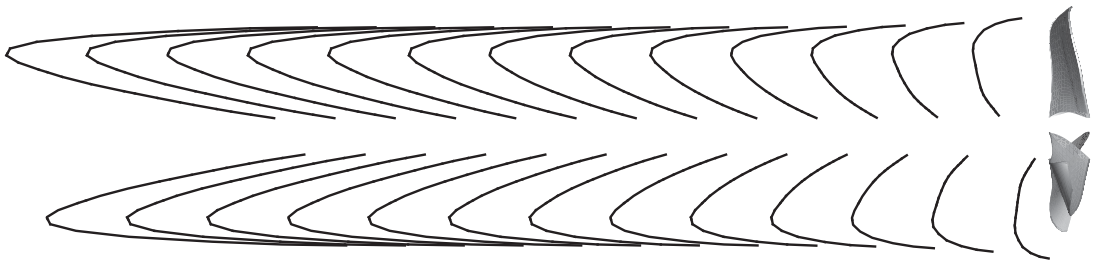

Figure 4.4: Longitudinal Section of Hoshino-type Blade Wake

Verifying the Induced Velocities

As described in Chapter 3 (see p. 54f. in particular), it is essential that the induced velocities on both sides of the RANS-BEM coupling match. The open water scenario is the only case where the induced velocities in the RANS part are known, therefore this is the only situation that allows for checking the agreement of induced velocities in the coupling plane (as described above, a curved plane 1.5%D upstream of the leading edge in this case). This is done for both propellers at the final apparent advance ratio from the corresponding self-propulsion simulation. The velocities in the following plots are nondimensionalized using the undisturbed inflow velocity and divided by the thrust coefficient.

The (axisymmetric) result using Hoshino's wake model is shown in Fig. 4.8 for the conventional propellers and in Fig. 4.9 for the Kappel propeller. Major discrepancies appear for both propellers in this case.

The results of the same exercise using Streckwall's wake model can be seen in Fig. 4.10 for the conventional propeller and in Fig. 4.11 for the Kappel propeller. From these four figures, several observations can be made:

The induced velocities in RANS (resulting from the BEM-computed force field) are almost identical for the two wake models.

The induced velocities computed in the BEM, however, differ significantly. For both wake models, the BEM-computed induced velocities are relatively

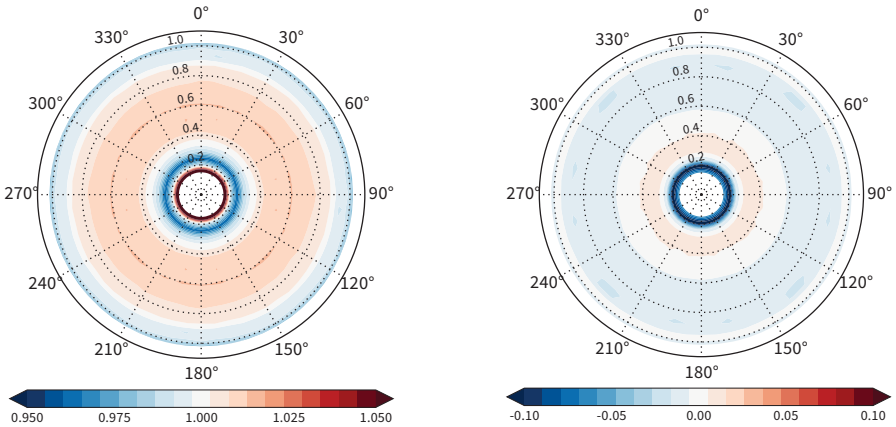

(a) Axial Component **(b)** Radial Component

Figure 4.5: RANS/BEM Induced Velocity Discrepancy – Conventional Coupling Corrections ("Effective Wake" in Open Water)

higher for the Kappel propeller, which will result in a higher effective wake fraction, just by virtue of a lack of agreement of induced velocities between the two methods involved in the coupling process.

The shapes of the velocity profiles are generally in fair agreement. In most cases, the induced velocities computed in the BEM lack in strength. For the propellers used in the present case, Streckwall's wake model leads to considerably better agreement of induced velocities than Hoshino's model.

For the Kappel propeller, significant differences between the wake models exist regarding the computed induced axial velocity close to the tip. Using Hoshino's model, the induced axial velocity hits zero at the tip radius, whereas Streckwall's model predicts a sizeable value in the tip region, even outside the propeller disk.

The lack of the propeller hub in the BEM leads to an unrealistic flow around the open root of the blade, resulting in the peaks close to the hub radius seen in all plots (Fig. 4.8 through 4.11), particularly affecting the radial velocity component.

The results for the simple blade wake model (Fig. 4.10 and 4.11) are visualized in a different form in Fig. 4.5 and 4.6, showing "effective wake fields" in open water. Those figures illustrate the areas where the velocities in the effective wake field prediction from the self-propulsion might be questionable, based on the results in open water.

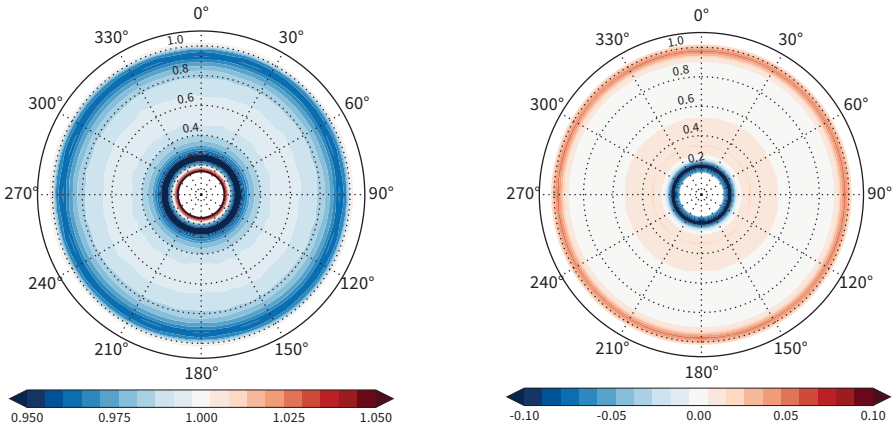

(a) Axial Component **(b)** Radial Component

Figure 4.6: RANS/BEM Induced Velocity Discrepancy – Kappel Coupling Corrections ("Effective Wake" in Open Water)

Effective Wake Fields

All wake and velocity fields shown in the following are the ones obtained with Streckwall's simple blade wake model (described in Section 2.3.1).

The wake fields shown in Fig. 4.12 and Fig. 4.13 are "raw" data, i.e. they show the fields from the final coupling iteration of the self-propulsion simulation without any possible modifications discussed in the next section.

Starting by looking at the induced velocity fields at the self-propulsion point on p. 73, two main differences between the conventional and the Kappel propeller can be seen: First, the axial velocities induced by the Kappel propeller are distributed more homogeneously in radial direction and the peak value is obviously shifted outwards. Second, the radial components of the induced velocities at the outer radii are visibly stronger for the Kappel propeller. There are no induced velocities in tangential direction, as the coupling plane is placed upstream of the propeller.

Looking at the effective wake fields on p. 72, no major differences in the flow field can be seen. The isolines of axial velocities are similarly shaped, and just offset by what corresponds to the difference in effective wake fraction.

Also, the in-plane velocity components are very similar, except the clearly stronger radial flow close to the tip, seen in the effective wake field for the Kappel propeller (Fig. 4.12).

Looking back at the discrepancies of induced velocities seen in the open water coupling (Fig. 4.5 and 4.6), it seems possible that they cause at least parts of the observed differences in effective wake fraction and distribution between the two propellers.

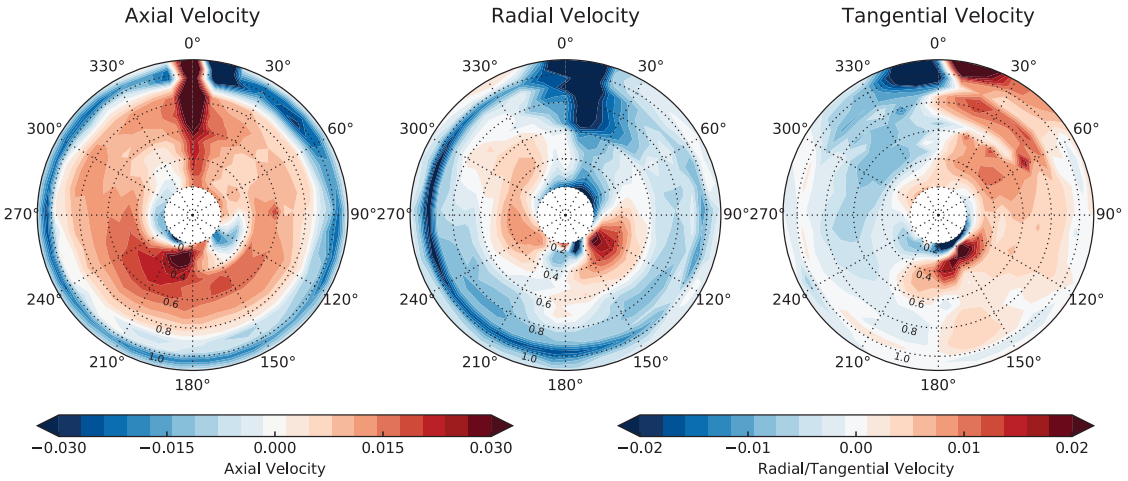

Figure 4.7: Difference of Corrected Self-Propulsion Effective Wake Fields from Conventional and Kappel Propeller

Correcting Effective Wake Fields based on Open Water Discrepancies

When assuming that the discrepancies found in open water apply identically to the behind ship-condition, one can add them as "coupling corrections" to the fields obtained in the self-propulsion simulation. The coupling correction then inherently includes inaccuracies in the calculation of induced velocities within the scope of the theory, as well as general differences that result from the different governing equations of potential flow and RANS. This way of compensating for the known discrepancies in open water is similar to the method described by Sánchez-Caja et al. (2015).

Applying these coupling corrections, the increased magnitude of the effective radial velocity and the increased effective wake fraction for the Kappel propeller disappear. By adding the field from Fig. 4.6 to the effective wake field from self-propulsion (Fig. 4.12) one may find a corrected effective wake field for the Kappel propeller case. Then subtracting the sum of Fig. 4.13 and Fig. 4.5 (the corrected effective wake field for the conventional propeller) from it, one finds Fig. 4.7, showing the differences of the two corrected effective wake fields. Note that the color scale in that figure is very narrow and zero-centered. White areas indicate zero difference between the effective wake field from the Kappel propeller and the conventional propeller. Positive values indicate higher velocities in the Kappel velocity field. Plotting the difference of two similar fields using a narrow color scale and the hull's tendency to cause flow separation in the aftbody region let the figure appear rather messy, but the main message is clear: Employing the described models and the coupled approach to simulating the working propeller behind the ship in numerical self-propulsion does neither result in significantly different effective wake frac-

tions nor systematically different effective wake distributions after applying the coupling correction fields found from an open water case.

The very small difference of the corrected effective wake fields suggests that the increased effective wake fraction for the Kappel propeller initially found from the RANS-BEM simulation – which corresponded nicely to the experimental results – was a fluke. Further interpretations and implications of this are discussed in Chapter 5.

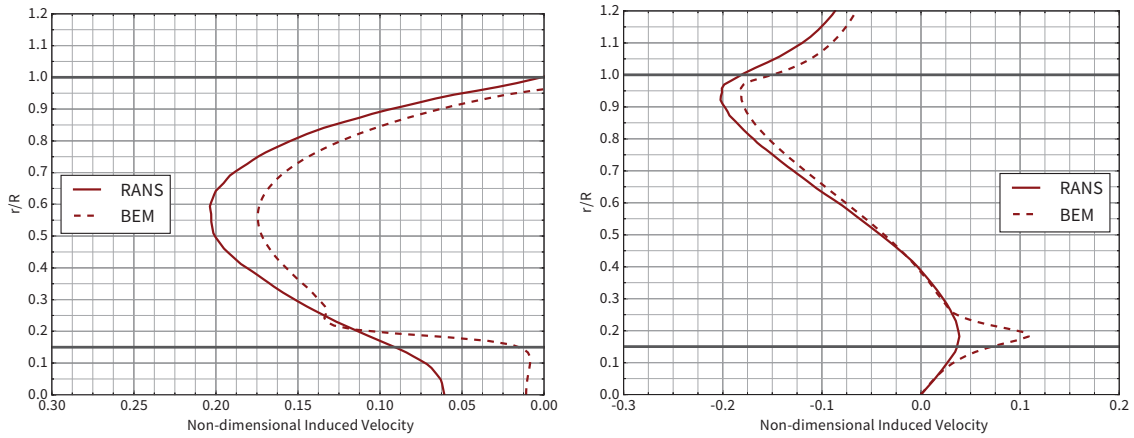

(a) Axial Component **(b)** Radial Component

Figure 4.8: Induced Velocities in Open Water, RANS/BEM – Conventional Hoshino Blade Wake

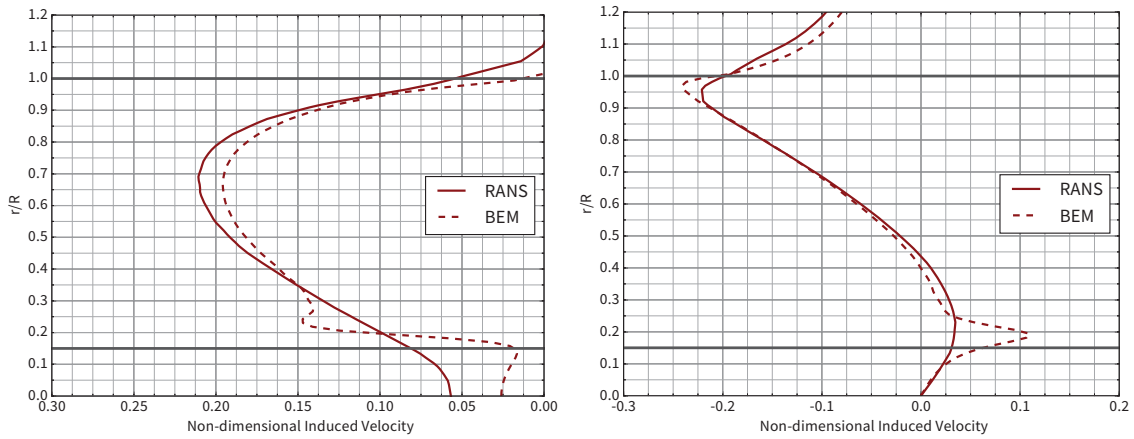

(a) Axial Component **(b)** Radial Component

Figure 4.9: Induced Velocities in Open Water, RANS/BEM – Kappel Hoshino Blade Wake

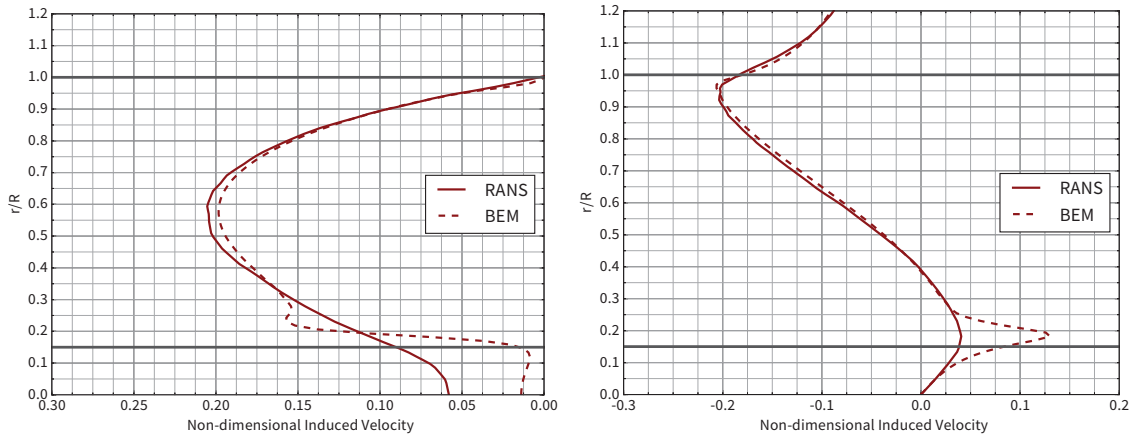

(a) Axial Component **(b)** Radial Component

Figure 4.10: Induced Velocities in Open Water, RANS/BEM – Conventional Streckwall Blade Wake

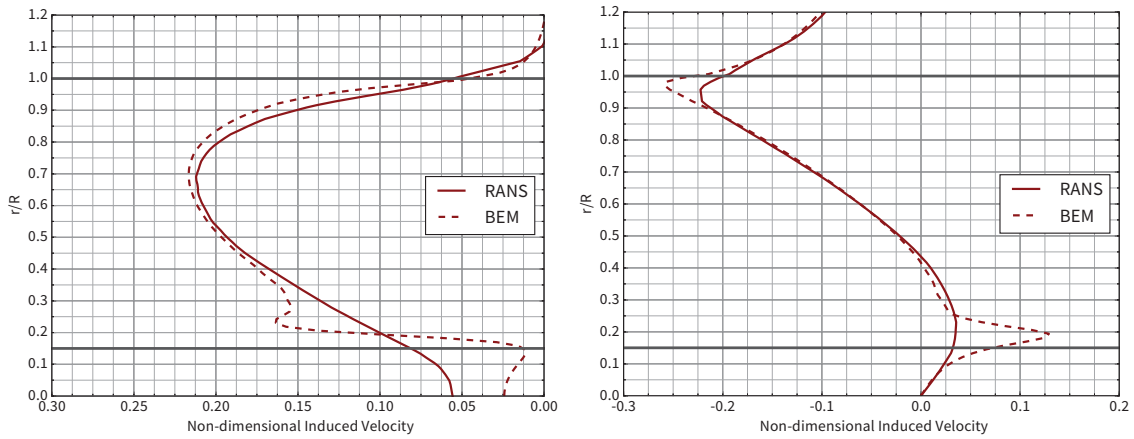

(a) Axial Component **(b)** Radial Component

Figure 4.11: Induced Velocities in Open Water, RANS/BEM – Kappel Streckwall Blade Wake

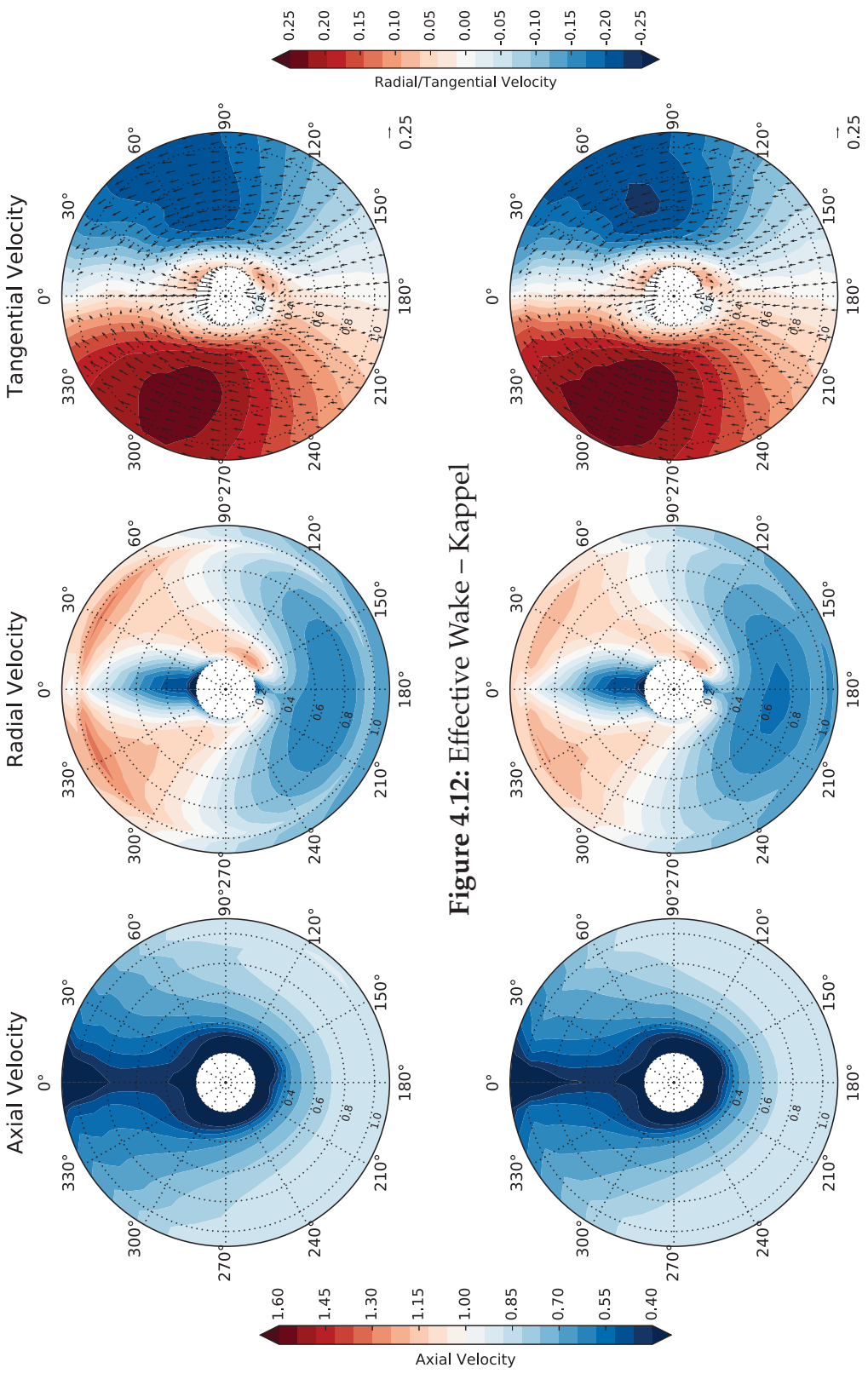

Figure 4.12: Effective Wake – Kappel

Figure 4.13: Effective Wake – Conventional

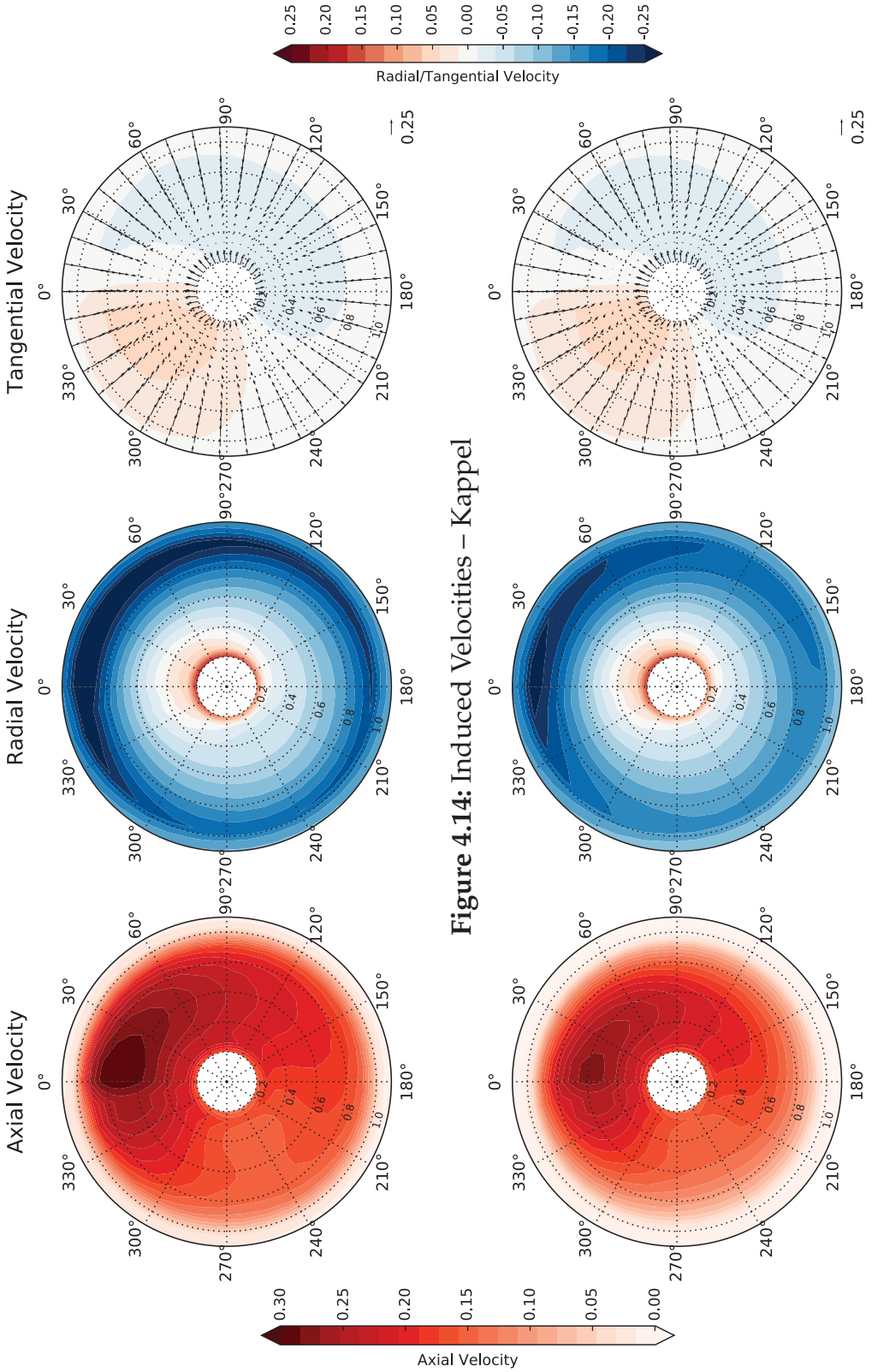

Figure 4.14: Induced Velocities – Kappel

Figure 4.15: Induced Velocities – Conventional

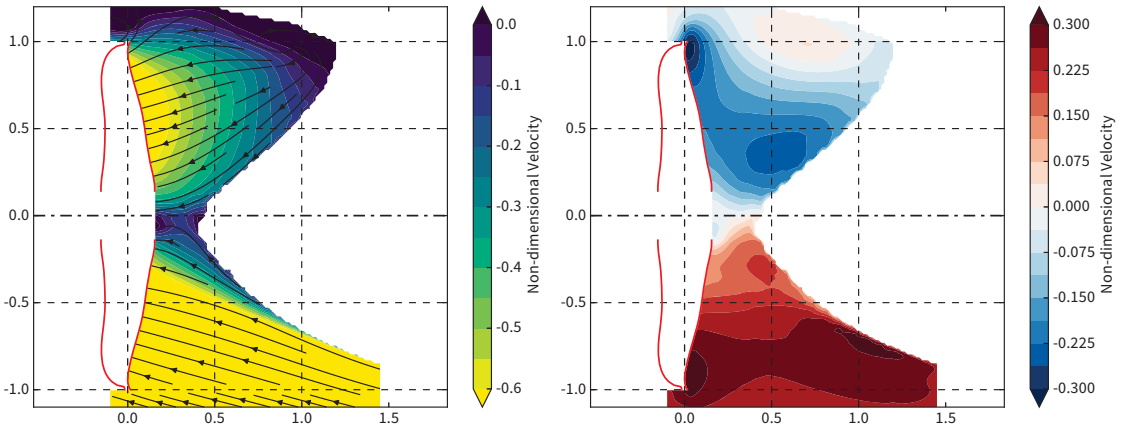

(a) Axial Component **(b)** Vertical Component

Figure 4.16: Total Velocities in the Center Plane – Kappel

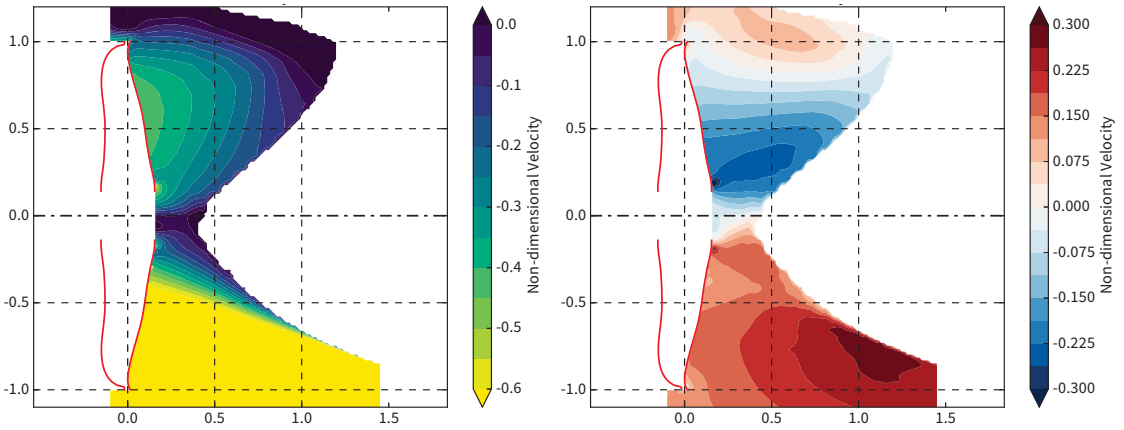

(a) Axial Component **(b)** Vertical Component

Figure 4.17: Effective Velocities in the Center Plane – Kappel

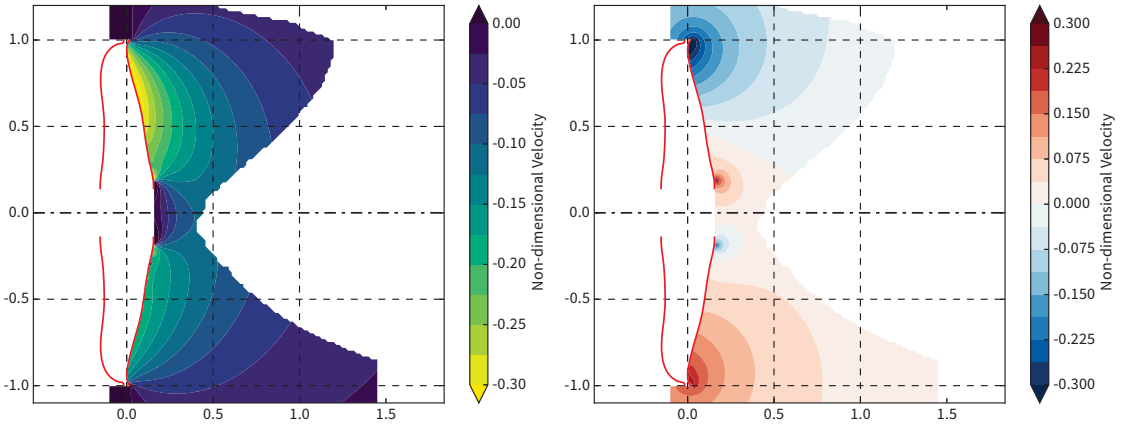

(a) Axial Component **(b)** Vertical Component

Figure 4.18: Induced Velocities in the Center Plane – Kappel

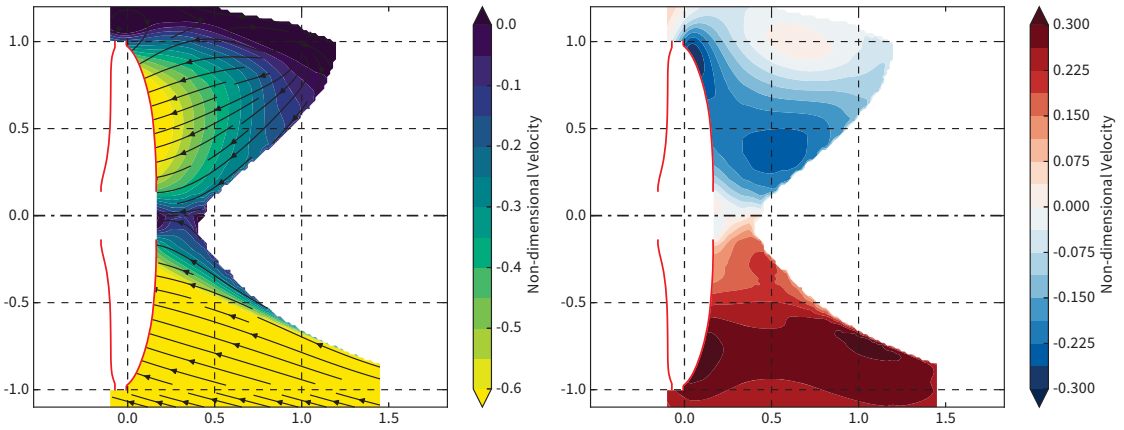

(a) Axial Component **(b)** Vertical Component

Figure 4.19: Total Velocities in the Center Plane – Conventional

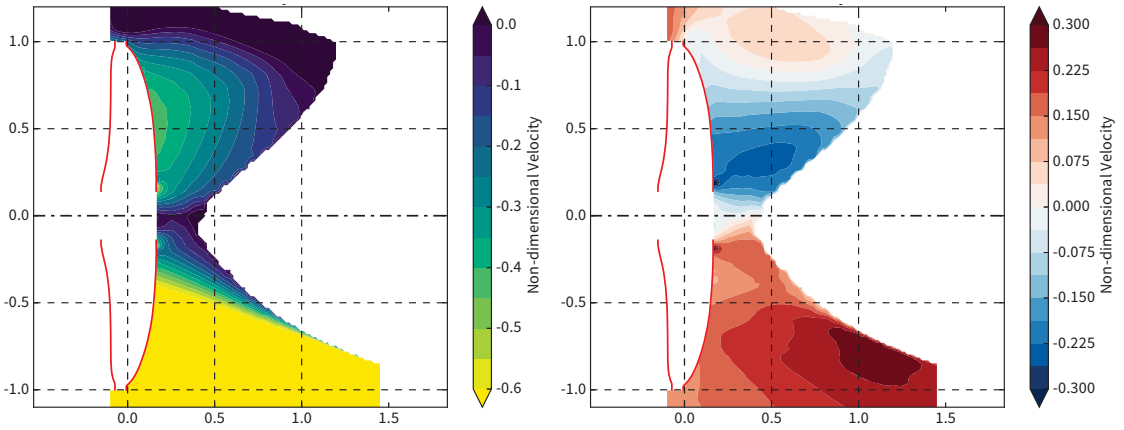

(a) Axial Component **(b)** Vertical Component

Figure 4.20: Effective Velocities in the Center Plane – Conventional

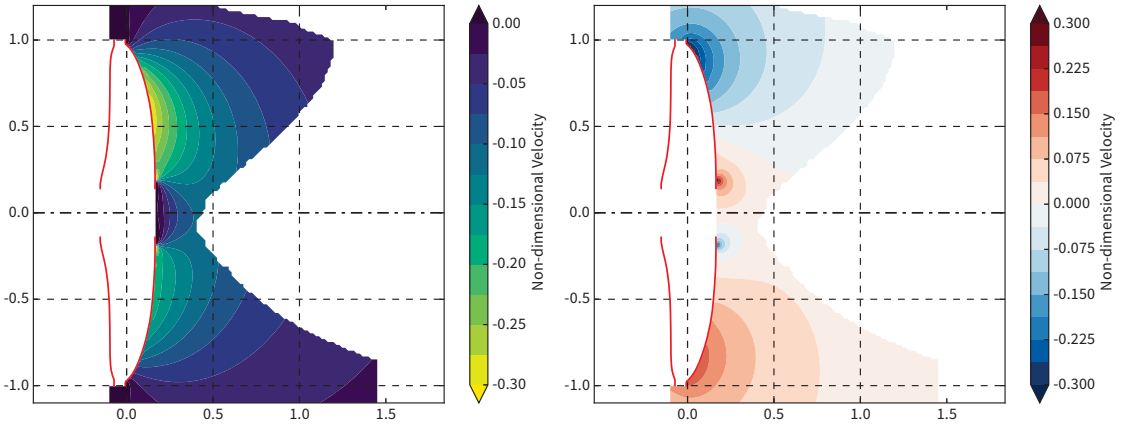

(a) Axial Component **(b)** Vertical Component

Figure 4.21: Induced Velocities in the Center Plane – Conventional

Quantity		Streckwall Kappel	Conv.
Effective Wake Fraction	w	0.265	0.250
Thrust Deduction	t	0.145	0.146
Relative Rotative Efficiency	η_R	1.021	1.023

Table 4.3: Hull-Propeller Interaction Coefficients, Full Scale

4.1.2 Full Scale Simulation Results

Generally, the full scale simulations and results suffer from the same issues as those at model scale, as the agreement of induced velocities (or the lack thereof) is largely scale-agnostic. It therefore appears unlikely, that these full scale simulations uncover substantial differences between conventional and Kappel propellers in terms of effective wake.

Figure 4.22 again shows the difference between the effective wake field from the Kappel propeller and the conventional propeller after applying the coupling corrections based on the known open-water discrepancies, just as Fig. 4.7 for the model scale case. The uniformly distributed small but positive values for the difference of axial velocities indicate that the effective velocities are actually *higher* for the Kappel case, i.e. the wake fraction is lower. This can be attributed to the slightly different locations of the coupling planes, which are following the corresponding propeller's leading edge. Due to the higher pitch (and absence of rake) of the conventional propeller, the plane is located further forward – closer to the hull – for the conventional case, compared to the simulations with the Kappel propeller.

The hull-propeller interaction coefficients as extracted directly from the results are still listed in Tab. 4.3, and the same visualizations of wake fields and induced velocity fields as in model scale are provided.

The full scale velocity distributions displayed on the following pages are still valuable, as they are commonly not known at all in full scale, and as they also serve as input for the cavitation analyses described in the following Section 4.2.

Scaling of Effective Wake Distributions

Focusing on scaling issues instead, several interesting changes in effective wake distribution can be seen comparing the velocity fields from model and full scale. The axial velocity contours in the effective wake field become straighter, as they change from somewhat V-shaped lines to more U-shaped contours. The wake peak becoming narrower is a known and obvious scale effect, but the

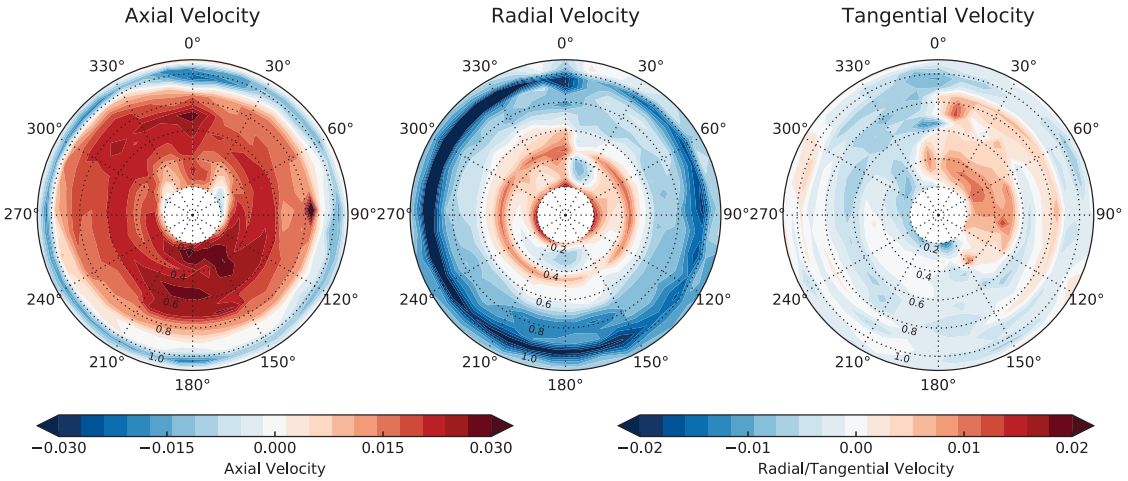

Figure 4.22: Difference of Corrected Self-Propulsion Effective Wake Fields from Conventional and Kappel Propeller

change from the nominal to the effective distribution causes a similar result and thereby further emphasizes this trend, when moving from the nominal distribution at model scale to the full scale effective wake.

A similar and related trend is observed for the in-plane velocity components. With the contraction of the general wake peak, the bilge vortex usually also contracts and becomes weaker, leading to different distributions of radial and tangential velocities. In the particular case analyzed, the change from nominal wake to effective wake again follows a pattern similar to the scale effect. The magnitude of the radial and tangential components increases and a generally less vortical and more upward-directed flow is observed.

Effective flow fields rather different from those at model scale can be seen from the centerplane slices on p. 80 and 81. The scale-related change in radial components is quite evident here as well. It may be interesting to note that the effective radial (vertical in the figure) velocity distribution changes more strongly in longitudinal direction in full scale. Moving the propeller slightly forward or aft might then result in a notably different radial effective wake. And again, no large-scale differences between the fields for the conventional and the Kappel propeller are evident from these figures.

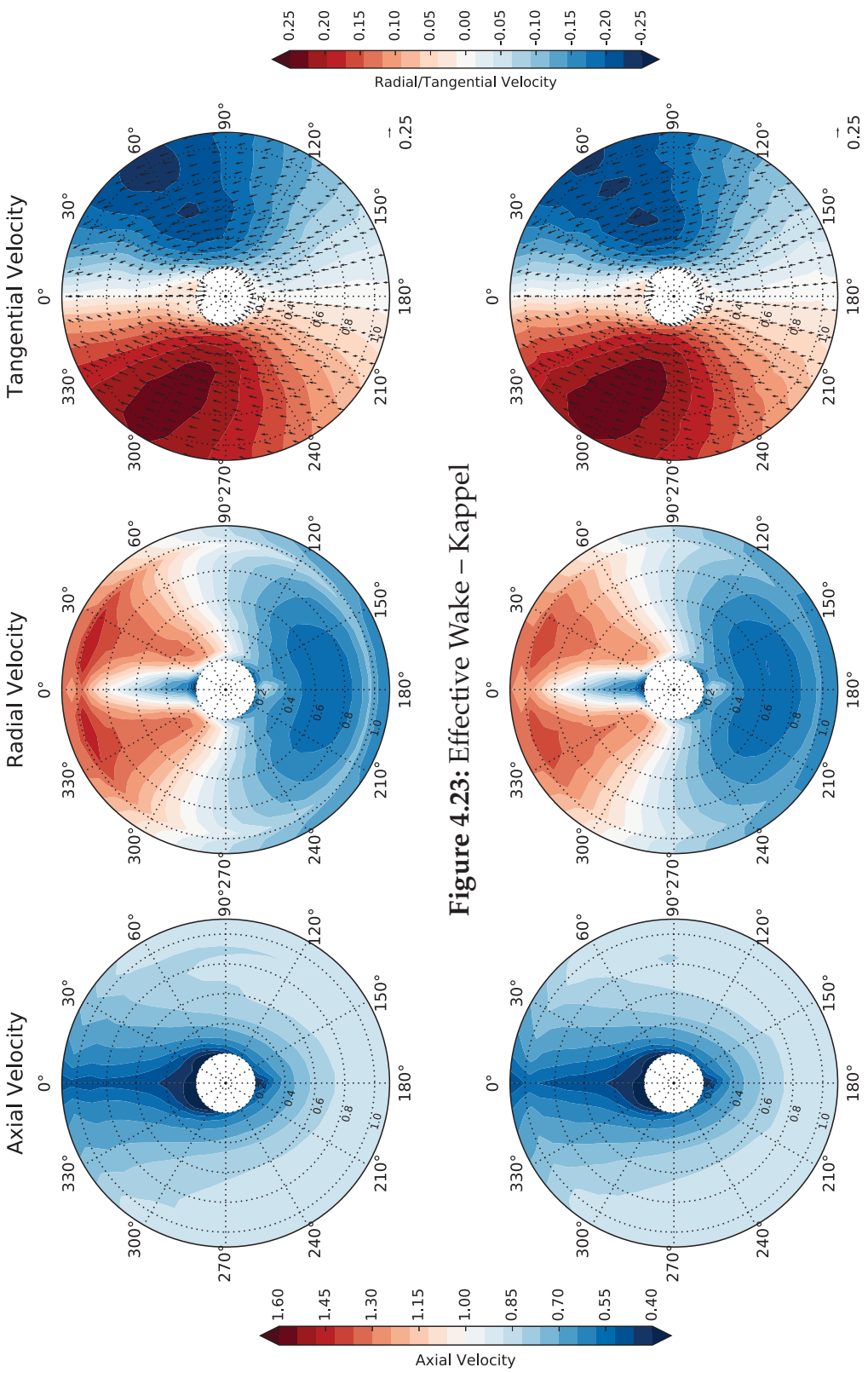

Figure 4.23: Effective Wake – Kappel

Figure 4.24: Effective Wake – Conventional

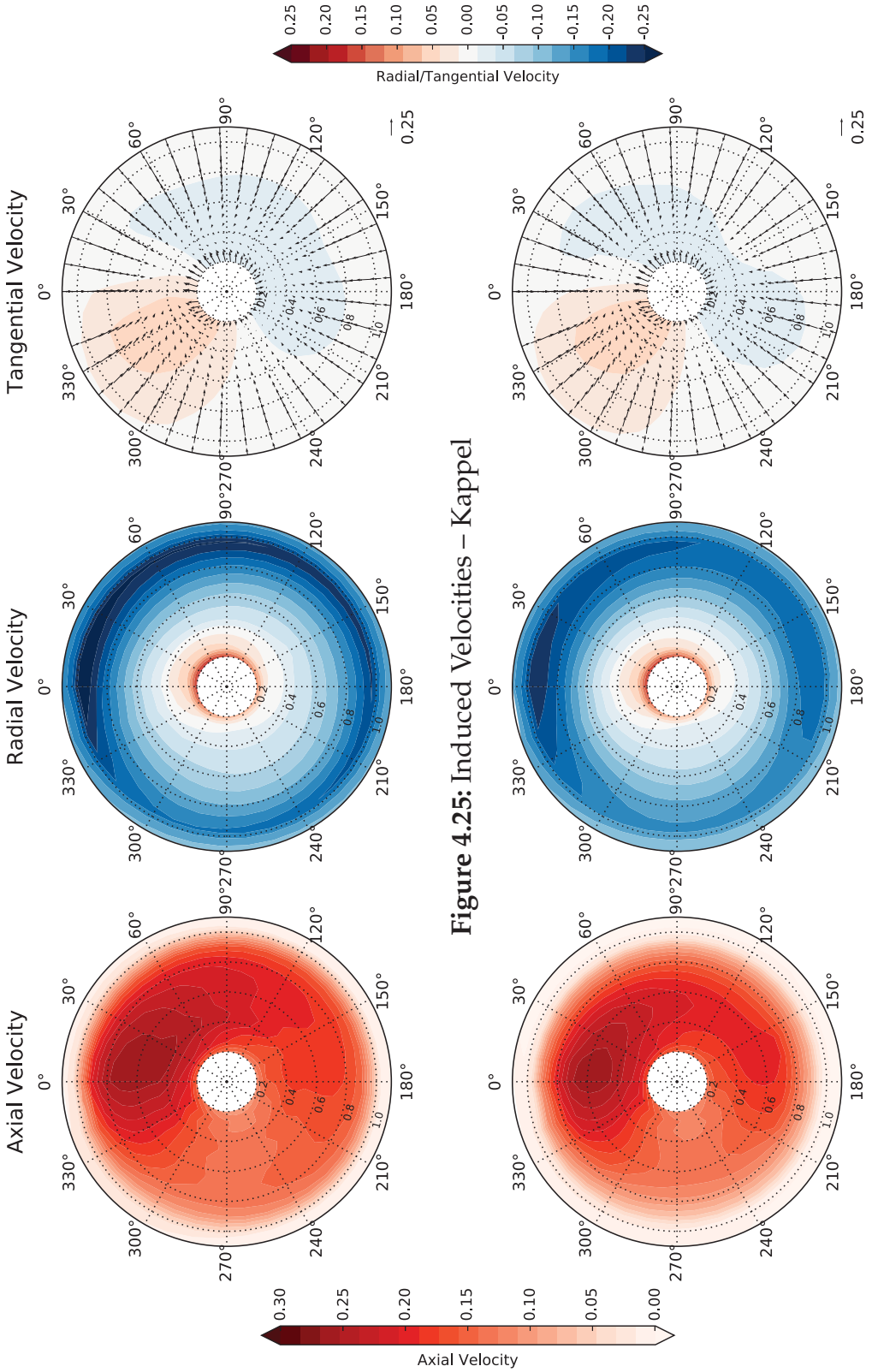

Figure 4.25: Induced Velocities – Kappel

Figure 4.26: Induced Velocities – Conventional

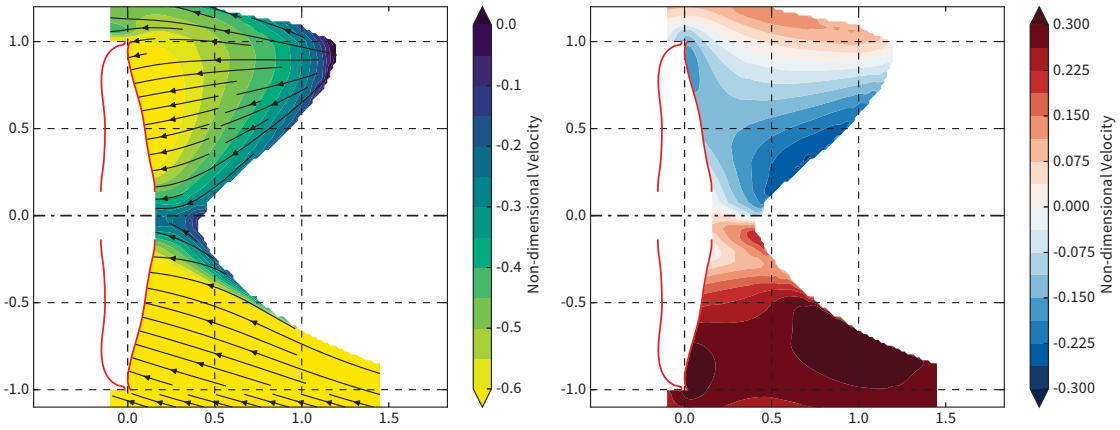

(a) Axial Component **(b)** Vertical Component

Figure 4.27: Total Velocities in the Center Plane – Kappel

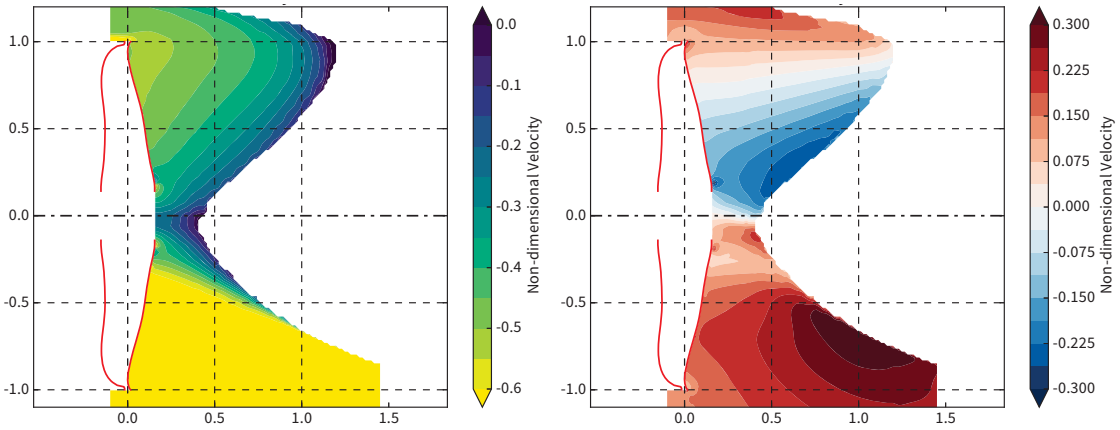

(a) Axial Component **(b)** Vertical Component

Figure 4.28: Effective Velocities in the Center Plane – Kappel

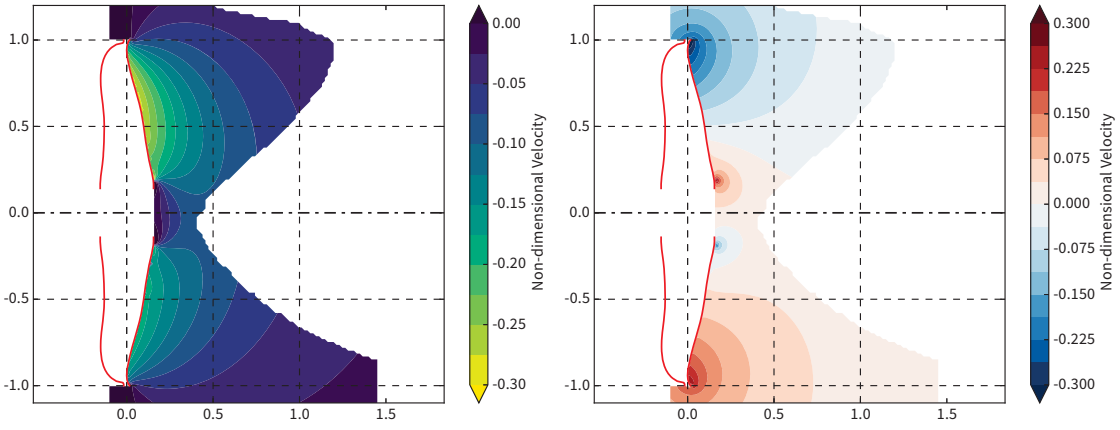

(a) Axial Component **(b)** Vertical Component

Figure 4.29: Induced Velocities in the Center Plane – Kappel

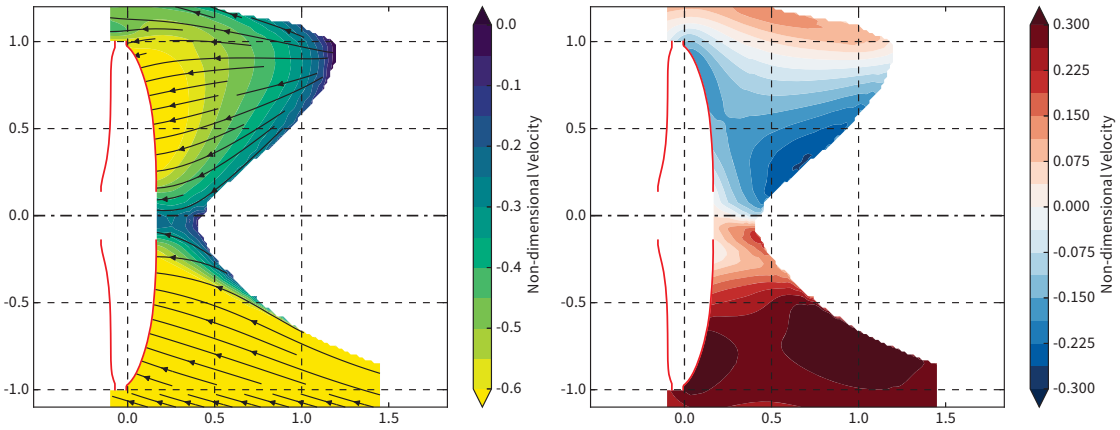

(a) Axial Component **(b)** Vertical Component

Figure 4.30: Total Velocities in the Center Plane – Conventional

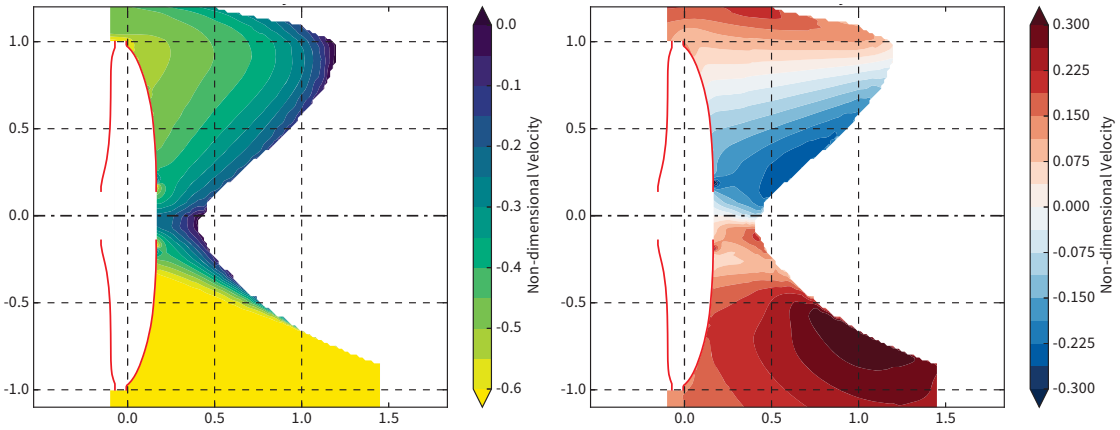

(a) Axial Component **(b)** Vertical Component

Figure 4.31: Effective Velocities in the Center Plane – Conventional

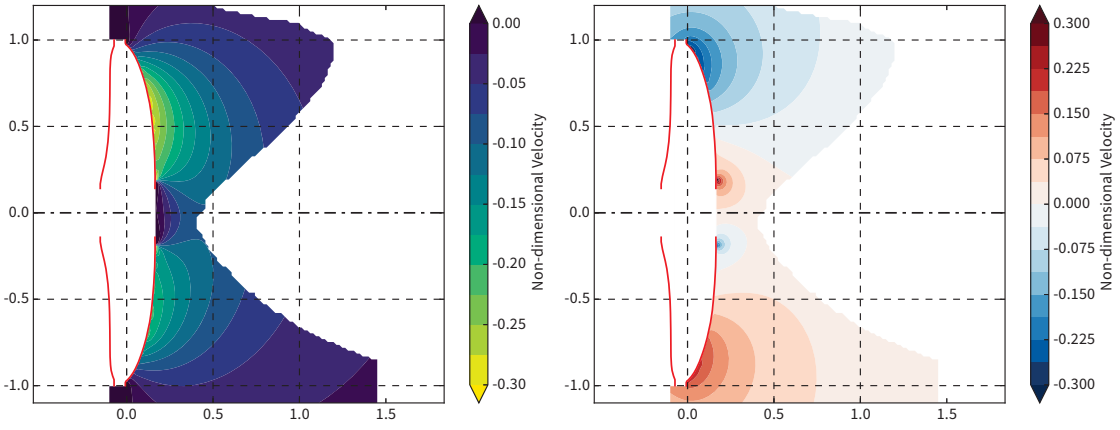

(a) Axial Component **(b)** Vertical Component

Figure 4.32: Induced Velocities in the Center Plane – Conventional

4.2 Cavitation Prediction in Wake Fields

The self-propulsion simulations described in the previous chapter were carried out for the non-cavitating condition. Using a panel code for propeller analysis allows for applying arbitrary wake fields as the inflow field without further approximations. As extracting the effective wake distributions in the self-propulsion simulations is an inherent part of RANS-BEM coupling, one can continue and extend the analysis based on those fields later on. This section provides results of cavitation simulations using ESPPRO with the cavitation model described in Sections 2.2–2.3 enabled.

Compared to this potential flow approach, CFD methods for cavitation prediction (see Section 1.3.3) allow for much higher levels of detail and sophistication for modeling the physical phenomenon of cavitation as such, but including a specific inflow field is non-trivial. In CFD, an effective wake field can only be taken into account by including the entire ship in the simulation at the same time. Applying an arbitrary non-uniform field – such as a measured nominal field – in a reliable way, while retaining its detailed flow features and accounting for the propeller's interaction with this field, is virtually impossible. Approximations are error-prone and always subject to significant uncertainty.

Gaggero et al. (2014) studied the influence of the wake scaling procedure on cavitation. In that study, BEM-based cavitation simulations were run in full scale nominal wake fields obtained by two different methods. First, measured model scale nominal wake fields were scaled to full scale using the method by Sasajima et al. (1966). Then, Gaggero et al. computed the full scale nominal wake field by RANS-based CFD. Even without including the additional effect of hull-propeller interaction, and only comparing differently obtained full scale fields, visible differences in cavitation patterns were noted.

The importance of using the correct effective wake distribution at full scale was also pointed out by the very complete and extraordinary study including full scale tests by Blake, Meyne, Kerwin, Weitendorf, and Friesch (1990). The study that led to that particular paper was initiated after the occurrence of propeller-related and propeller-caused problems in full scale. Blake et al. note that the at that time lacking ability to compute full scale effective wake fractions and distributions was the major missing part of the hydrodynamic design and analysis of ship propellers that ultimately led to (among other problems) the unacceptable full scale cavitation behavior, causing excessive vibrations.

For Kappel propellers specifically, Andersen et al. (2000) name the effective wake field and its differences compared to conventional propellers (as discussed in the previous section) as an important input to the design and analysis of such propellers. Andersen et al. (ibid.) and Andersen et al. (2005b)

partially attribute the different cavitation behaviour of Kappel propellers to the presumptively different shift from nominal to effective wake.

Applying the tools described in the earlier chapters of this thesis, the absolute accuracy of the cavitation prediction is bound by the limitations of potential flow and the particular cavitation model, but the influence of wake scaling *and* hull-propeller interaction (represented by the effective wake distribution) on the cavitation prediction can be investigated individually and combined.

Figure 4.33 (on the next page) shows nominal wake fields at model and full scale (obtained using SHIPFLOW-XCHAP without a propeller model) and effective wake fields, also at model and full scale (using the results from Section 4.1). All wake fields stem from the bulk carrier case described on p. 59f. To ensure comparable operating conditions and resulting thrust values – while highlighting the effect of the *distribution* of velocities – the axial velocities of the wake fields are scaled to always match the same wake fraction of $w = 0.25$. Radial and tangential wake components are not scaled.

The cavitation number $\sigma_n = 3.3$ is slightly lower than that at the full scale design point. It was chosen to ensure that both propellers cavitate in the given wakefields, making a comparison possible. The timestep size corresponds to a blade angle increment of 2°.

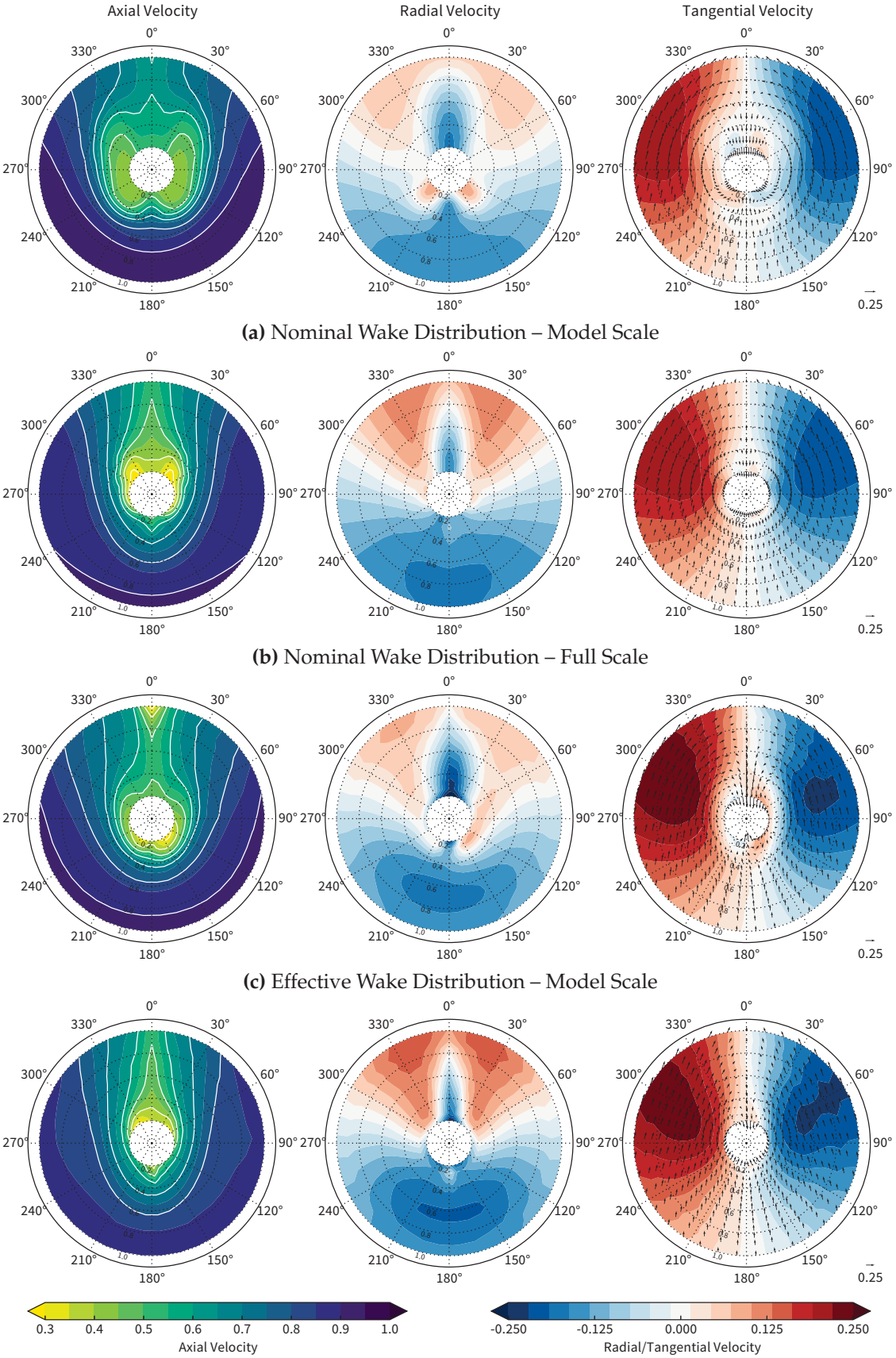

(a) Nominal Wake Distribution – Model Scale

(b) Nominal Wake Distribution – Full Scale

(c) Effective Wake Distribution – Model Scale

(d) Effective Wake Distribution – Full Scale

 Figure 4.33: Wake Fields for Cavitation Analysis, all scaled to $w = 0.25$

Visualization of Results

Running two propellers in four different wake fields at 180 timesteps per revolution generates plenty of data. To visualize the results in a compact way that allows for easy comparison, the cavitation extent over a full propeller revolution is displayed in polar diagrams. As the cavity itself is three-dimensional and time (or blade angle) introduces another dimension, the shape is presented in two different plots. Figures 4.34 and 4.36 show the chordwise extent of the cavity (for the conventional and the Kappel propeller, respectively), while the maximum cavity thickness is plotted in Figs. 4.35 and 4.37.

The chordwise extent is nondimensionalized by the chord length at the corresponding radius. Red areas indicate the presence of supercavitation. The chordwise extent is the aggregate length of cavitating blade panels on one strip. A "cavitating" panel means that the dynamic instead of the kinematic boundary condition is applied. Still, sometimes panels close to the leading edge are triggered and marked as cavitating, but the cavity stays very thin and does not grow further from there. In those cases, a very small – but non-zero – cavity thickness results. Such areas might then be large enough to show up in the "chordwise extent" figures, but are below the threshold value in the figures displaying the cavity thickness. This explains the apparent discrepancies in terms of cavitation extent between the two types of figures.

Cavity thickness values are nondimensionalized by the maximum blade section thickness at the corresponding radius and the lower threshold in the figures is 5%.

Note that the propeller rotation is counterclockwise in these figures, opposite to the wake field figures, and corresponding to a view looking aft. This is common for cavitation sketches as cavitation primarily occurs on the suction side.

Also note that this form of projection is actually not well-suited for proper visualization of Kappel propeller cavitation, as sections close to the tip are located at largely identical radial distances from the shaft. Therefore, certain local cavity features might be difficult to see as they only appear as thin lines (such as in Fig. 4.37d) due to the small radial distance between sections. To overcome this flaw in the visualization, the radial coordinate should preferably be replaced by a curvilinear spanwise parameter that follows the mid-chord line, which would then result in a kind of expanded view of the blade. This is also how the geometry of a Kappel-type propeller blade is commonly described (originally by Andersen and Andersen 1987). However, focusing on large-scale differences and to keep the visualizations simple and comparable, the following figures plot results in a normal polar coordinate system – using the radius.

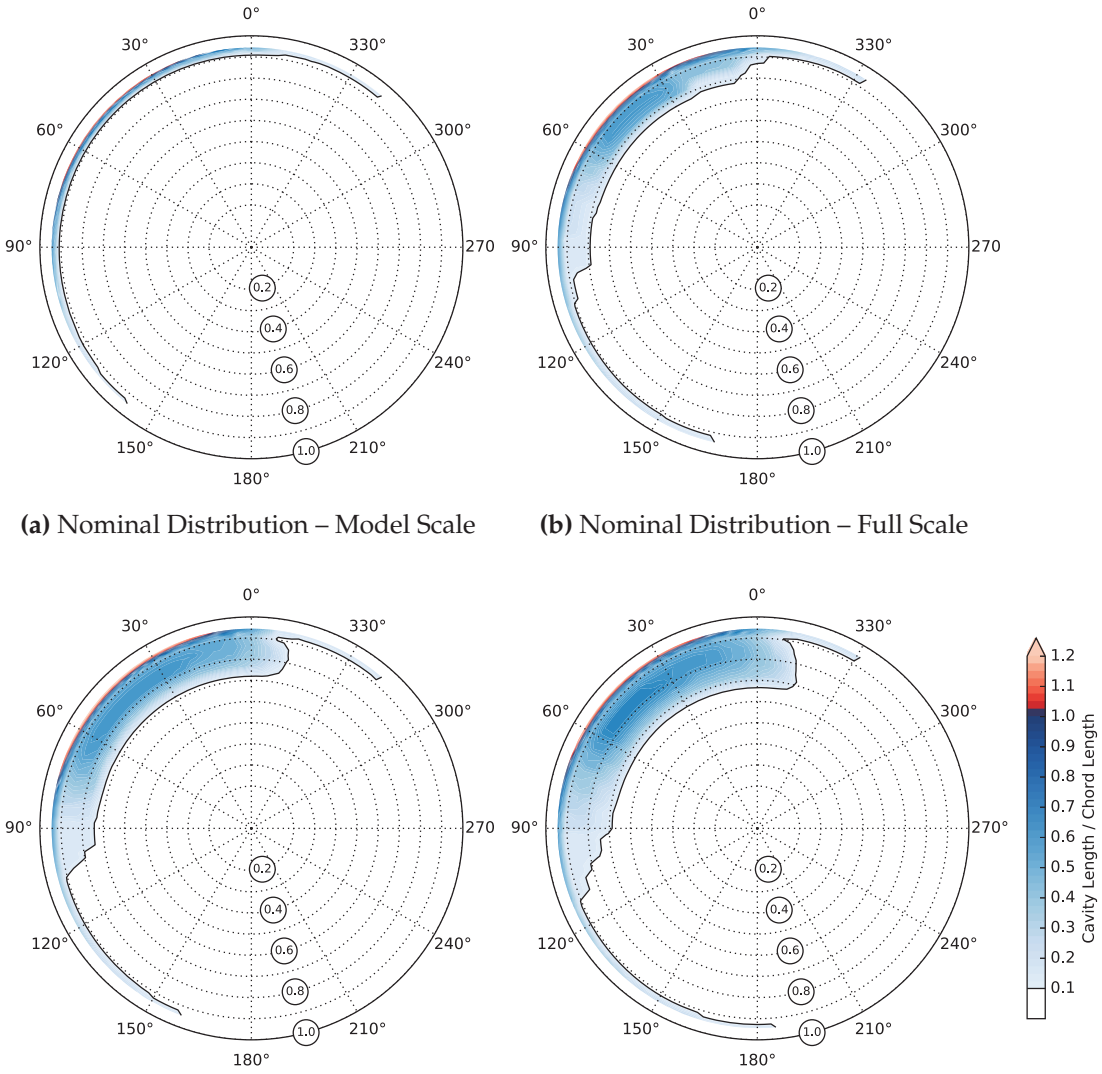

(a) Nominal Distribution – Model Scale

(b) Nominal Distribution – Full Scale

(c) Effective Distribution – Model Scale

(d) Effective Distribution – Full Scale

Figure 4.34: Chordwise Extent of Sheet Cavitation, Conventional Propeller

Results for the Conventional Propeller

Looking at the chordwise extent of sheet cavitation as a function of radius and blade angle in Fig. 4.34 and taking the axial velocity distributions from Fig. 4.33 into account some general observations can be made. The extent of cavitation is smallest for the nominal distribution at model scale and considerably larger for the three other cases. Moving from nominal to effective wake has a slightly larger impact than changing from model to full scale.

The narrower the wake peak at the 12 o'clock position, the larger the extent of the cavity which is triggered as the blade passes through this zone of particularly low axial velocities. As both the shift from nominal to effective and the

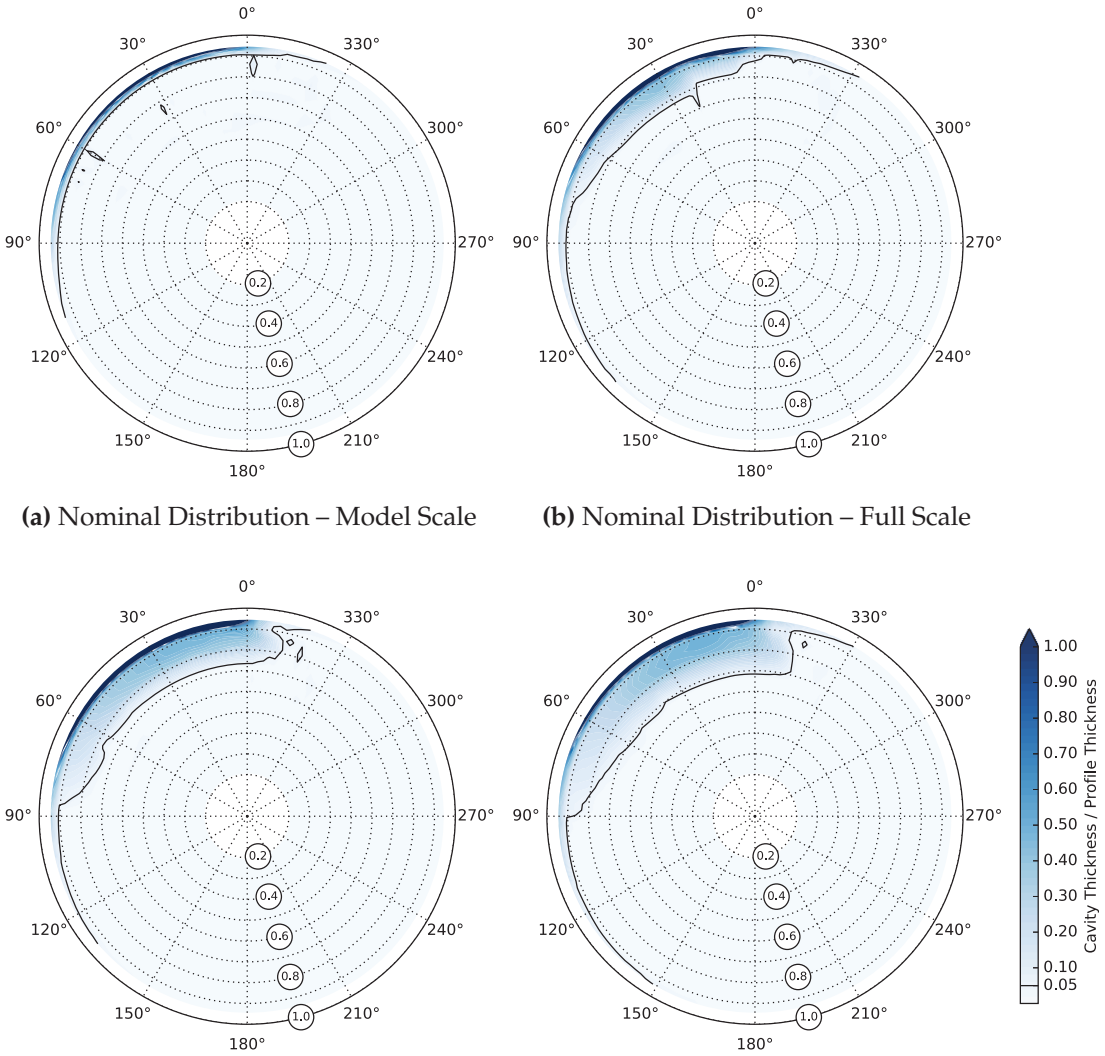

(a) Nominal Distribution – Model Scale

(b) Nominal Distribution – Full Scale

(c) Effective Distribution – Model Scale

(d) Effective Distribution – Full Scale

Figure 4.35: Thickness of Sheet Cavitation, Conventional Propeller

change from model to full scale lead to a narrower wake peak, the additional increase in extent of the combination of these two factors is visible (Fig. 4.34d) but not nearly of the magnitude of the two "individual" increases, compared to the nominal field at model scale.

The same observations apply to the cavity thickness. The thickness always increases in radial direction, and appears to be proportional to the chordwise extent. The outermost strip of panels at the blade tip reaches a long chordwise extent and correspondingly large thickness values in all cases. Whether this is realistic and the sheet cavity actually rolls up into a cavitating tip vortex, or whether the large values are merely due to low mesh quality at the tip is difficult to assess at this point.

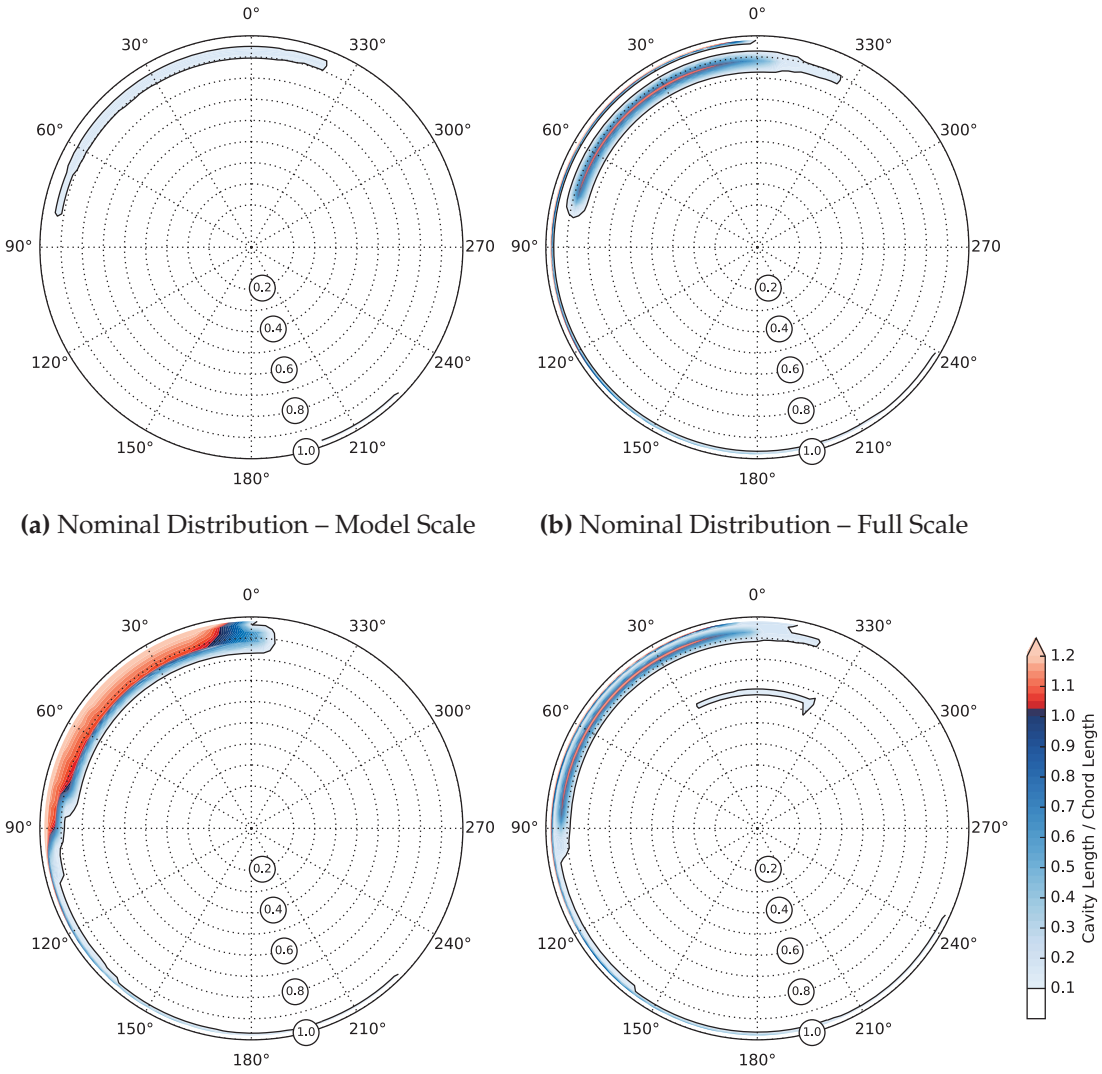

(a) Nominal Distribution – Model Scale

(b) Nominal Distribution – Full Scale

(c) Effective Distribution – Model Scale

(d) Effective Distribution – Full Scale

Figure 4.36: Chordwise Extent of Sheet Cavitation, Kappel Propeller

Results for the Kappel Propeller

As for the case of the conventional propeller, the three-dimensional cavity extent over all blade angles is smallest for the simulation in the model scale nominal wake distribution. In all cases analyzed here, cavitation occurs further out radially than for the conventional propeller. In addition, another trend appears from Fig. 4.36: Once the blade starts to cavitate, the chordwise extent increases from zero to figures close to or above 100% chord length over a short radial distance.

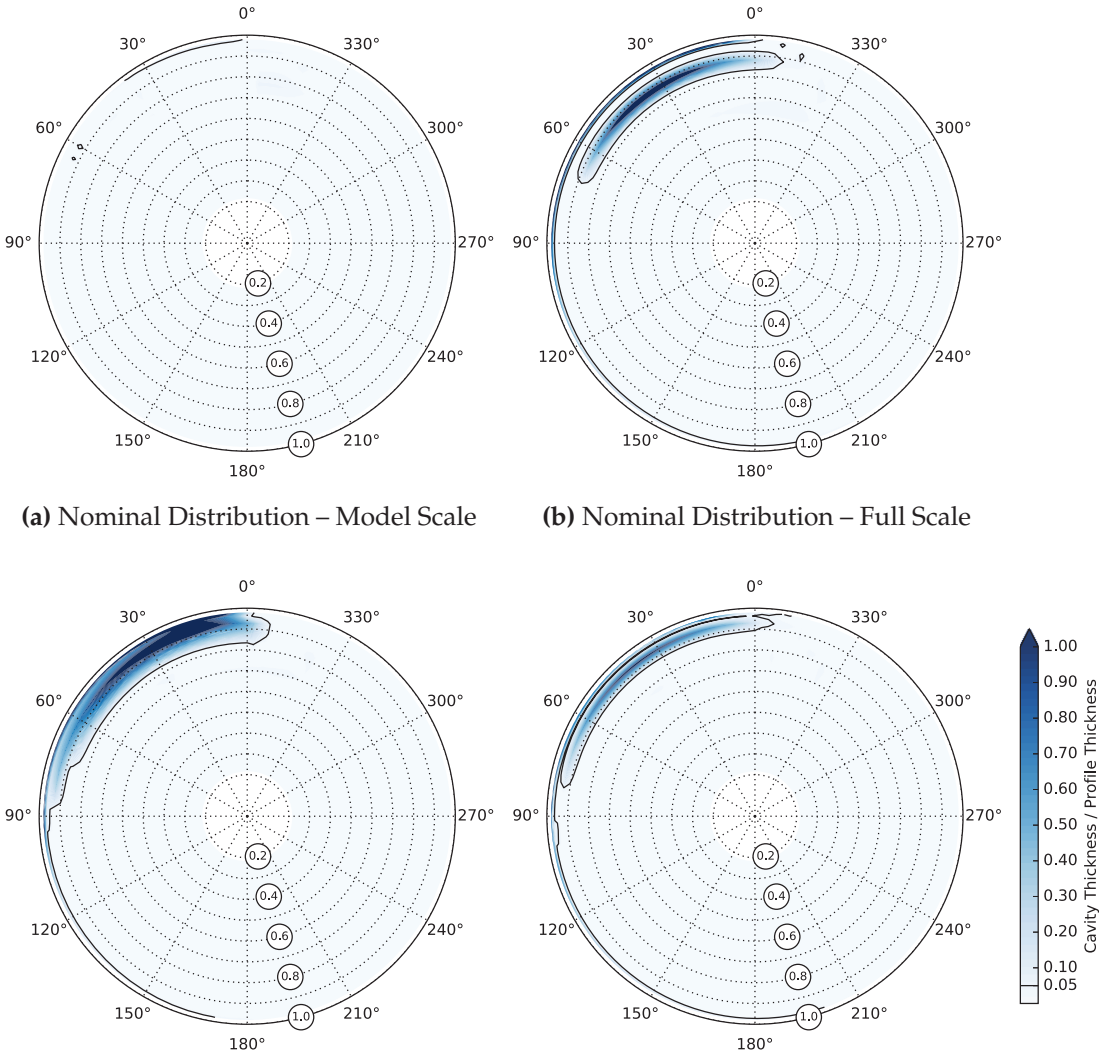

(a) Nominal Distribution – Model Scale

(b) Nominal Distribution – Full Scale

(c) Effective Distribution – Model Scale

(d) Effective Distribution – Full Scale

Figure 4.37: Thickness of Sheet Cavitation, Kappel Propeller

Even though one should remember the flawed visualization, where a very short radial distance translates to a much larger distance along the mid-chord line, both of these observations are generally in line with earlier findings from experiments. Similar cavitation patterns on Kappel propellers in a large cavitation tunnel are described by Andersen et al. (2000). The trend towards thick supercavities in the region of the bent tip seen here and in the experiments was not found in the calculated cavity shapes using a linear and two-dimensional model by Andersen et al. (ibid.).

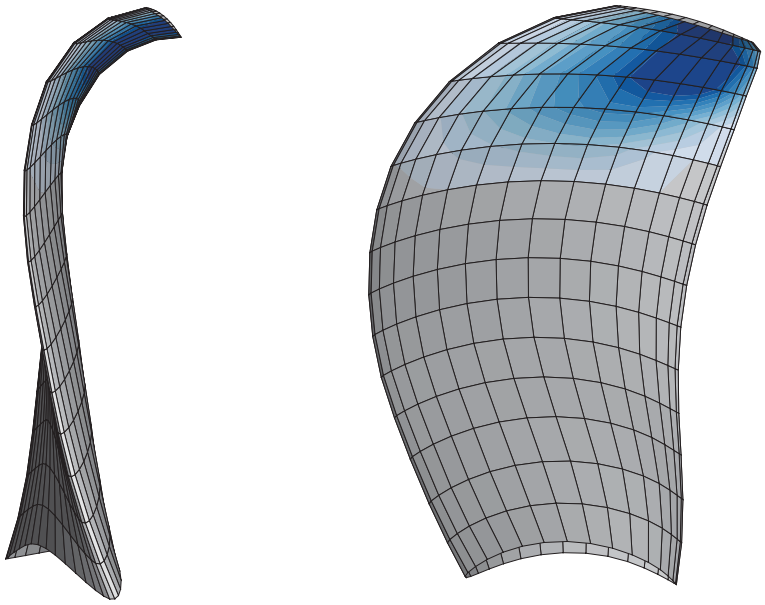

(a) Looking at LE **(b)** Oblique View at Suction side

Figure 4.38: Kappel Propeller in Model Scale Effective Wake Distribution Blade Angle 12°

The very extensive (Fig. 4.36c) and thick cavity in the model scale effective wake distribution seems to be caused by the small area with very low axial velocity close to the tip radius at the 12 o'clock position (see Fig. 4.33c), showing the sensitivity of this particular propeller to small changes in inflow at the tip radius. The resulting difference in predicted cavity extent becomes very obvious in Fig. 4.39.

The role of the radial component of the wake field (which was speculated to be the major and decisive factor by Andersen et al. 2005b) is still not entirely clear. While one could create new, artificial wake fields that combine the axial velocity distribution of the full scale effective wake field with the in-plane components of another case, a better spatial resolution of the blade geometry is also required. In the present mesh, the bend of the Kappel blade – which is where the cavity is forming – is represented by only few panels in spanwise direction and a considerable part of the tip is cut away (see Fig. 4.38).

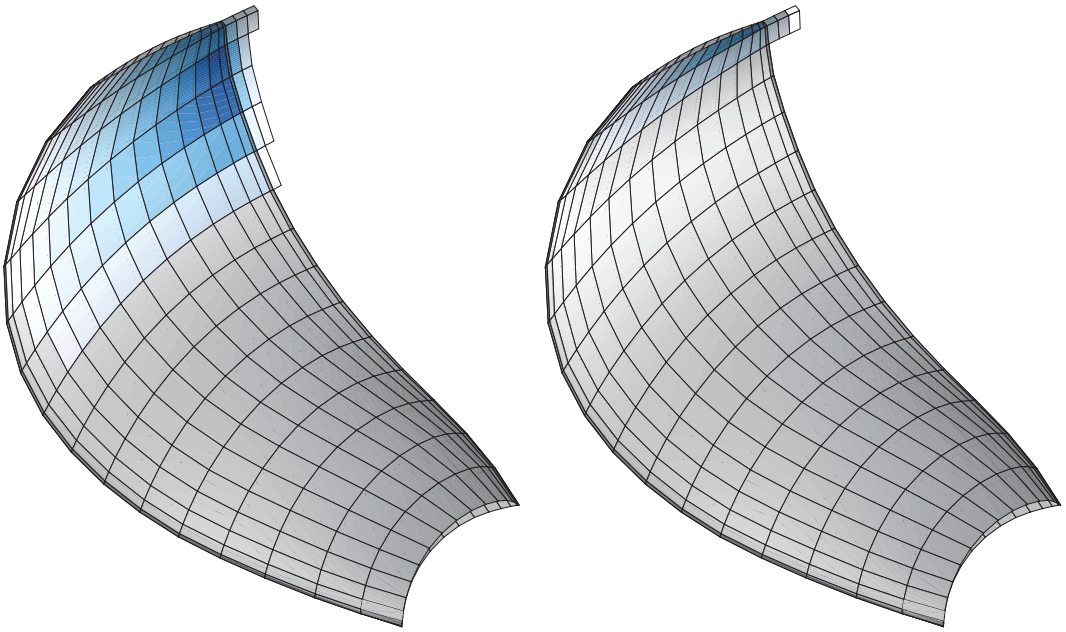

(a) Model Scale Wake Distribution **(b)** Full Scale Wake Distribution

Figure 4.39: Kappel Propeller in Effective Wake Distributions
Blade Angle 45°

5 Conclusion and Outlook

5.1 Conclusion and Final Remarks

The methods developed in the scope of the present work seem to generally work well and robustly and have been applied to carry out numerical self-propulsion tests and cavitation predictions in behind-ship condition at model and full scale.

Effective wake fields have been computed based on a RANS-BEM coupling approach, which then served as input for an unsteady sheet cavitation prediction using the cavitation modeling capabilities of the same BEM implementation. Those methods work robustly for engineering applications and are ready for immediate use as an efficient analysis tool due to their computational efficiency and scalability.

From the application of the RANS-BEM coupling to conventional and Kappel propellers it can be concluded that the difference in radial load distribution between conventional and Kappel propellers is not the main cause for the differences in effective wake fractions observed in model tests.

For Kappel propellers the primitive wake geometry definition appears to be the likely cause for unsatisfactory results using the RANS-BEM coupling. As reasoned in Chapter 3, the coupling method relies on well-matching induced velocities computed directly from the singularities in the BEM and those that result from the body forces on the RANS side. For the conventional blade this agreement is good, whereas too large discrepancies are observed for the Kappel propeller in open water at the advance ratio corresponding to the self-propulsion point. That, in turn, introduces significant uncertainty to the results presented in Section 4.1 and does not allow for a definite and conclusive statement on the reason behind the peculiarities of hull-propeller interaction of Kappel propellers observed in experiments. Depending on the stance taken, one might sensibly argue for two possible interpretations and outcomes:

Either, that there is no significant actual difference in hull-propeller interaction and effective inflow between conventional and Kappel-type propellers. This may be deducted from the results shown in Section 4.1, after applying the coupling corrections to the effective wake fields, assuming all assumptions and simplifications made – including the treatment of the trailing vortices – are fair

and valid. The absence of global differences in effective wake is also implicitly suggested by the main hypothesis by Shin and Andersen (2016), who suggest that scale effects and artifacts related to model test procedures might appear as differences in effective wake fraction, due to differences in Reynolds number between open water and self-propulsion tests.

This hypothesis, however, does not correlate well with full-scale findings, as e.g. published by Andersen et al. (2005a), where the actual full-scale power savings agree well with predictions based on experiments in model scale. In those full-scale predictions, the power savings originate from both an increased open water efficiency and a significantly increased hull efficiency (which is purely due to an increased wake fraction). In the above-mentioned other recent attempt to analyze the effective wake behaviour and related differences between conventional and Kappel propellers, Shin and Andersen (ibid.) used an all-CFD approach, running numerical self-propulsion tests with a discretized propeller using a commercial RANS solver. As discussed in Chapter 3, however, it is impossible to extract the effective wake *field* from such simulations. Therefore, the applicability of that approach is very limited and questionable for this kind of analysis, and the study was not conclusive regarding the effective wake differences, either.

Alternatively, one can continue to assume that the actual effective flow differs as suggested by self-propulsion experiments. Relating this to the results from Section 4.1 implies the assumption that applying the open water-based coupling corrections (described on p. 68) to the behind-ship condition is not entirely correct. In other words: The mismatch in open water does not necessarily translate to discrepancies of similar magnitude and distribution in a non-uniform wake. This is because the coupling corrections must also be largely influenced by the shape of the trailing vortices and hence by the model used in describing the geometry of these vortices. Furthermore, it implies that the aspect of hull-propeller interaction that differentiates Kappel propellers from conventional propellers primarily lies in the alignment of the trailing vortices and their interaction with the hull. In that case a significant difference in hull-propeller interaction between conventional and Kappel propellers may still exist. The simplified model for the geometry of the trailing vortices used in the present work is not able to capture these differences and is therefore not sufficiently accurate for this application. In case the trailing vortices behave very differently from what is currently assumed for Kappel propellers, this might even affect the blade load distribution and the unsteady propeller forces.

Fortunately, the computational procedure including the coupling of the RANS solver and the panel code is of fairly general nature, so that any improvements to either of the programs do not impede the coupling, but will rather lead to immediately realizable improvements of overall results. That

means that the simulations from Chapter 4 can easily be re-run once a more advanced (and correct) way of establishing the blade wake geometry is found and implemented.

For cavitation patterns, the previously conceptually known but now quantified differences between nominal and effective wake distributions have been shown to result in significant differences, regardless of the exact results regarding the effective wake fraction. In particular, it is important to acknowledge the fact that predicting cavitation based on a scaled nominal wake field, measured in a towing tank or computed by CFD in model or full scale, is not a conservative approach. Rather, the full-scale effective wake distribution should be used when evaluating propeller cavitation performance. This seems particularly important for Kappel propellers, which are sensitive to small inflow changes in the tip region and tend to develop long and thick sheet cavities in the bend.

The differences seen in this still comparably simple approach to cavitation modeling also raise additional concerns regarding the validity and applicability of computationally expensive and in principle accurate, purely CFD-based cavitation predictions that do not include the ship hull, but try to model the ship's wake field by other means (see e.g. Shin, Regener, and Andersen 2015). As some of the cavitation-related challenges in the design of Kappel propellers mentioned in earlier work (Andersen et al. 2000; 2005b) remain valid and have partly been reproduced in the present work, hull-propeller interaction should be considered an essential part in future cavitation simulations and the continued development of the Kappel propeller concept.

5.2 Future Work

As suggested in the conclusion, a more advanced model for the alignment of the trailing vortices (blade wake) for unsteady cases in highly non-uniform inflow could lead to significant improvements of the prediction and help answer the still open questions regarding hull-propeller interaction of Kappel propellers.

Such a model should increase the general accuracy of the unsteady force prediction over a large range of thrust loadings and also ensure excellent agreement of induced velocities of BEM and RANS. Both seem likely to be achieved, once the wake is aligned properly with the total velocity field. The development of a model that also works well for Kappel propellers may be supported by velocity field measurements in the propeller wake by experiments or high-fidelity CFD.

Furthermore, it seems natural to develop a new wake alignment model that even integrates with the RANS-BEM coupling approach, as the effective wake

in the propeller race is not identical to the flow field in the propeller plane, which will also influence the aligned shape of the trailing vortices*.

To be able to sensibly and routinely apply such a model, it needs to be considerably faster than the fully iterative alignment schemes that exist today. The always dense, often ill-conditioned matrices found in panel methods are clearly a drawback compared to typical sparse problems encountered in field methods like CFD, as today's fast, efficient, and scalable solution procedures favor the latter. From an engineering point of view, there is little reason to choose a very sophisticated potential flow-based model, if a physically more complete method (that might inherently capture the effect of interest) can run the same kind of analysis in a similar amount of time.

Apart from the continued development of the individual methods, the tools developed and presented in this work seem ready and well-suited for a number of applications. Simulation-based design, as discussed in the introduction chapter, is one of them. While often only fairly small gains in efficiency are reported using that design approach, previous studies show impressive and promising trends in secondary objectives, such as pressure pulses and cavitation volume.

Due to the relatively small computational cost and parallel scalability, the methods are also attractive for application to complex problems, such as self-propulsion simulations in waves – with simultaneous prediction of cavitation and pressure pulses in the full scale effective wake field. Work on that particular problem was recently reported by Taskar et al. (2016), using simpler tools for prediction of cavitation and pressure pulses and also basing those on a nominal wake approximation. Given the substantial influence of hull-propeller interaction on cavitation performance in calm water demonstrated in the present work, it appears attractive to also investigate its influence in other situations and scenarios.

* As already mentioned many years ago by Gilbert Dyne in his written discussion of the paper by Greeley and Kerwin (1982).

Symbols and Nomenclature

Vectors and matrices are written interchangeably using the arrow notation $\vec{v}$ or using bold symbols, as in $\boldsymbol{v}$ or $\boldsymbol{A}$. Scalars are always written in non-bold. Normal vectors are always assumed to be normalized to unit length.

Unless noted otherwise, ITTC standard definitions and nomenclature apply.

Wake fields and cavitation patterns are described and visualized in polar coordinate systems. A blade angle of zero degrees corresponds to the 12 o'clock position. The angle then increases in clockwise direction looking forward. This corresponds to the sense of rotation of all propellers in this thesis.

List of Figures

References

AMDAHL, Gene M. *Validity of the single processor approach to achieving large scale computing capabilities*. In *AFIPS Spring Joint Computer Conference*, pp. 483–485. ACM Press, New York, NY (1967). DOI: 10.1145/1465482.1465560. *Cited on p. 36*

ANDERSEN, Poul. *A Comparative Study of Conventional and Tip-Fin Propeller Performance*. In *21st Symposium on Naval Hydrodynamics*, pp. 930–945. Trondheim (1996). *Cited on p. 9*

ANDERSEN, Poul, ANDERSEN, Svend Vogt, BODGER, Lyn, FRIESCH, Jürgen, and KAPPEL, Jens J. *Cavitation Considerations in the Design of Kappel Propellers*. In *NCT'50 - International Conference on Propeller Cavitation*, pp. 159–174. Newcastle (2000). *Cited on pp. 9, 82, 89, and 95*

ANDERSEN, Poul, BORROD, Anne-Sophie, and BLANCHOT, Herve. *Evaluation of the Service Performance of Ships*. *Marine Technology*, 42(4):177–183 (2005a). *Cited on pp. 9 and 94*

ANDERSEN, Poul, FRIESCH, Jürgen, KAPPEL, Jens J, LUNDEGAARD, Lars, and PATIENCE, Graham. *Development of a Marine Propeller With Nonplanar Lifting Surfaces*. *Marine Technology*, 42(3):144–158 (2005b). *Cited on pp. 9, 62, 64, 82, 90, and 95*

ANDERSEN, Svend Vogt and ANDERSEN, Poul. *Hydrodynamic Design of Propellers with Unconventional Geometry*. *Transactions of the Royal Institution of Naval Architects*, 129:201–221 (1987). *Cited on pp. 9, 59, and 85*

ANDERSON, E, BAI, Z, BISCHOF, C, BLACKFORD, S, DEMMEL, J, DONGARRA, J, DU CROZ, J, GREENBAUM, A, HAMMARLING, S, MCKENNEY, A, and SORENSEN, D. *LAPACK Users' Guide*. Society for Industrial and Applied Mathematics, Philadelphia, PA, 3rd edition (1999). ISBN 0-89871-447-8. *Cited on p. 29*

BALTAZAR, Joao and FALCÃO DE CAMPOS, Jose Alberto Caiado. *An iteratively coupled solution of the cavitating flow on marine propellers using BEM*. *Journal of Hydrodynamics*, 22(5):838–843 (2010). DOI: 10.1016/S1001-6058(10)60039-X. *Cited on p. 32*

BALTAZAR, Joao, FALCÃO DE CAMPOS, Jose Alberto Caiado, and BOSSCHERS, Johan. *A Study on the Modeling of Marine Propeller Tip Flows Using BEM*. In *Congreso de Métodos Numéricos en Ingeniería, SEMNI*. Granada (2005). *Cited on p. 15*

BAUER, Maria and ABDEL-MAKSOUD, Moustafa. *Boundary Element Method for the Computation of Unsteady Sheet Cavitation Effects in Marine Propeller Flows*. In *Proceedings of the 8th International Conference on Engineering Computational Technology*. Dubrovnik (2012). DOI: 10.4203/ccp.100.121. *Cited on p. 24*

BERGER, Stephan. *Kopplung eines Rechenverfahrens für potentialtheoretische Strömungen mit einem Rechenverfahren für viskose Strömungen mit Hilfe eines Propellermodells*. Diploma thesis, TU Hamburg-Harburg, Hamburg (2011). *Cited on p. 50*

BERGER, Stephan, DRUCKENBROD, Markus, PERGANDE, Markus, and ABDEL-MAKSOUD, Moustafa. *A Two-Stage Optimisation Method for Full-Scale Marine Propellers Working Behind a Ship*. *Ship Technology Research*, 61(2):64–79 (2014). DOI: 10.1179/str.2014.61.2.001. *Cited on p. 13*

BERGER, Stephan, GOSDA, Roland, SCHARF, Martin, KLOSE, Rhena, GREITSCH, Lars, and ABDEL-MAKSOUD, Moustafa. *Efficient Numerical Investigation of Propeller Cavitation Phenomena causing Higher-Order Hull Pressure Fluctuations*. In *31st Symposium on Naval Hydrodynamics*. Monterey, CA (2016). *Cited on p. 16*

BERTRAM, Volker. *Practical Ship Hydrodynamics*. Butterworth-Heinemann, Oxford (2012). ISBN 9780080971506. DOI: 10.1016/B978-0-08-097150-6.10001-6. *Cited on pp. 4, 10, and 21*

BETZ, Albert. *Schraubenpropeller mit geringstem Energieverlust*. *Nachrichten von der Gesellschaft der Wissenschaften zu Göttingen, Mathematisch-Physikalische Klasse*, 1919(2):193–217 (1919). *Cited on p. 10*

BLAKE, William K, MEYNE, Klaus, KERWIN, Justin E, WEITENDORF, Ernst-August, and FRIESCH, Jürgen. *Design of APL C-10 Propeller with Full-Scale Measurements and Observations Under Service Conditions*. *SNAME Transactions*, 98:77–111 (1990). *Cited on p. 82*

BODGER, Lyn, HELMA, Stephan, and SASAKI, Noriyuki. *Vibration control by propeller design*. *Ocean Engineering*, 120:175–181 (2016). DOI: 10.1016/j.oceaneng.2015.10.006. *Cited on p. 8*

BRESLIN, John P and ANDERSEN, Poul. *Hydrodynamics of Ship Propellers*. Cambridge University Press (1994). ISBN 9780521574709. DOI: 10.1017/CBO9780511624254. *Cited on p. 53*

BUDICH, Bernd, SCHMIDT, Steffen J, and ADAMS, Nikolaus A. *Numerical Investigation of a Cavitating Model Propeller Including Compressible Shock Wave Dynamics*. In *4th International Symposium on Marine Propulsors (smp'15)*, pp. 555–565. Austin, TX (2015). *Cited on p. 12*

CARLTON, John. *Marine Propellers and Propulsion*. Butterworth-Heinemann, Oxford (2012). ISBN 978-0-08-097123-0. *Cited on p. 43*

CHASE, Nathan, MICHAEL, Thad, and CARRICA, Pablo M. *Overset simulation of a submarine and propeller in towed, self-propelled and maneuvering conditions*. *International Shipbuilding Progress*, 60:171–205 (2013). DOI: 10.3233/ISP-130088. *Cited on p. 57*

CHOI, Jin-Keun and KINNAS, Spyros A. *Prediction of Non-Axisymmetric Effective Wake by a Three-Dimensional Euler Solver*. *Journal of Ship Research*, 45(1):13–33 (2001). *Cited on pp. 47 and 49*

CHOI, Jin-Keun and KINNAS, Spyros A. *Prediction of Unsteady Effective Wake by a Euler Solver/Vortex-Lattice Coupled Method*. *Journal of Ship Research*, 47(2):131–144 (2003). *Cited on p. 50*

CIAPPI, Elena, BRETSCHNEIDER, Herbert, BOSSCHERS, Johan, CHOI, Gil Hwan, FARABEE, Theodore, KAWAKITA, Chiharu, and TANG, Denghai. *Report of the Specialist Committee on Hydrodynamic Noise*. In *Proceedings of the 27th International Towing Tank Conference, Volume II*, pp. 639–679. Copenhagen (2014). *Cited on p. 6*

CONEY, William B. *A Method for the Design of a Class of Optimum Marine Propulsors*. PhD thesis, Massachusetts Institute of Technology (1989). *Cited on p. 11*

DYNE, Gilbert. *A Note on the Design of Wake-Adapted Propellers*. *Journal of Ship Research*, 24(4):227–231 (1980). *Cited on pp. 44 and 45*

ESKILSSON, Claes and BENSOW, Rickard. *Estimation of Cavitation Erosion Intensity Using CFD: Numerical Comparison of Three Different Methods*. In *4th International Symposium on Marine Propulsors (smp'15)*. Austin, TX (2015). *Cited on p. 7*

ESLAMDOOST, Arash, LARSSON, Lars, and BENSOW, Rickard. *Waterjet Propulsion and Thrust Deduction*. *Journal of Ship Research*, 58(4):201–215 (2014). DOI: 10.5957/JOSR.58.4.130057. *Cited on p. 3*

FERZIGER, Joel H and PERIĆ, Milovan. *Computational Methods for Fluid Dynamics*. Springer (2002). ISBN 978-3-540-42074-3. DOI: 10.1007/978-3-642-56026-2. *Cited on p. 39*

FINE, Neal E. *Nonlinear Analysis of Cavitating Propellers in Nonuniform Flow*. PhD thesis, Massachusetts Institute of Technology (1992). *Cited on pp. 16, 18, 24, 25, 26, 27, 28, 33, 34, and 35*

FINE, Neal E and KINNAS, Spyros A. *A Boundary-Element Method for the Analysis of the Flow around 3-D Cavitating Hydrofoils*. *Journal of Ship Research*, 37(3):213–224 (1993). *Cited on p. 34*

FLOWTECH INTERNATIONAL AB. XCHAP *Theoretical Manual*. Göteborg (2007). *Cited on p. 62*

FLOWTECH INTERNATIONAL AB. SHIPFLOW *User's Manual, Version 6.2*. Göteborg (2016). `http://www.flowtech.se`. *Cited on pp. 51 and 63*

FRANC, Jean-Pierre and MICHEL, Jean-Marie. *Fundamentals of Cavitation*. Kluwer Academic Publishers, Dordrecht (2004). DOI: 10.1007/1-4020-2233-6. *Cited on p. 6*

GAGGERO, Stefano, GONZALEZ-ADALID, Juan, and PEREZ SOBRINO, Mariano. *Design of contracted and tip loaded propellers by using boundary element methods and optimization algorithms*. *Applied Ocean Research*, 55:102–129 (2016). DOI: 10.1016/j.apor.2015.12.004. *Cited on p. 13*

GAGGERO, Stefano, VILLA, Diego, VIVIANI, Michele, and RIZZUTO, Enrico. *Ship wake scaling and effect on propeller performances*. In *Developments in Maritime Transportation and Exploitation of Sea Resources*, volume 1, pp. 13–21 (2014). ISBN 9781138001619. *Cited on p. 82*

GREELEY, David S and KERWIN, Justin E. *Numerical methods for propeller design and analysis in steady flow*. *SNAME Transactions*, 90:415–453 (1982). *Cited on pp. 11, 30, and 96*

GREVE, Martin and ABDEL-MAKSOUD, Moustafa. *Potential theory based simulations of unsteady propeller forces including free surface effects*. In *4th International Symposium on Marine Propulsors (smp'15)*, pp. 83–93. Austin, TX (2015). *Cited on p. 50*

GREVE, Martin, WÖCKNER-KLUWE, Katja, ABDEL-MAKSOUD, Moustafa, and RUNG, Thomas. *Viscous-Inviscid Coupling Methods for Advanced Marine Propeller Applications*. *International Journal of Rotating Machinery* (2012). DOI: 10.1155/2012/743060. *Cited on p. 50*

GUSTAFSON, John L. *Reevaluating Amdahl's law*. *Communications of the ACM*, 31(5):532–533 (1988). DOI: 10.1145/42411.42415. *Cited on p. 37*

HALLY, David. *Propeller Analysis Using RANS/BEM Coupling Accounting for Blade Blockage*. In *4th International Symposium on Marine Propulsors (smp'15)*, pp. 297–304. Austin, TX (2015). *Cited on pp. 48 and 55*

HARRIES, Stefan and KATHER, Bernd-Leopold. *Rechnererzeugte Propellergeometrien*. In *Jahrbuch der Schiffbautechnischen Gesellschaft*, volume 91 (1997). *Cited on p. 13*

HESS, John L. *Panel Methods in Computational Fluid Dynamics*. *Annual Review of Fluid Mechanics*, 22:255–274 (1990). DOI: 10.1146/annurev.fl.22.010190.001351. *Cited on p. 15*

HINO, Takanori, CARRICA, Pablo M, BROGLIA, Riccardo, BULL, Peter, KIM, Sung-Eun, LI, Da-Qing, WAN, Decheng, RHEE, Shin Hyung, SAISTO, Ilkka, and VIOLA, Ignazio Maria. *Final Report of the 27th ITTC's Specialist Committee on CFD in Marine Hydrodynamics*. Technical report, International Towing Tank Conference, Copenhagen (2014). *Cited on p. 42*

HINO, Takanori, HIRATA, N, OHASHI, K, TODA, Y, ZHU, T, MAKINO, K, TAKAI, M, and NISHIGAKI, M. *Hull Form Design and Flow Measurements of a Bulk Carrier with an Energy-Saving Device for CFD Validations*. In *PRADS 2016*. Copenhagen (2016). *Cited on p. 56*

HOEKSTRA, Martin. *An Investigation into the Effect of Propeller Hull Interaction on the Structures of the Wake Field*. In *Symposium on Hydrodynamics of Ship and Offshore Propulsion Systems*. Høvik (1977). *Cited on p. 45*

HOLDEN, Kjell Olav, FAGERJORD, Odd, and FROSTAD, Ragnar. *Early Design-Stage Approach to Reducing Hull Surface Forces Due to Propeller Cavitation*. *SNAME Transactions*, 88:403–442 (1980). *Cited on p. 8*

HOSHINO, Tetsuji. *Hydrodynamic Analysis of Propellers in Steady Flow Using a Surface Panel Method - 2nd Report: Flow Field around Propeller*. *Journal of the Society of Naval Architects of Japan*, 166:79–92 (1989). DOI: 10.2534/jjasnaoe1968.1989.166_79. *Cited on pp. 30 and 64*

HOUGH, G R and ORDWAY, D E. *The Generalized Actuator Disk*. In *2nd Southeastern Conference on Theoretical and Applied Mechanics*. Atlanta, GA (1964). *Cited on p. 52*

HSIN, Ching-yeh. *Development and analysis of panel methods for propellers in unsteady flow*. PhD thesis, Massachusetts Institute of Technology (1990). *Cited on pp. 16, 21, 31, 33, and 38*

HUANG, Thomas T and GROVES, Nancy C. *Effective Wake: Theory and Experiment*. In *Symposium on Naval Hydrodynamics*. Tokyo (1980). *Cited on p. 44*

HUNDEMER, Jochen. *Entwicklung eines Verfahrens zur Berechnung der instationären potenzialtheoretischen Propellerumströmung*. PhD thesis, TU Hamburg-Harburg (2013). *Cited on pp. 16 and 17*

INTERNATIONAL MARITIME ORGANIZATION. *Third IMO Greenhouse Gas Study 2014*. London (2015). *Cited on p. 1*

KATZ, Joseph and PLOTKIN, Allen. *Low-Speed Aerodynamics*. Cambridge University Press, 2nd edition (2001). ISBN 9780521665520. DOI: 10.1017/CBO9780511810329. *Cited on pp. 15, 17, and 21*

KERWIN, Justin E. *Marine Propellers*. *Annual Review of Fluid Mechanics*, 18:367–403 (1986). DOI: 10.1146/annurev.fluid.18.1.367. *Cited on p. 45*

KERWIN, Justin E and HADLER, Jacques B. *Propulsion*. Society of Naval Architects and Marine Engineers, Jersey City, NJ (2010). *Cited on p. 1*

KERWIN, Justin E, KEENAN, D P, BLACK, S D, and DIGGS, J G. *A Coupled Viscous/Potential Flow Design Method for Wake-Adapted, Multi-Stage, Ducted Propulsors Using Generalized Geometry*. *SNAME Transactions*, 102:23–56 (1994). *Cited on p. 47*

KERWIN, Justin E and LEE, Chang-Sup. *Prediction of Steady and Unsteady Marine Propeller Performance by Numerical Lifting-Surface Theory*. *SNAME Transactions*, 86:218–253 (1978). *Cited on pp. 11 and 30*

KINNAS, Spyros A. *Simulation of Cavitating and Free Surface Flows using BEM*. In *Boundary Element Methods In Engineering And Sciences*, Chapter 9, pp. 323–363. Imperial College Press (2010a). DOI: 10.1142/9781848165809_0009. *Cited on p. 26*

KINNAS, Spyros A. *Theory of Cavitation*. In *Propulsion*, Chapter 6, pp. 112–124. Society of Naval Architects and Marine Engineers, Jersey City, NJ (2010b). *Cited on p. 6*

KINNAS, Spyros A and FINE, Neal E. *Non-Linear Analysis of the Flow Around Partially or Super-Cavitating Hydrofoils by a Potential Based Panel Method*. In *IABEM-90 Symposium of the International Association for Boundary Element Methods*. Rome (1990). *Cited on pp. 27 and 28*

KINNAS, Spyros A, LEE, Hanseong, and YOUNG, Yin L. *Modeling of Unsteady Sheet Cavitation on Marine Propeller Blades*. *International Journal of Rotating Machinery*, 9(4):263–277 (2003). DOI: 10.1155/S1023621X03000241. *Cited on p. 12*

KLEINWÄCHTER, Andre, HELLWIG-RIECK, Katrin, HEINKE, Hans-Jürgen, and DAMASCHKE, Nils A. *Full-scale total wake field PIV-measurements in comparison with ANSYS CFD calculations: a contribution to a better propeller design process*. *Journal of Marine Science and Technology*, pp. 1–13 (2016). DOI: 10.1007/s00773-016-0418-6. *Cited on p. 43*

KLINKENBERG, Joy and VELDHUIS, Christian. *CFD for twin gondola aft ship design*. In *PRADS 2016*. Copenhagen (2016). *Cited on pp. 39 and 48*

LAMB, Horace. *Hydrodynamics*. Dover, 6th edition (1932). *Cited on p. 17*

LARSSON, Lars and RAVEN, Hoyte C. *Ship Resistance and Flow*. Society of Naval Architects and Marine Engineers, Jersey City, NJ (2010). ISBN 978-0-939773-76-3. *Cited on p. 41*

LARSSON, Lars, STERN, Frederick, and VISONNEAU, Michel (Editors). *Numerical Ship Hydrodynamics - An assessment of the Gothenburg 2010 Workshop*. Springer (2014). ISBN 978-94-007-7188-8. DOI: 10.1007/978-94-007-7189-5. *Cited on pp. 39 and 48*

LAWSON, C L, HANSON, R J, KINCAID, D R, and KROGH, F T. *Basic Linear Algebra Subprograms for Fortran Usage*. *ACM Trans. Math. Softw.*, 5(3):308–323 (1979). DOI: 10.1145/355841.355847. *Cited on p. 29*

LEE, Hanseong and KINNAS, Spyros A. *Modeling of Unsteady Blade Sheet and Developed Tip Vortex Cavitation*. *4th International Symposium on Cavitation (CAV2001)* (2001). *Cited on p. 16*

LERBS, Hermann W. *Moderately Loaded Propellers with a Finite Number of Blades and an Arbitrary Distribution of Circulation*. *SNAME Transactions*, 60:73–117 (1952). *Cited on p. 10*

VAN MANEN, Jan D, VAN OOSSANEN, Peter, and VORUS, William S. *Principles of Naval Architecture*, volume 2. The Society of Naval Architects and Marine Engineers, Jersey City, NJ (1988). ISBN 0-939773-01-5. *Cited on p. 4*

MARTIN, J Ezequiel, MICHAEL, Thad, and CARRICA, Pablo M. *Submarine Maneuvers Using Direct Overset Simulation of Appendages and Propeller and Coupled CFD/Potential Flow Propeller Solver*. *Journal of Ship Research*, 59(1):31–48 (2015a). DOI: 10.5957/JOSR.59.1.140053. *Cited on pp. 50 and 57*

MARTIN, J Ezequiel, MOFIDI, Alireza, MICHAEL, Thad, and CARRICA, Pablo M. *Validation of a Propeller Model for Maneuvering Applications*. In *4th International Symposium on Marine Propulsors (smp'15)*, pp. 288–295. Austin, TX (2015b). *Cited on p. 51*

MCCOOL, Michael, ROBISON, Arch D, and REINDERS, James. *Structured Parallel Programming*. Elsevier (2012). ISBN 978-0-12-415993-8. *Cited on pp. 35 and 36*

MESSAGE PASSING INTERFACE FORUM. *Document for a standard message-passing interface*. Technical Report CS-93-214, University of Tennessee (1993). *Cited on p. 57*

MOORE, Gordon E. *Cramming more components onto integrated circuits*. *Electronics*, 38(8) (1965). *Cited on p. 35*

MUELLER, A C and KINNAS, Spyros A. *Propeller Sheet Cavitation Predictions Using a Panel Method*. *Journal of Fluids Engineering*, 121(2):282 (1999). DOI: 10.1115/1.2822204. *Cited on p. 35*

NEWMAN, John Nicholas. *Marine Hydrodynamics*. MIT Press (1977). ISBN 9780262140263. *Cited on pp. 17, 18, and 43*

NEWMAN, John Nicholas. *Distributions of sources and normal dipoles over a quadrilateral panel*. *Journal of Engineering Mathematics*, 20(2):113–126 (1986). DOI: 10.1007/BF00042771. *Cited on p. 21*

OLSEN, Anders Smærup. *Optimisation of Propellers Using the Vortex-Lattice Method*. PhD thesis, Technical University of Denmark, Lyngby (2001). *Cited on p. 11*

OOSTERVELD, Marinus Willem Cornelis and VAN OOSSANEN, Peter. *Further Computer-Analyzed Data of the Wageningen B-Screw Series*. *International Shipbuilding Progress*, 22(251) (1975). *Cited on p. 10*

OPENMP ARCHITECTURE REVIEW BOARD. *OpenMP Application Programming Interface, Version 4.5* (2015). `http://openmp.org/wp/`. *Cited on p. 36*

PRAEFKE, Eckhard. *The Marine Propeller Design Spiral*. In *2nd International Symposium on Marine Propulsors (smp'11)*. Hamburg (2011). *Cited on pp. 7 and 10*

PYO, Sangwoo. *Numerical Modeling of Propeller Tip Flows with Wake Sheet Roll-up in Three Dimensions*. PhD thesis, Massachusetts Institute of Technology (1995). *Cited on p. 15*

RIJPKEMA, Douwe, STARKE, Bram, and BOSSCHERS, Johan. *Numerical simulation of propeller-hull interaction and determination of the effective wake field using a hybrid RANS-BEM approach*. In *3rd International Symposium on Marine Propulsors (smp'13)*, pp. 421–429. Launceston (2013). *Cited on p. 49*

ROTTE, Gem Michel. *Analysis of a Hybrid RaNS-BEM Method for Predicting Ship Power*. Master's thesis, TU Delft (2015). *Cited on p. 49*

SAETTONE, Simone, REGENER, Pelle B, and ANDERSEN, Poul. *Pre-Swirl Stator and Propeller Design for Varying Operating Conditions*. In *PRADS 2016*. Copenhagen (2016). *Cited on p. 57*

SÁNCHEZ-CAJA, Antonio, MARTIO, Jussi, SAISTO, Ilkka, and SIIKONEN, Timo. *On the enhancement of coupling potential flow models to RANS solvers for the prediction of propeller effective wakes*. *Journal of Marine Science and Technology*, 20(1):104–117 (2015). DOI: 10.1007/s00773-014-0255-4. *Cited on pp. 49, 50, and 68*

SASAJIMA, Hideo, TANAKA, Ichiro, and SUZUKI, Toshio. *Wake Distribution of Full Ships*. *Journal of Zosen Kiokai*, 1966(120):1–9 (1966). DOI: 10.2534/jjasnaoe1952.1966.120_1. *Cited on p. 82*

SCHETZ, Joseph A. and FAVIN, Stanley. *Numerical Solution for the Near Wake of a Body with Propeller*. *Journal of Hydronautics*, 11(4):136–141 (1977). DOI: 10.2514/3.63086. *Cited on p. 47*

SHIN, Keun Woo and ANDERSEN, Poul. *CFD Study on Effective Wake of Conventional and Tip-modified Propellers*. In *31st Symposium on Naval Hydrodynamics*. Monterey, CA (2016). *Cited on p. 94*

SHIN, Keun Woo, REGENER, Pelle B, and ANDERSEN, Poul. *Methods for Cavitation Prediction on Tip-Modified Propellers in Ship Wake Fields*. In *4th International Symposium on Marine Propulsors (smp'15)*, pp. 549–555. Austin, TX (2015). *Cited on p. 95*

STARKE, Bram and BOSSCHERS, Johan. *Analysis of scale effects in ship powering performance using a hybrid RANS-BEM approach*. In *29th Symposium on Naval Hydrodynamics*, pp. 26–31. Gothenburg (2012). *Cited on pp. 48, 49, 50, and 51*

STARKE, Bram, VAN DER PLOEG, Auke, and RAVEN, Hoyte C. *Viscous free surface flow computations for self-propulsion conditions using PARNASSOS*. In *Gothenburg 2010, A Workshop on Numerical Ship Hydrodynamics*. Gothenburg (2010). *Cited on p. 48*

STERN, Frederick, KIM, H T, PATEL, V C, and CHEN, H C. *A Viscous-Flow Approach to the Computation of Propeller-Hull Interaction*. *Journal of Ship Research*, 32(4):246–262 (1988). *Cited on p. 47*

STRECKWALL, Heinrich. *Hydrodynamic Analysis of Three Propellers Using a Surface Panel Method*. In *22nd ITTC Propulsion Committee Propeller RANS/Panel Method Workshop*. Grenoble (1998). *Cited on pp. 30 and 64*

SZANTYR, Jan A. *A Method for Analysis of Cavitating Marine Propellers in Non-Uniform Flow*. *International Shipbuilding Progress*, 41(427):223–241 (1994). DOI: 10.3233/ISP-1994-4142703. *Cited on p. 16*

TASKAR, Bhushan, STEEN, Sverre, BENSOW, Rickard E, and SCHRÖDER, Björn. *Effect of waves on cavitation and pressure pulses*. *Applied Ocean Research*, 60:61–74 (2016). DOI: 10.1016/j.apor.2016.08.009. *Cited on p. 96*

TIAN, Ye, JEON, Chan-Hoo, and KINNAS, Spyros A. *On the Accurate Calculation of Effective Wake/Application to Ducted Propellers*. *Journal of Ship Research*, 58(2):70–82 (2014). DOI: 10.5957/JOSR.58.2.130048. *Cited on pp. 49 and 50*

TIAN, Ye and KINNAS, Spyros A. *A Wake Model for the Prediction of Propeller Performance at Low Advance Ratios*. *International Journal of Rotating Machinery*, 2012(2):1–11 (2012). DOI: 10.1006/jcph.2001.6862. *Cited on p. 30*

TIAN, Ye and KINNAS, Spyros A. *Prediction of Performance of a Cavitating Propeller in Oblique Inflow*. *Journal of Physics: Conference Series*, 656:012073 (2015). DOI: 10.1088/1742-6596/656/1/012073. *Cited on p. 49*

UNITED NATIONS CONFERENCE ON TRADE AND DEVELOPMENT. *Review of Maritime Transport 2016*. London (2016). ISBN 978-92-1-112904-5. *Cited on p. 1*

VAZ, Guilherme. *Modelling of Sheet Cavitation on Hydrofoils and Propellers using Boundary-Element-Methods*. PhD thesis, Universidade Técnica de Lisboa, Lisbon (2005). *Cited on pp. 16, 32, and 33*

VAZ, Guilherme and BOSSCHERS, Johan. *Modelling Three Dimensional Sheet Cavitation on Marine Propellers Using a Boundary Element Method*. In *6th International Symposium on Cavitation (CAV2006)*. Wageningen (2006). *Cited on p. 24*

VESTING, Florian. *Marine Propeller Optimisation - Strategy and Algorithm Development*. PhD thesis, Chalmers University of Technology (2015). *Cited on p. 14*

WANG, Youjiang, ABDEL-MAKSOUD, Moustafa, and SONG, Baowei. *Convergence of different wake alignment methods in a panel code for steady-state flows*. *Journal of Marine Science and Technology* (2016). DOI: 10.1007/s00773-016-0375-0. *Cited on p. 31*

WATSON, David G M. *Practical Ship Design*. Elsevier Science, Oxford (2002). ISBN 9780080440545. *Cited on p. 5*

WÖCKNER, Katja, GREVE, Martin, SCHARF, Martin, RUNG, Thomas, and ABDEL-MAKSOUD, Moustafa. *Unsteady Viscous/Inviscid Coupling Approaches for Propeller Flow Simulations*. In *2nd International Symposium on Marine Propulsors (smp'11)*. Hamburg (2011). *Cited on p. 50*

YOUNG, Yin L and KINNAS, Spyros A. *A BEM for the Prediction of Unsteady Midchord Face and/or Back Propeller Cavitation*. *Journal of Fluids Engineering*, 123(2):311 (2001). DOI: 10.1115/1.1363611. *Cited on p. 35*

ZHANG, Dao-Hua, BROBERG, Leif, LARSSON, Lars, and DYNE, Gilbert. *A Method for Computing Stern Flows with an Operating Propeller*. *RINA Transactions*, 134:245–259 (1991). DOI: 10.3940/rina.sbt.1992.b2. *Cited on p. 47*

DTU Mechanical Engineering
Section of Fluid Mechanics, Coastal and Maritime Engineering
Technical University of Denmark

Nils Koppels Allé, Bld. 403
DK-2800 Kgs. Lyngby
Denmark
Phone (+45) 4525 1360
Fax (+45) 4588 4325
www.mek.dtu.dk
ISBN: 978-87-7475-488-6

DCAMM
Danish Center for Applied Mathematics and Mechanics

Nils Koppels Allé, Bld. 404
DK-2800 Kgs. Lyngby
Denmark
Phone (+45) 4525 4250
Fax (+45) 4593 1475
www.dcamm.dk
ISSN: 0903-1685